Theoretical Modeling of Fundamental Chemical Phenomena at Surface and Interface

(表面や界面で起こる基礎的な化学現象に関する理論的モデル化)

Ben Wang

Graduate School of Chemical Sciences and Engineering

Hokkaido University

August 2021

Contents

Chapter 1

Generation Introduction

1.1 Chemical Phenomena at Surfaces

Chemical bonding formation and catalytic reactions are of great importance in a variety of applications, in which the chemical phenomena and reactions occurring at adsorbate-substrate system are presently the active branches [1]. Almost all the chemical phenomena and reaction at surface are induced by the interfacial electron transfer after the chemisorption of adsorbate on surface. To identify the exact electron transfer mechanism underlying the chemical phenomena and reaction at surfaces, methods that can model the adsorbate-substrate interaction and obtain a clear image of the energy level alignment at the interface should be developed. To reach this target, a significant number of experimental and theoretical investigations have been triggered [2−6]. In comparison to the large-area surface, the interfacial region and active sites that induce the surface reaction exist in very limited area. As a consequence, a small change in the composition of the adsorbate or surface will cause a significantly changed geometric and/or electronic structure and as a consequence a different bonding nature during the chemical process. Therefore, it is necessary to introduce some model systems that can represent the interfacial structure in full details and study the specific elements affecting the interfacial property in a flexible way.

1.2 Self-Assembled Monolayers

Self-assembled monolaters (SAMs) adsorbed on metal substrate electrodes provide a prototypical system to modify the surface system with thin films and organic monolayers and study the molecule-surface interaction [7, 8]. This is due to the convenient formation feature of SAMs and their specific affinity to the metal substrates [9−11]. SAMs can organize spontaneously on the metal surface in a particularly simple and flexible way. The surface can be functionalized and improved with chemical character from the SAMs. The simple and flexible way make the accurate control of adsorption position, intermolecular interactions, and molecule-substrate interface of functional molecules becomes possible, thus providing the new insights into the study of interfacial chemistry. As a consequence, the SAMs/metal surface system has been studied for many years, both from experimental and theoretical perspectives [12−18].

1.2.1 structural features of SAMs

Formation of SAMs experiences the self-assembly process which consists in the spontaneous formation of well-defined geometry by synergic effect of the functional units [8]. The molecular orientation of SAMs should be well-defined on the metal substrate and managed uniformly at the atomic scale. This is critically dependent on the molecule-surface interaction. The driving forces underlying such interaction involve different types of molecule-substrate bonding and inter-, intramolecular interaction like hydrogen bonding, van der Waals forces, electrostatic interactions, and hydrophobic interactions. Characterizing the features of these intermolecular or surface bonding is vitally important for understanding the interfacial electronic structure of SAMs adsorbed on metal substrate which is the basic requirement to develop molecular electronic devices with diverse functionality.

(a) (b)

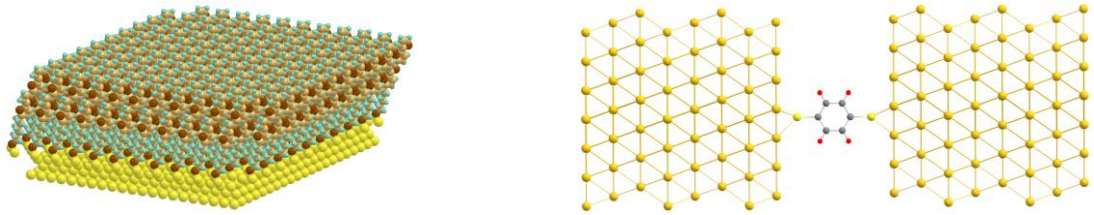

Figure 1.1. Schematic representation of (a) self-assembled monolayers adsorbed on metal substrate, use quaterthiophene (4T)-terminated alkanethiolate SAMs on Au(111) as an example, and (b) self-assembled monolayers sandwiched between two metallic electrodes, use the benzene-1,4-dithiol (BDT) embedded between two Au(111) surfaces used with eight layers of Au on either side with the hollow binding site as an example.

Figure 1.1a shows the structural features of SAMs adsorbed on metal substrate, using quaterthiophene (4T)-terminated alkanethiolate SAMs on Au(111) as an example of SAMs on metal surface. This example model has been used to bound to the Au(111) surface [19, 20]. As the figure shows, the SAMs are distributed in a similar standing-up orientation. Besides, by adding another metal electrode at the terminal of monolayer, the SAMs can act as a linker between two metal electrodes, and therefore can be used for molecular electronics. Herein, benzene-1,4-dithiol (BDT) molecule which is also one popular thiol based SAMs [21−23] switched by two metal electrodes has been used as the model case. The new metal-SAMs-metal structure as illustrated in Figure 1.1(b) shows the necessary properties such as conductance for molecular junctions. The overall device performance is also determined by the electronic structure of SAMs/interface. During the practical applications, even a small change in the SAMs conformation can lead to a significant effect on conductance, thus affecting the performance of the molecular devices.

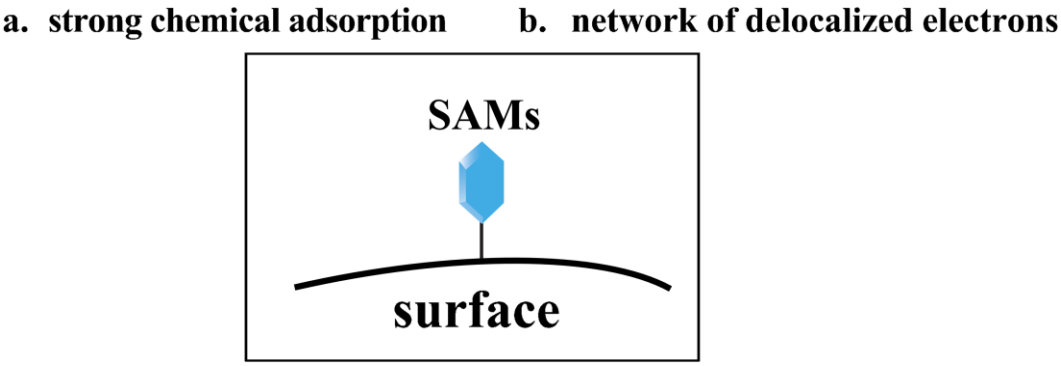

Figure 1.2. Scheme representation of the SAMs adsorbed on surface.

It is necessary to introduce the SAMs−substrate interaction in more detail by extracting only one basic unit from the Figure 1.1. Here, we use the **Figure 1.2** to show the SAMs and the adsorbed surface system. The strong chemical adsorption and also the construction of delocalized electrons after adsorption are two essential factors that should be considered during studying the SAMs/surface interface.

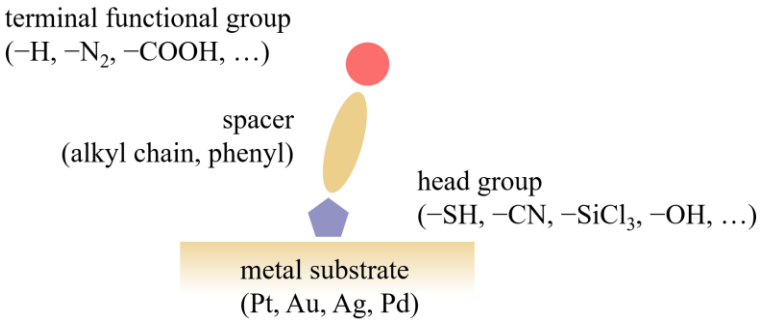

Figure 1.3. Scheme representation of all basic components of a SAM used to bind to the metal substrate. The brackets show some typical examples of each component.

To focus on the individual components of the SAMs, then we use **Figure 1.3** to represent one basic unit of organic monolayer adsorbed on metal substrate. In general, the organic monolayer contains terminal functional group, spacer unit or backbone and head group. The substrate contains several noble metals such like Pt, Au, Ag, Pd or some other semiconductor substrates. Each

component has its own specific effect on the structural conformation of the monolayer on surface, as well as the interfacial electronic structure.

1). The head group, or docking group serves as the connection between the monolayer and metal surface. SAMs generally involve the active head groups that possess specific affinity to metal determines the primitive properties of SAMs. As a feature component of the SAMs systems, the direct interaction with metal substrates make the most significant effect of head group on the chemical bonding interaction;

2). The spacer unit or backbone connects the headgroup and the tailgroup. It can affect the intermolecular interaction and also the molecular orientation by van der Waals forces or hydrogen bonds with the adjacent spacer units. Furthermore, the spacer unit can provide a well-defined thickness that determines the electronic conductivity during the formation of molecular junction;

3). The final one is the terminal functional group, or tailgroup constitutes the outer space of the organic monolayer. The tailgroup can be order in molecular orientation and conformation which involves carboxyl, hydroxyl, porphyrin, or ferrocene, etc. Different groups can bring property of hydrophilicity or hydrophobicity to the system. Moreover, other types of molecules can be attached to this group to increase the structural complexity of the system. The electronic structure of the interface between SAMs and surface can also be affected by the electron-donating or -withdrawing ability of the tailgroup through the spacer unit. Choices of the terminal group substitution allow for a modification on properties of the electrode/organic contact that contribute to the functionality of organic devices.

These three parts works in conjunction to construct the SAMs together. A large category of organic compounds can be used as SAMs, in this chapter, we limit our description to the thiols based SAMs and aryl isocyanide SAMs.

1.2.2 thiols based self-assembled monolayers

Organosulfur compound that contains a thiol (SH) group fabricated SAMs are perhaps the most widely studied type of SAMs and the alkanethiol SAMs on metal surface, particularly on Au(111) are the typical model systems for developing molecular electronics [8, 24−33]. This is mainly due to the high affinity of thiol group to the metal surfaces, and also the inert nature of Au towards oxidation. To grow thiol-derived SAMs on Au surface, researchers usually immerse the clean Au substrate in the organosulfur compound solution (such as alkanethiol in ethanol solution). The deposition step will complete after the enough immersion time (serval hours or a day) in the solution [8]. From a molecular viewpoint, the hydrogen-sulfur (S−H) bond breaks firstly, the thiolate unit adsorbs onto the metal surface via a S−Au bond during the formation of SAMs. After the formation, the covalent S−Au bond is constructed with an adsorption energy of ~2.1 eV [34]. The S−Au bond is strong enough to make displacement of ordered SAMs of thiols on metal substrate becomes feasible [8]. The final SAMs are formed not only through the S−Au chemical bond, but also the nonbonding interactions between the spacer unit, like alkyl chains. The joint effect results in the well-packed and molecular ordered layer on the metal surface.

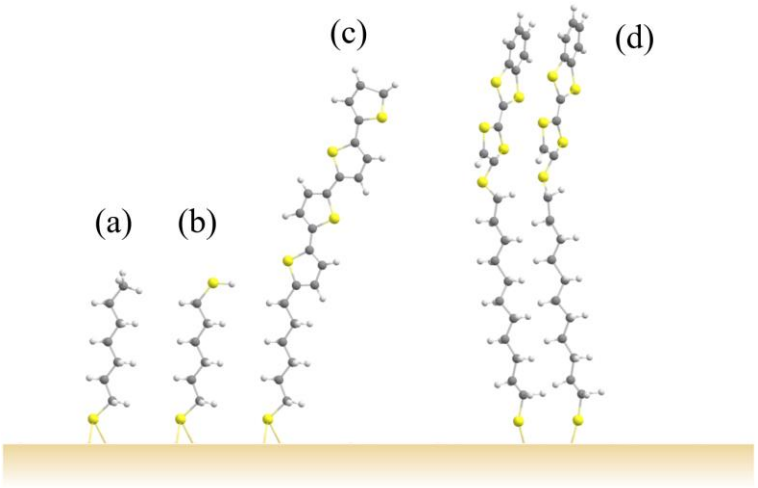

Figure 1.4. A few examples of thiol based compounds adsorbed on metal surface used to form SAMs. (a). normal alkanethiols (C_nSH or C_n (n = number of carbon atoms in alkyl chain)); (b). normal alkanethiols with another −SH as the endgroup; (c). normal alkanethiols with a quaterthiophene group terminated; (d). the dialkyl-disulfide SAMs containing two $S(CH_2)_{11}S$−benzotetrathiafulvalene molecules.

Figure 1.4 shows a few examples of the thiols based SAMs with the increase in structural complexity. The Fig 1.4a is the normal alkanethiols that are always indicated as C_nSH or C_n (n = number of carbon atoms in alkyl chain). Length of the alkyl chain determines the distance between terminal group and metal substrates. In the normal alkanethiols, a methyl group plays as the endgroup, and the alkyl chain as the spacer unit. The endgroup of methyl group can be replaced by other substituents, like another −SH in the Fig 1.4b, or others (e.g., $-OCH_3$, $-NO_2$, etc.). The functionalized alkanethiols can be further improved by introducing complex endgroups, like in Fig 1.4c, a quaterthiophene group is terminated at the end of alkyl chain [19, 20]. Moreover, a dialkyl-disulfide SAM structure established through the oxidation of two adjacent

$S(CH_2)_{11}S$−benzotetrathiafulvalene molecules, as shown in Fig 1.4d, has also been used to bind to the metal surface [35].

When at high coverage, the metal surface is covered with the alkanethiol SAM in the stand-up conformation. As a consequence, as mentioned before, the organic thin films of thiol SAMs can change the physico-chemical properties of the metal substrate through its functionalization. This explains why this type of organic material is so popular, not only for studying the self-assembly process, but also in other diverse fields of applications, such as sensing [36], molecular electronics [37], molecular switching [38], and surface patterning [39]. Further information of thiol fabricated SAMs on metal surface can be found in some other references [40−43].

1.2.3 aryl isocyanide molecule based self-assembled monolayers

Capabilities of the thiol SAMs can be extended to other SAMs with diverse chemical functionality in a similar way. Among them, the aryl isocyanide molecule based SAMs is an essential candidate in contrast to the thiol SAMs. Despite many advantages of thiol SAMs, their application to functional molecular electronic devices has been greatly hindered by their low conductivity [44, 45]. For aryl isocyanide group based SAMs, there is an effective network of delocalized electrons between the π-orbitals of the aromatic ring and the d-band of metal surface, which is linked by the triple bond of the NC group. It has been reported that the −NC/metal junctions have lower conduction barriers that the corresponding thiol-based junctions [46]. Therefore, it is important to establish in detail the bonding mechanism of isocyanide-terminated device-type molecules for molecular electronics applications.

Table 1.1 shows a few examples of aryl isocyanide molecules based SAMs adsorbed on metal surface in recent years. The aryl isocyanide molecules with different functional groups open up the exploration of this kind of SAMs. The metal substrates contains the popular noble metals, and

the essential properties including the adsorption conformation, heterogeneous electron transfer, electron tunneling, thermal stability, and vibrational behaviors have been featured.

Table 1.1. A few examples of isocyanide based compounds adsorbed on metal surface used to form SAMs, the applied substrates in the study and the essential property derived from each study in recent years.

SAM type	Substrate	Key examined property	Ref.
hexane diisocyanide 1,4-phenylene diisocyanide 4,4′-terphenyl diisocyanide 1,4-bis[2-(4-isocyanophenyl)ethynyl]benzene	mirror-finished Au disk electrode	Kinetic behavior and the catalytic activity for oxygen reduction reaction when attached to cobalt(II)−tetraphenylporphyrin (CoTPP)	47
4-methylphenyl-isocyanide	Au(111) surface	Alignment of molecular orientation by optical manipulation	48
hexane diisocyanide 1,4-phenylene diisocyanide 4,4′-terphenyl diisocyanide 1,4-bis[2-(4-isocyanophenyl)ethynyl]benzene	Au disk, Pt monatomic overlayer/Au, Pd monatomic overlayer/Au	Controllable heterogeneous charge transfer and the electrochemical reaction rate	49
Isocyanide terminated perylene diimide (CN_2PDI)	Au, Ag, Pt	Temperature and work function dependent Electron tunneling in SAM junction	50
1-pentyl isocyanide, benzyl isocyanide	Au surface	Thermal stability and adsorption states	51
1,4-phenylene diisocyanide, 4,4′-biphenyl diisocyanide, 4,4″-p-terphenyl diisocyanide	planar gold electrode surfaces	Characterization of electric field and interfacial structure at Au/diisocyanide/aqueous electrolyte interface	52
1,4-phenylene diisocyanide	Ag surface	vibrational features, competitive binding	53

Besides thiols and aryl isocyanide SAMs, there are many other popular SAMs adsorbed on metal substrates. The examples contain amines[54] and isonitriles [55, 56] on Pt and Au, alkynes on Au and Ag [57, 58] carbenes on Au [59−61].

1.3 Experimental Characterization

To identify the SAMs conformation and evaluate the electron transfer across the interface between adsorbate and metal surface, various experimental analytical techniques with well-defined and controllable conditions have been utilized. Among them, two main branches of these analytical techniques are:

a). Microscopy based scanning tunneling microscopy (STM) and atomic force microscopy (AFM). These two techniques are based on microscopy. They can be used to identify the surface morphology, surface coverage, composition of SAMs on the nanometer scale, thus can provide a direct image of the adsorbate/surface structure [62, 63];

b). Spectroscopy based Fourier transform infrared (FTIR) spectroscopy [64], Surface-enhanced Raman scattering (SERS) [65], and near-edge X-ray absorption fine structure (NEXAFS) [66, 67], X-ray photoelectron spectroscopy (XPS) [63, 68, 69] are also applicable for treating the SAMs on substrate system. These spectroscopic techniques are based on the spectroscopic information that generated by the interaction between radiation of a specific energy and irradiated material.

In this section, we introduce two spectroscopic tools – vibrational sum frequency generation (VSFG) spectroscopy and two-photon photoelectron spectroscopy (2PPE), with an emphasis on the former one to provide the experimental characterization of SAMs adsorbed on metal surfaces.

1.3.1 vibrational sum frequency generation spectroscopy

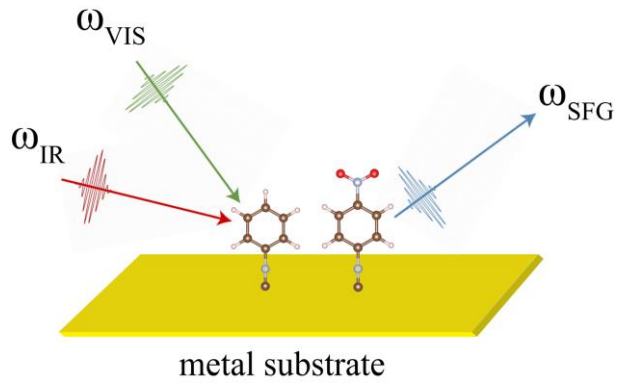

Figure 1.5. Schematic representation of the vibrational sum frequency generation spectroscopy (VSFG) for 4-methylphenyl isocyanide (MPI) and 1,4-phenylene diisocyanide (PDI) molecules adsorbed on metal surface.

Scheme in **Figure 1.5** shows the working mechanism of the VSFG spectroscopy. The theory underlying this spectroscopic technique was proposed by Bloembergen [70], and the development of it has been promoted by Shen group [71]. In general, the VSFG spectroscopy is based on the resonant vibrational transition and is a second-order nonlinear optical laser technique. As for the specific setup, two input laser lights, a frequency fixed visible light (ω_{VIS}) and a frequency tunable IR light (ω_{IR}) irradiate the system. The input two lights spatially and temporally overlap and then convert into a new SFG light. Finally, this new resonant SFG light emits from the system and is detected by the probe. The "sum" of SFG spectroscopy here is reflected in the following equation:

$$\omega_{SFG} = \omega_{VIS} + \omega_{IR}$$

which indicates that the SFG frequency is the summation of two input frequencies.

Unlike other conventional spectroscopic techniques like IR and Raman which are not specific to the adsorbate/surface system, VSFG is intrinsically surface-specific and is especially favorable to study the microscopic structure of interfacial system. The reason underlying this behavior is due

to the quantum mechanical selection rules of VSFG spectroscopy. A nonlinear response can only be observed in the dipole moment of a medium when the laser light irradiates. SFG possess an electric dipole forbidden nature in a centrosymmetric media. The inversion symmetry condition breaks for an interface between two centrosymmetric media [72]. Therefore, VSFG is an effective technique used to selectively probe the interfacial structures like composition and molecular orientation at the interface. Moreover, in conjunction with the time-resolved measurements, the SFG can be used to study the electron transfer dynamics and vibrational relaxation dynamics that occur on the interfacial systems [73−76]. The full theory of VSFG spectroscopy and the experimental setups can be found elsewhere [70, 71, 72].

Utility of VSFG spectroscopy for studying the molecular orientation of the adsorbate/surface system has been proved [77−80] and it has been utilized for the aryl isocyanide molecules adsorbed on noble metal surfaces. Effort of characterization of aryl isocyanide SAMs on metal surface using the VSFG spectroscopy has been given by M. Ito, H. Noguchi, K. Ikeda and K. Uosaki [81]. They have employed two types of SAMs − 1,4-phenylene diisocyanide (PDI) and 4-methylphenyl isocyanide (MPI) adsorbed on Au, Ag, Pt, and Pd as the model cases. The adsorption site, tilt angle of PDI SAMs and MPI SAMs adsorbed on metal substrate have been exploited, showing the substrate dependence.

1.3.2 two-photon photoelectron spectroscopy

Apart from the VSFG spectroscopy, two-photon photoelectron (2PPE) spectroscopy is also an important spectroscopic technique for treating the SAMs/surface system. The general VSFG spectroscopy is a time-averaged spectroscopic technique. Therefore, it cannot be applied to the

dynamical process like ultrafast chemical reactions, chemical exchange on interfaces. These can be performed using the 2PPE spectroscopy as an alternative.

During the practical observation, one electron is excited from the occupied state by the pump pulse, and to the unoccupied state localized at the SAMs adsorbate. The excited electron will then be photoemitted from another probe pulse, and can be captured by one probe pulse[82]. Consequently, the highest occupied molecular orbital (HOMO) and the lowest unoccupied molecular orbital (LUMO) can be detected, and the dynamics of the excited electron can be determined by the time-resolved (TR)-2PPE spectra [83, 84].

Atsushi Nakajima *et. al*. have devoted considerable efforts to this field [85−88]. The essential role of SAMs-ordered metal surfaces on the interfacial electronic structure and electron dynamics have been derived, which provides insights into the surface functionality and benefits the field of surface chemistry in the future research.

In addition to the aforementioned microscopy and spectroscopy based techniques, some other analytical means have also been employed to characterize the SAMs/metal surface system, including surface electrochemistry [89] and thermal desorption [90, 91].

1.4 Theoretical Adsorbate−Surface Model

Although the conventional spectroscopic techniques including surface-specific spectroscopies can be used as complementary techniques to provide essential information of unambiguous chemical identification of SAMs on surface, to reach the accuracy in the quantitative representation at the atomic scale or to complement the experimental observed results, it is necessary to employ the theoretical model. The results based on the theoretical model can be used to confirm or interpret the experimental observations and to provide atomic-scale mechanistic insight into the structural factors that affect the molecular adsorption and ordering on the substrate.

Moreover, different from the physisorption, the chemisorption consists of significant interaction between molecule and surface so that their electronic states hybridize and electron density redistributes. There are multiple electronic states attending the interaction, sometimes an investigation of such bonding is only accessible when theoretical calculations are indeed available.

In this section, the theoretical method for treating the many-atom system like adsorbate-surface case will be introduced. Two typical theoretical models – d-band model and Blyholder model will be mainly presented in this section to give a simple picture of the electronic structure of adsorbate/surface system.

1.4.1 nature of metallic and molecular electronic states

Chemical interaction between molecule and surface can be understood from the energy levels of the interacting electronics states. **Figure 1.6a** shows the energy diagram of a metal surface. Atoms are held together in a metal surface via the metallic bonding. The electron energy levels of metal atoms with delocalized nature constitute the dense and continuous energy bands. The valence bands are filled with electrons up to the Fermi energy level (E_F). The energy difference between

E_F and vacuum level corresponds to the work function (Φ). The work function corresponds to the minimum amount of energy needed to remove an electron from the metal. In metals, work function and ionization energy are the same.

On the other hand, the adsorbate molecule has discrete electronic states due to the localized electrons and charge density populating in the intramolecular covalent bonds. The **Fig. 1.6b** shows the electron localization function of a molecule (using one aryl isocyanide molecule – H−C_6H_4−NC as example). The highly localized electrons are found around the atom, which is different from the metallic case.

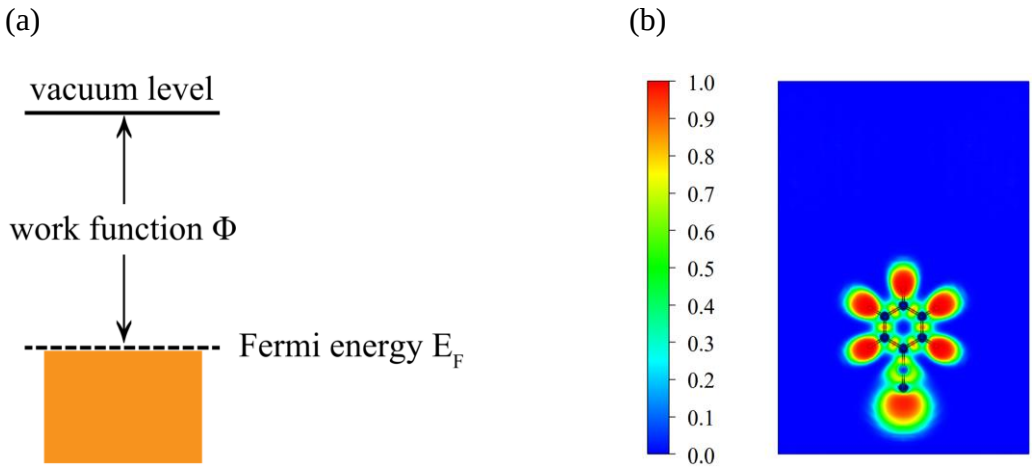

Figure 1.6. (a) Schematic illustration of the metallic electronic states and (b) electron localization function of isolated H−C_6H_4−NC molecule. The red color indices the stronger electron localization, while the blue color means electrons are delocalizing in the atmosphere.

SAMs adsorb on metal surface when they are bound in the vicinity of the surface, their respective states mix with each other so that hybridization occurs, and new electronic states will be generated. As a consequence, the energy levels of adsorbed molecule will be affected, depending on the strength of the chemical bonding. In comparison to the uncoupled systems, the energy levels of new electronic states will broaden and shift with respect to the original unbound

cases. There are two key electronic parameters that play important role on adsorbate-surface interaction, modification of the electrode work function due to the SAMs adsorption and the alignment of the SAMs electron levels (conducting states) with respect to the Fermi level.

1.4.2 d-band model

An important model of electronic structure and adsorption energy is the d-band model presented by Hammer and Nørskov [92, 93] which is developed based on the Newns-Anderson model for adsorption [94−96] and a similar formalism by Grimley [97, 98] and has been proven very useful for understanding the chemical bond formation between molecule approaching diverse noble metal surfaces [99, 100].

According to the d-band model, the interaction between adsorbate and metal surface can be conceptually treated as a consecutive two-step interaction as the **Figure 1.7** shows:

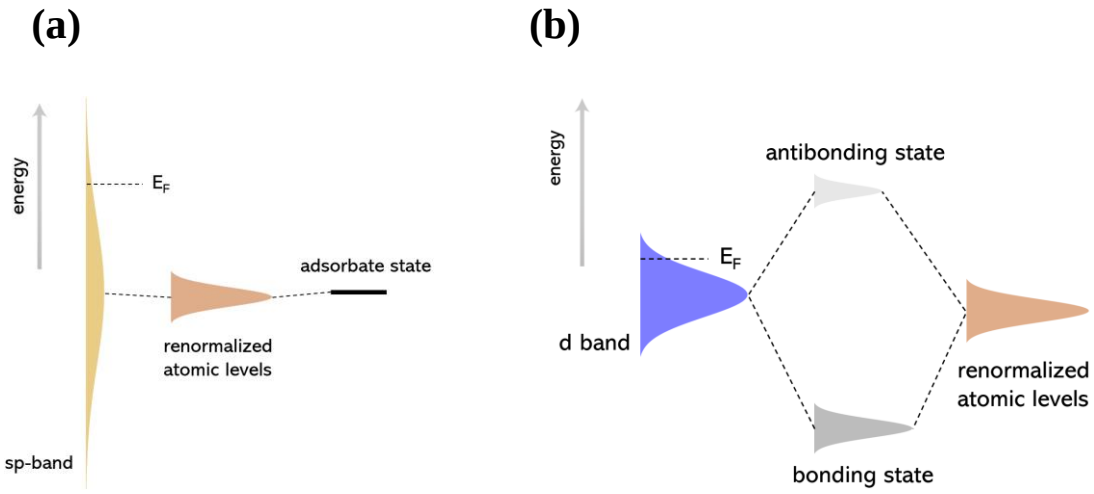

Figure 1.7. Schematic energy diagram of d-band model for molecular adsorbed on metal surface via a chemisorption.

a). The first step is the interaction between metal free-electron-like sp-band with adsorbate level. There are a broad delocalized sp-band and a narrow localized d-band for metal surfaces

according to the density of states (DOS) of metal surface. Here in the Fig. 1.7a, the yellow filled curves show the dense and continuous bands of hybridized sp-bands, while the discrete electronic states of the adsorbate has been represented by the black line. They reason why the metal sp-band firstly interacts with the adsorbate is due the more electrons in sp-bands that spill out into the vacuum level. A broadening of the adsorbate level happens due to the adsorbate resonance, and the new level shifts down (because the substrate Fermi level and the electron chemical potential of the atom become aligned). These broadened and shifted energy levels represented by brown color are named as "renormalized atomic levels" [100];

b). The formed renormalized atomic levels after the step a) will continue to react with the localized d-bands. The d-bands have been represented by filled blue curves in Fig. 1.7b. d-bands are more localized than sp-bands, therefore they have relatively narrow peak. The interaction between renormalized atomic levels and narrow d-bands gives rise to the separation of bonding states (an increase trend in electron density) and antibonding states (a decrease trend in electron density) [100].

Most sp-bands are similar throughout the noble or transition metals, and so differences in bond formation, as well as catalytic adsorption rates are attributed to the interactions with d-band. Occupancy in bonding and corresponding antibonding states determines the bonding strength. It is obvious that the bonding is strongest when bonding states are fully occupied while antibonding states remains empty. The picture of bonding and antibonding states enables us to determine the nature of one chemical bond. If the antibonding states are at least partially empty, the chemical bonding possess ionic or covalent character: ionic character shows the bonding states are mainly produced either from adsorbate or substrate orbitals, the covalent character represents almost same amount from adsorbate and substrate comprise the bonding states. Such a classification is efficient

when regions of a substrate and an adsorbate can be defined and separately treated. However, it is always no easy to assign the electron density to different atoms for strong chemisorption case. An alternative way to assign electron density to individual atoms in a many-atom system was developed by Bader [101−104]

The d-band model gives a qualitative interpretation for molecule adsorbed on different transition metal surfaces and has been applied to understand the catalytic activity of transition metal surfaces. According to this model, main changes in the adsorbate levels due to the interaction between adsorbate and metal substrate can be summarized as:

i). increase in width and a shift in energy;

ii). formation of bonding and antibonding orbitals.

1.4.3 Blyholder model

There are two frontier orbitals – namely highest occupied molecular orbital (HOMO) and the lowest unoccupied molecular orbital (LUMO) in the molecule. Their energy difference is called as an energy gap. In the frontier theory, it can be intuitively understood that the donor and acceptor states of a molecule is directly related to its HOMO and LUMO levels.

This leads to a simpler picture of bonding interaction between adsorbate and transition metal surface – the Blyholder model (also known as the donor-acceptor model) [105]. The Blyholder is another model for describing the interaction between adsorbate and metal surface and is much simpler than the d-band model.

In this model, it is general assumed that the chemical bonding at the interface between molecule and metal surface can be interpreted in terms of the interaction of the frontier molecular orbitals with the d orbitals of metal atom. The model is initially used to explain the interaction

between CO and metal surfaces, the CO 5σ orbital hybridizes with the d orbital of metal substrate, which is the main bonding force during the interaction. On the other hand, the metal d orbital gives electron back into the antibonding 2π* orbital of CO molecule. In addition to the CO adsorption, the Blyholder model has been also applied to NO adsorption. However, sometimes the Blyholder is oversimplified, it only focuses on the frontier orbitals (5σ, 2π* in the case of CO), the contributions from other lower lying molecular orbitals (4σ, 1π, 3σ, as well as the core states of CO) have been considered essentially without change as in the uncoupled case. The details of the bonding are somewhat more complicated than Blyholder model.

1.5 Structure of This Thesis

The goal of this thesis is to give an intuitive picture that can provide insight into the fundamental processes governing the interfacial phenomena and that can guide for the design of optimized functional interfaces. Throughout this dissertation, we will use various theoretical approaches to tackle the electron transfer across the interface and the (photo)catalytic reaction that occurs on surfaces. We will show to what extent the adsorbate and substrate influence the interfacial electronic structure on an atomistic scale.

Chapter 1 has given a basic overview of SAMs adsorbed on metal substrate, two typical molecules used as SAMs with a strong emphasis on aryl isocyanide molecules, experimental characterization, as well as the theoretical model. Then in Chapter 2, starting from the many-body time-dependent Schrödinger equation, we denote the theoretical background which is the foundation of calculations in the subsequent chapters, with an emphasis on the periodic system calculation and the plane wave method. In Chapter 3, we focus on the adsorbate-induced electron transfer and the chemical bonding nature upon adsorption on the Pt(111) surface. By incorporating a periodic NBO algorithm, the electron transfer strength can be evaluated in a quantitative and efficient way. In Chapter 4, we further explore the substrate effect on the interfacial electronic structure. Substrate dependent electron transfer across the interface between SAMs and metal surface have been clarified. In Chapter 5, we turn our attention to the catalytic reactions that occur on the surface. The long distance functionalization induced by O_2 adsorption on single C atom doped h-BN surface is presented. Two typical oxidation reactions have been employed to verify the O_2 activation. In Chapter 6, the exploration of surface reaction will expand to the photocatalytic oxidation. The reaction routes after the photoexcitation of phenol molecule on anatase TiO_2(001)

surface is attempted to explain. In Chapter 7, we give main conclusions of work presented in this thesis and suggest the outlook for further study in the research areas inspired by this thesis.

1.6 References

[1] G. A. Somorjai and Y. Li, Introduction to Surface Chemistry and Catalysis (Wiley, Hoboken, NJ) 2nd Ed (2010).

[2] G. Ertl, Reactions at Solid Surfaces (Wiley, Hoboken, NJ) (2009).

[3] A. W. Adamson and A. P. Gast, Physical Chemistry of Surfaces (Wiley, New York), 6th Ed (1997).

[4] P. C. Hiemenz and R. Rajagopalan, Principles of Colloid and Surface Chemistry (Marcel Dekker, New York), 3rd Ed (1997).

[5] D. P. Woodruff and T. A. Delchar, Modern Techniques of Surface Science (Cambridge Univ Press, New York), 2nd Ed (1994).

[6] A. Nilsson, L. G. M. Pettersson, and J. K. Norskov, Chemical Bonding at Surfaces and Interfaces (Elsevier Science & Technology, Amsterdam) (2008).

[7] G. Whitesides, *Science* **295**, 2418 (2002).

[8] G. Bracco; M, Smerieri; L. Savio, Self-assembly of Organic Molecules at Metal Surfaces. Springer Handbook of Surface Science 2020, 967−1004.

[9] S. M. Barlow and R. Raval, *Surf. Sci. Rep*. **50**, 201 (2003).

[10] J. V. Barth, J. Weckesser, N. Lin, A. Dmitriev, and K. Kern, *Appl. Phys*. A **76**, 645 (2003).

[11] S. De Feyter and F.C. De Schryver, *Chem. Soc. Rev*. **32**, 139 (2003).

[12] K. Wang and B. Xu, *Top. Curr. Chem*. **375**, 17 (2017).

[13] D. Olson, A. Boscoboinik and W. T. Tysoe, *Chem. Commun.* **55**, 13872 (2019).

[14] S. Watson, M. Nie, L. Wang, and K. Stokes, *RSC Adv.* **5**, 89698 (2015).

[15] E. Leary, A. La Rosa, M. T. González, G. Rubio-Bollinger, N. Agraït, and N. Martín, *Chem. Soc. Rev.* **44**, 920 (2015).

[16] T. A. Su, M. Neupane, M. L. Steigerwald, L. Venkataraman, and C. Nuckolls, *Nat. Rev. Mater.* **1**, 16002 (2016).

[17] S. Ahn, S. V. Aradhya, R. S. Klausen, B. Capozzi, X. Roy, M. L. Steigerwald, C. Nuckolls and L. Venkataraman, *Phys. Chem. Chem. Phys.* **14**, 13841 (2012).

[18] J. C. Love, L. A. Estroff, J. K. Kriebel, R. G. Nuzzo and G. M. Whitesides, *Chem. Rev.* **105**, 1103 (2005).

[19] H. S. Kato, Y. Murakami, Y. Kiriyama, R. Saitoh, T. Ueba, T. Yamada, Y. Ie, Y. Aso, and T. Munakata, *J. Phys. Chem. C* **119**, 7400 (2015).

[20] Y. Osumi, T. Yamada, Y. Ie, and H. S. Kato, *J. Phys. Chem. C* **123**, 16127 (2019).

[21] S. Kaneko, E. Montes, S. Suzuki, S. Fujii, T. Nishino, K. Tsukagoshi, K. Ikeda, H. Kano, H. Nakamura, H. Vázquez, and M. Kiguchi, *Chem. Sci.* **10**, 6261 (2019).

[22] J. Kestell, R. Abuflaha, M. Garvey and W. T. Tysoe, *J. Phys. Chem. C* **119**, 23042 (2015).

[23] C. W. Bauschlicher and A. Ricca, *Chem. Phys. Lett.* **367**, 90 (2003).

[24] H. Häkkinen, *Nat. Chem*. **4**, 443 (2012).

[25] R. Nuzzo and D. Allara, *J. Am. Chem. Soc.* **105**, 4481 (1983).

[26] R. Nuzzo, F. Fusco, and D. Allara, *J. Am. Chem. Soc*. **109**, 2358 (1987).

[27] R. Nuzzo, L. Dubois, and D. Allara, *J. Am. Chem. Soc.* **112**, 558 (1990).

[28] M. D. Porter, T. Bright, D. Allara, and C. Chidsey, *J. Am. Chem. Soc.* **109**, 3559 (1987).

[29] C. Chen, M. Mrksich, S. Huang, G. Whitesides, and D. Ingber, *Science* **276**,1425 (1997).

[30] X. Jiang, R. Ferrigno, M. Mrksich, and G. Whitesides, *J. Am. Chem. Soc*. **125**, 2366 (2003).

[31] X. Jiang, D. Bruzewicz, A. Wong, M. Piel, and G. Whitesides, *Proc. Nat. Acad. Sci*. **102**, 975 (2005).

[32] R. L. McCreery, *Chem. Mater*. **16**, 4477 (2004).

[33] K. Sotthewes, V. Geskin, R. Heimbuch, A. Kumar, and H. J. W. Zandvliet, *APL Mater*. **2**, 010701 (2014).

[34] E. Pensa, E. Cortés, G. Corthey, P. Carro, C. Vericat, M. H. Fonticelli, G. Benítez, A. A. Rubert, and R. C. Salvarezza, *Acc. Chem. Res*. **45**, 1183 (2012).

[35] Y. Han, M. S. Maglione, V. Diez Cabanes, J. Casado-Montenegro, X. Yu, S. K. Karuppannan, Z. Zhang, N. Crivillers, M. Mas-Torrent, C. Rovira, J. Cornil, J. Veciana, and C. A. Nijhuis, *ACS Appl. Mater. Interfaces* **12**, 55044 (2020).

[36] N. K. Chaki and K. Vijayamohanan, *Biosens. Bioelectron*. **17**, 1 (2002).

[37] G. Heimel, L. Romaner, E. Zojer, and J.-L. Bredas, *Acc. Chem. Res*. **41**, 721 (2008).

[38] J. Z. Gao, L. Tang, S. Holmes, F. S. Li, R. E. Palmer, and Q. Guo, *Nanoscale* **8**, 19787 (2016).

[39] Y. Xia and G. M. Whitesides, *Annu. Rev. Mater. Sci*. **28**, 153 (1998).

[40] C. Vericat, M. Vela, G. Benitez, P. Carro, and R. Salvarezza, *Chem. Soc. Rev*. **39**, 1805 (2010).

[41] A. Ulman, *Chem. Rev.* **96**, 1533 (1996).

[42] J. C. Love, L. A. Estroff, J. K. Kriebel, R. G. Nuzzo, and G. M. Whitesides, *Chem. Rev.* **105**, 1103 (2005).

[43] A. de Melo Souza, I. Rungger, R. B. Pontes, A. R. Rocha, A. J. R. da Silva, U. Schwingenschlöegl, and S. Sanvito, *Nanoscale* **6**, 14495 (2014).

[44] A. Nitzan and M. A. Ratner, *Science* **300**, 1384 (2003).

[45] M. Kiguchi, S. Miura, K. Hara, M. Sawamura, and K. Murakoshi, *Appl. Phys. Lett.* **89**, 213104 (2006)

[46] S. Hong, R. Reifenberger, W. Tian, S. Datta, J. Henderson, and C. P. Kubiak, *Superlattices Microstruct.* **28**, 289 (2000).

[47] S. Sato, K. Namba, K. Hara, A. Fukuoka, K. Murakoshi, K. Uosaki, and K. Ikeda, *J. Phys. Chem. C* **120**, 2159 (2016).

[48] K. Ikeda, N. Fujimoto, and K. Uosaki, *J. Phys. Chem. C* **118**, 21550 (2014).

[49] S. Sato, S. Iwase, K. Namba, T. Ono, K. Hara, A. Fukuoka, K. Uosaki, and K. Ikeda, *ACS Nano* **12**, 1228 (2018).

[50] C. E. Smith, Z. Xie, I. Baldea, and C. D. Frisbie, *Nanoscale* **10**, 964 (2018).

[51] A. Tsunoi, G. Lkhamsuren, E. A. Q. Mondarte, S. Asatyas, M. Oguchi, J. Noh, and T. Hayashi, *J. Phys. Chem. C* **123**, 13681 (2019).

[52] A. Ge, P. E. Videla, G. L. Lee, B. Rudshteyn, J. Song, C. P. Kubiak, V. S. Batista, and T. Lian, *J. Phys. Chem. C* **121**, 18674 (2017).

[53] J. Ahn, S. Shi, B. Vannatter, and D. Qin, *J. Phys. Chem. C* **123**, 21571 (2019).

[54] E. de la Llave, R. Clarenc, D. J. Schiffrin, and F. J. Williams, *J. Phys. Chem. C* **118**, 468 (2014).

[55] J. J. Hickman, C. Zou, D. Ofer, P. Harvey, M. S. Wrighton, P. E. Laibinis, C. D. Bain, and G. M. Whitesides, *J. Am. Chem. Soc*. **111**, 7271 (1989).

[56] J. M. Beebe, V. B. Engelkes, L. L. Miller, and C. D. Frisbie, *J. Am. Chem. Soc*. **124**, 11268 (2002).

[57] J. J. Stapleton, T. A. Daniel, S. Uppili, O. M. Cabarcos, J. Naciri, R. Shashidhar, and D. L. Allara, *Langmuir*, **21**, 11061 (2005).

[58] T. Zaba, A. Noworolska, C. M. Bowers, B. Breiten, G. M. Whitesides, and P. Cyganik, *J. Am. Chem. Soc*. **136**, 11918 (2014).

[59] D. Fracasso, S. Kumar, P. Rudolf, and R. C. Chiechi, *RSC Adv.* **4**, 56026 (2014).

[60] C. M. Crudden, J. H. Horton, I. I. Ebralidze, O. V. Zenkina, A. B. McLean, B. Drevniok, Z. She, H.-B. Kraatz, N. J. Mosey, T. Seki, E. C. Keske, J. D. Leake, A. Rousina-Webb, G. Wu, *Nat. Chem.* **6**, 409 (2014).

[61] G. Wang, A. Rehling, S. Amirjalayer, M. Knor, J. B. Ernst, C. Richter, H.-J. Gao, A. Timmer, H.-Y. Gao, N. L. Doltsinis, F. Glorius, H. Fuchs, *Nat. Chem.* **9**, 152 (2017).

[62] G. E. Poirier and E. D. Pylant, *Science* **272**, 1145 (1996).

[63] N.-Y. Cui, C. Liu, and W. Yang, *Surf. Interface Anal.* **43**, 1082 (2011).

[64] A. Imanishi, R. Omoda, and Y. Nakato, *Langmuir* **22**, 1706 (2006).

[65] J. Wiedemair, L. Le Thi Ngoc, A. van den Berg, and E. T. Carlen, *J. Phys. Chem. C* **118**, 11857 (2014).

[66] M. Beccari, A. Kanjilal, M. G. Betti, C. Mariani, L. Floreano, A. Cossaro and V. Di Castro, *J. Electron Spectrosc. Relat. Phenom*. **172**, 64 (2009).

[67] A. Patnaik, K. K. Okudaira, S. Kera, H. Setoyama, K. Mase, and N. Ueno, *J. Chem. Phys*. **122**, 154703 (2005)

[68] T. L. Freeman, S. D. Evans and A. Ulman, *Langmuir* **11**, 4411 (1995).

[69] M. C. Bourg, A. Badia and R. B. Lennox, *J. Phys. Chem. B* **104**, 6562 (2000).

[70] N. Bloembergen and P. S. Pershan, Phys. Rev. 128, 606 (1962.)

[71] Y. R. Shen, *Nature*, **337**, 519 (1989).

[72] S. Nihonyanagi, S. Yamaguchi and T. Tahara, *Chem. Rev.* **117**, 10665 (2017).

[73] E. H. G. Backus, J. D. Cyran, M. Grechko, Y. Nagata and M. Bonn, *J. Phys. Chem. A* **122**, 2401 (2018).

[74] J. E. Laaser, W. Xiong, and M. T. Zanni, *J. Phys. Chem. B* **115**, 2536 (2011).

[75] C. Hess, M. Wolf, S. Roke, and M. Bonn, *Surf. Sci.* **502**, 304 (2002).

[76] A. Ghosh, M. Smits, J. Bredenbeck, N. Dijkhuizen, and M. Bonn, *Rev. Sci. Instrum.* **79**, 093907 (2008).

[77] A. Tuladhar, Z. A. Chase, M. D. Baer, B. A. Legg, J. Tao, S. Zhang, A. D. Winkelman, Z. Wang, C. J. Mundy, J. J. De Yoreo, and H.-F Wang, *J. Am. Chem. Soc*. **141**, 2135 (2019).

[78] S. M. Piontek, M. DelloStritto, B. Mandal, T. Marshall, M. L. Klein, and E. Borguet, *J. Am. Chem. Soc*. **142**, 12096 (2020).

[79] T. Weidner, N. F. Breen, K. Li, G. P. Drobny, and D. G. Castner, *Proc Natl Acad Sci USA* **107**, 13288 (2010).

[80] X-Y, Zhu, *Surf. Sci. Rep*. **56**, 1 (2004).

[81] M. Ito, H. Noguchi, K. Ikeda and K. Uosaki, *Phys. Chem. Chem. Phys.* **12**, 3156 (2010).

[82] M. Weinelt, *Journal of Physics: Condensed Matter*. **14**, R1099 (2002).

[83] P. Szymanski, S. Garrett-Roe, and C. B. Harris, *Prog. Surf. Sci*. **78**, 1 (2005).

[84]. A. Stolow, A. E. Bragg, and D. M. Neumark, *Chem. Rev*, **104**, 1719 (2004).

[85] M. Shibuta, N. Hirata, R. Matsui, T. Eguchi and A. Nakajima, *J. Phys. Chem. Lett*. **3**, 981 (2012).

[86] N. Hirata, M. Shibuta, R. Matsui, and A. Nakajima, *J. Phys. Chem. C* **116**, 13623 (2012).

[87] M. Shibuta, N. Hirata, T. Eguchi, and A. Nakajima, *ACS Nano* **11**, 4307 (2017).

[88] H. S. Kato, Y. Murakami, Y. Kiriyama, R. Saitoh, T. Ueba, T. Yamada, Y. Ie, Y. Aso, and T. Munakata, *J. Phys. Chem. C* **119**, 7400 (2015).

[89] V. Ganesh, R. R. Pandey, B. D. Malhotra, V. Lakshminarayanan, *J. Electroanal. Chem*. **619**, 87 (2008).

[90] J. Stettner and A. Winkler, *Langmuir* **26**, 9659 (2010).

[91] R. G. Nuzzo, B. R. Zegarski and L. H. Dubois, *J. Am. Chem. Soc*. **109**, 733 (1987).

[92] S. Holloway, B. I. Lundqvist, J. K. Nørskov (1984) Electronic factors in catalysis. Proceedings of the Eighth Conference on Catalysis (Springer, Berlin), Vol IV, p 85.

[93] B. Hammer and J. K. Nørskov, *Nature* **376**, 2238 (1995).

[94] P. W. Anderson, *Phys. Rev.* **124**, 41 (1961).

[95] J. P. Muscat and D. M. Newns, *Phys. Rev. Lett.* **43**, 2025 (1979).

[96] J. P. Muscat and D. M. Newns, *Prog. in Surf. Sci*. **9**, 1 (1978).

[97] T. Grimley, *Proc. Phys. Soc*. **90**, 751 (1967).

[98] T. Grimley, *Prof. Phys. Soc.* **72**, 103 (1958).

[99] C. D. Lindstrom and X.-Y. Zhu, *Chem. Rev.* **106**, 4281 (2006).

[100] HANDBOOK OF SURFACE SCIENCE VOLUME 2 Electronic Structure, K. Horn and M. Scheffler).

[101] R. F. W. Bader, *Chem. Rev.* **91**, 893 (1991).

[102] R. F. W. Bader, *Atoms in Molecules: A Quantum Theory*, Oxford University Press, USA, 1994.

[103] R. F. W. Bader, *Acc. Chem. Res.* **18**, 9 (1985).

[104] R. F. W. Bader. In: P. v. Schleyer, (Ed.). *Encyclopedia of Computational Chemistry.* (John Wiley and Sons, Chichester, U.K., 1998), pp. 64−86.

[105] G. Blyholder, *J. Phys. Chem.* **68**, 2772 (1964).

Chapter 2

Theoretical Methods

In this Chapter, the basic theoretical background and key concepts used in the computation of subsequent chapters will be introduced. Specifically, at the beginning, the Born-Oppenheimer Approximation and density functional theory (DFT) are reviewed. The solution of the DFT problem will be given in the second part. Then, to meet the requirement of our adsorbate-surface system calculation which is specific to this dissertation, the periodic potential and plane-wave basis set will be presented. Lastly, a conceptual review of pseudopotential, in particular, the projector-augmented wave (PAW) and norm-conserving pseudopotentials will be given in the final section.

2.1 Born-Oppenheimer Approximation

Ab-initio calculations of chemical properties of surface and interface environments which belong to many-body system composed of electrons and nuclei as well as the surface always starts from the many-body Schrödinger equation. Such equation describing the chemical properties and including the Hamiltonian which contains the kinetic energy of all particles within the surface and their interaction energies is the time-dependent Schrödinger equation (TD−SE) [1]:

$$i\hbar\frac{\partial\Phi(r,R;t)}{\partial t}=\left(-\sum_{\mu}\frac{\hbar^2}{2M_{\mu}}\nabla^2_{\mathbf{R}_{\mu}}-\sum_{i}\frac{\hbar^2}{2m}\nabla^2_{\mathbf{r}_i}+V(r,R)\right)\Phi(r,R;t) \tag{2.1}$$

$\Phi(r,R;t)$: many-body time-dependent wavefunction;

$r\equiv(\mathbf{r}_1,\dots,\mathbf{r}_n)$, $R\equiv(\mathbf{R}_1,\dots,\mathbf{R}_N)$: notations of electrons and nuclei, respectively;

M_{μ}, m: mass of nucleus and electron;

μ, i: indices run over nuclei and electrons, respectively;

ħ: reduced Planck constant equaling to h/2π where h is the Planck's constant

$\Phi(r, R; t)$ depends on the spatial coordinates of all electrons and ions and on time. It contains the complete information of the studied system. Most important properties would be available once a $\Phi(r, R; t)$ were known. Therefore, the most direct way of studying the time-dependent behavior of an atom or molecule is to solve the TD−SE.

The term in the bracket stands for the Hamiltonian operator, *H*. This operator consists of a kinetic energy term (the first two parts) and a potential energy term (the final part). The potential energy term, $V(r, R)$ describes the interaction between all particles in a considered electron-ion system, and can be further expanded as:

$$V(r, R) = -\sum_{i,\mu} \frac{Z_I e^2}{|\mathbf{r}_i - \mathbf{R}_\mu|} + \frac{1}{2}\sum_{i \neq j} \frac{e^2}{|\mathbf{r}_i - \mathbf{r}_j|} + \frac{1}{2}\sum_{\mu \neq \nu} \frac{Z_\mu Z_\nu e^2}{|\mathbf{R}_\mu - \mathbf{R}_\nu|} \quad (2.2)$$

In this equation, the indices μ, ν and i, j run over nuclei and electrons, respectively. e is the elementary charge, Z_μ and Z_ν represent the atomic number of each ion. The three terms in the right side describe the electron-ion interaction, electron-electron interaction and ion-ion interaction, respectively.

A defined electron-ion Hamiltonian doesn't depend on the time. The wavefunction $\Phi(r, R; t)$ will keep static in this case. Thus the TD−SE Eq. (2.1) can be simplified to the time-independent or static form:

$$H\Phi(r, R) = E\Phi(r, R) \quad (2.3)$$

The equation can be treated as an eigenvalue problem where $\Phi(r, R)$ and E are the eigenfunctions and eigenvalues. Solving this eigenvalue equation can give the desirable information under study. However, in practical case, it is still very tough to obtain the analytical

solution for system bigger than the simplest hydrogen atom, and is therefore cannot work for surface systems.

One famous approximation for simplifying this problem is the Born-Oppenheimer approximation (BOA) [2]. To be concise, since nucleus is much heavier (1836 : 1) than the light electron, time scale associated with the nuclear motion is much longer than that of the electrons, we can assume the electrons adapt to the nuclear motion instantaneously and the motion of the electrons is entirely decoupled from the motion of the nuclei, and their degrees of freedom can therefore be separately treated. The nuclear motion can be treated classically, considering that they are affected by a potential created by the electrons.

The problem then becomes the solution of electronic problem, and can be written as:

$$\left(-\frac{\hbar^2}{2m}\sum_i \nabla^2_{\mathbf{r}_i} + V(r,R)\right)\Psi_R(r) = E(R)\Psi_R(r) \tag{2.4}$$

for given R. The eigenvalue term $E(R)$ represents the total energy or potential energy surface (PES). The nuclear motion is determined by $E(R)$, its global minimum corresponds to the ground state of the entire system.

2.2 Density Functional Theory

After including the BOA into the electronic problem, the dimensionality of the eigenfunctions $\Phi(r,R)$ then decreases from the total number of electrons and nuclei to only the electronic degrees of freedom. However, the electron number in surface system is still large, causing the eigenvalue problem still very difficult to solve. Birth of density functional theory (DFT) help us to overcome this issue. The basic idea behind the DFT is to use the electron density instead of the electron wavefunction to treat the many-body system [3, 4]. In this way, the degrees of freedom is reduced

from $3\mathbf{n_e}$ to 3. As the currently most common first principles electronic structure theory, DFT has been widely used in the field of quantum chemistry.

2.2.1 Hohenberg−Kohn theorem

We now turn to the central point of DFT method, which is called the Hohenberg-Kohn theorem [3, 4]. This theorem states there is a conversely unique correspondence between a potential $V(r, R)$ and the ground-state electron density $n(\mathbf{r})$ which is defined as

$$n(\mathbf{r}) = N\int |\Psi(\mathbf{r}, \mathbf{r}_2, \dots \mathbf{r}_N)|^2 d\mathbf{r}_2 \dots d\mathbf{r}_N \tag{2.5}$$

The consequence of the Hohenberg-Kohn theorem is that important observables, like the ground state energy can be exacted based on the electron energy functional of the entire system with respect to the electron density $n(\mathbf{r})$:

$$E[n(\mathbf{r})] = F[n(\mathbf{r})] + \int n(\mathbf{r})V(\mathbf{r})d\mathbf{r} \tag{2.6}$$

$F[n(\mathbf{r})]$: a universal functional of the density;

$V(\mathbf{r})$: nuclear or external potential on each electron

The electron energy functional $E[n(\mathbf{r})]$, is minimized to give the ground state energy. This minimization of energy functional is always infeasible, due to the unknown exact dependence of the functional on electron density $n(\mathbf{r})$.

2.2.2 Kohn−Sham equation

To make the Hohenberg-Kohn theorem in a more practical way, Kohn and Sham proposed the Kohn-Sham (KS) approach. In this approach, the exact electron density $n(\mathbf{r})$ is constructed using an auxiliary set of non-interacting electrons moving in the effective potential field of electron-nuclei system [5].

The non-interacting orbitals ψ_i are introduced in this situation, and the electron density can be written as

$$n(\mathbf{r}) = \sum_i |\psi_i(\mathbf{r})|^2, \langle \psi_i \mid \psi_j \rangle = \delta_{ij} \tag{2.7}$$

The energy functional E can be expressed as

$$E = T_s[n(\mathbf{r})] + E_H[n(\mathbf{r})] + E_{xc}[n(\mathbf{r})] + \int n(\mathbf{r}) V(\mathbf{r}) d\mathbf{r} \tag{2.8}$$

where the first term $T_s[n(\mathbf{r})]$ in the right side is the kinetic energy of non-interacting electrons and can be written as

$$T_s[n(\mathbf{r})] = -\frac{\hbar^2}{2m} \sum_i \int \psi_i^*(\mathbf{r}) \nabla^2 \psi_i(\mathbf{r}) d\mathbf{r} \tag{2.9}$$

The second term $E_H[n(\mathbf{r})]$ is the Hartree energy, while the third term $E_{xc}[n(\mathbf{r})]$ is the exchange-correlation energy. It can be found that minimizing the energy functional E with respect to the can ψ_i leads to the Schrödinger equation for non-interacting electrons in an effective potential:

$$\left(-\frac{\hbar^2}{2m}\nabla^2 + V(\mathbf{r}) + V_H(\mathbf{r}) + V_{xc}(\mathbf{r})\right)\psi_i(\mathbf{r}) = \epsilon_i \psi_i(\mathbf{r}) \tag{2.10}$$

The term in the bracket is the KS Hamiltonian. The $V(\mathbf{r})$, $V_H(\mathbf{r})$ and $V_{xc}(\mathbf{r})$ represent the external potential created by the nuclei, Hartree potential and the exchange-correlation potentials, respectively. The Hartree potential and the exchange-correlation potentials can be expressed as

$$V_H(\mathbf{r}) = \frac{\delta E_H[n(\mathbf{r})]}{\delta n(\mathbf{r})} = e^2 \int \frac{n(\mathbf{r}')}{|\mathbf{r}-\mathbf{r}'|} d\mathbf{r}' \ , V_{xc}(\mathbf{r}) = \frac{\delta E_{xc}[n(\mathbf{r})]}{\delta n(\mathbf{r})} \tag{2.11}$$

It can be shown that these two terms also depend on the orbital ψ_i via the electron density $n(\mathbf{r})$. ϵ_i and $\psi_i(\mathbf{r})$ are the eigenvalues and eigenvectors of the KS Hamiltonian, they can also be treated as the KS energies and orbitals.

Diagonalization of the KS Hamiltonian results in the KS orbital energy ϵ_i, and eigenvector $\psi_i(\mathbf{r})$. Summation of the KS orbital energy ϵ_i is not the total energy, the total energy should be written as

$$E = \sum_i \epsilon_i - E_H[n(\mathbf{r})] - \int n(\mathbf{r})V_{xc}(\mathbf{r})d\mathbf{r} + E_{xc}[n(\mathbf{r})] \quad (2.12)$$

$E_{xc}[n(\mathbf{r})]$ is the exchange-correlation term. We can solve the KS equation via a self-consistent way as following procedure

$$n^a(\mathbf{r}) \longrightarrow V_{\text{eff}}^a(\mathbf{r}) \longrightarrow \text{ KS equations } \longrightarrow [\psi_i(\mathbf{r})]^{a+1} \longrightarrow n^{a+1}(\mathbf{r})$$

$n^a(\mathbf{r})$ is the electron density in the a-th step. The self-consistent run will complete until the desired convergence condition is satisfied. By employing a set of KS orbitals, we replace the problem of solving eigenvalue of system with interacting electrons by the independent electrons which move in an effective field. Once the functional dependence of the effective potential (mainly the exchange-correlation potential) was known, the electron density and energy can be thereby obtained from the KS equations.

2.2.3 exchange-correlation functionals

To turn the DFT into an applicable tool in practical way, we have to make viable approximations on the exchange-correlation functionals $E_{xc}[n(\mathbf{r})]$. There are several approximations for the treatment of exchange-correlation functionals, including generalized gradient approximation (GGA) [4−7] and local density approximation (LDA) [5].

local density approximation

In the LDA approximation, the energy functional is replaced by a function of the local density $n(\mathbf{r})$.

$$E_{xc} = \int n(\mathbf{r})\epsilon_{xc}(n(\mathbf{r}))d\mathbf{r} \quad (2.13)$$

here, the $\epsilon_{xc}(n)$ is the exchange-correlation energy density of the homogeneous electron gas. An exact treatment for uniform density can be offered by LDA, thus LDA is suitable for density that varies slowly, while it is not suitable for not uniform density, such as atoms. This leads to remarkable error sometimes for approximating the functionals.

generalized gradient approximation

In the LDA, there is only density at the point **r** will be used for the exchange-correlation functional. GGA improves the LDA by including more functionals that depend upon the local density. The GGA is currently the basic functionals in most calculations. There are some other approximations that are generally more accurate and more time-consuming, such like meta GGA, and hybrid functionals have been proposed. In this thesis, we use the GGA proposed by Perdew, Burke and Ernzerhoff [8, 9] due to the consideration price-performance ratio.

2.3 Plane-Wave Basis Set and Pseudopotentials

In this thesis, the main simulation model is the periodic solid surface which always possess a great challenge to quantum chemical simulation due to its taxing computational complexity. To that end, we now focus on the infinite periodic systems, which is specific to the surface and interface systems in this thesis. The periodicity in surface systems satisfies the periodic condition upon the effective and KS wavefunctions. For a slab of crystal composed of $\mathcal{N} = \mathcal{N}_1\mathcal{N}_2\mathcal{N}_3$ unit cells, the one-electron states $\psi(\mathbf{r})$ obeys the periodic boundary conditions (PBC)

$$\psi(\mathbf{r} + \mathcal{N}_1\mathbf{R}_1) = \psi(\mathbf{r} + \mathcal{N}_2\mathbf{R}_2) = \psi(\mathbf{r} + \mathcal{N}_3\mathbf{R}_3) = \psi(\mathbf{r}). \tag{2.14}$$

r is the position vector

By using the Bloch's theorem [10], the one-electron states can then be written as

$$\psi_{i,\mathbf{k}}(\mathbf{r}) = e^{i\mathbf{k}\cdot\mathbf{r}}u_{i,\mathbf{k}}(\mathbf{r}) \tag{2.15}$$

i is the electronic band number, $\mathbf{k}$ is the electronic wave vector in the unit cell of the reciprocal lattice. $u_{i,\mathbf{k}}(\mathbf{r})$ is the periodic part of the KS wavefunction and is translationally invariant, this means

$$u_{i,\mathbf{k}}(\mathbf{r}+\mathbf{R}) = u_{i,\mathbf{k}}(\mathbf{r}) \tag{2.16}$$

During the implementation of DFT method, the non-interacting KS orbitals should be expanded in a finite set of basis functions. A variety of basis sets can be selected to expand the KS orbitals, including the localized basis sets (Gaussian-type atomic orbitals, linear combinations of atomic orbitals), the delocalized basis set (plane wave), as well as the mixed basis sets. In this thesis, we use the plane-wave (PW) basis set to expand the KS wavefunctions.

A plane wave basis set is defined as

$$\langle \mathbf{r} \mid \mathbf{k}+\mathbf{G} \rangle = \frac{1}{\sqrt{\mathcal{N}\Omega}} e^{i(\mathbf{k}+\mathbf{G})\cdot\mathbf{r}}, \frac{\hbar^2}{2m}|\mathbf{k}+\mathbf{G}|^2 \leq E_{cut} \tag{2.17}$$

where Ω is the unit cell volume, $\mathcal{N}\Omega$ is the crystal volume, E_{cut} is the cutoff on the kinetic energy of PWs. $\mathbf{G}$ is the wave vector of the reciprocal lattice vectors. When E_{cut} approaches to infinite large, the PW basis set is complete.

A PW basis set can work with the Fourier expansion coefficients $c_{i,\mathbf{k}+\mathbf{G}}$

$$|\psi_i\rangle = \sum_{\mathbf{G}} c_{i,\mathbf{k}+\mathbf{G}} |\mathbf{k}+\mathbf{G}\rangle$$

$$c_{i,\mathbf{k}+\mathbf{G}} = \langle \mathbf{k}+\mathbf{G} \mid \psi_i \rangle = \frac{1}{\sqrt{\mathcal{N}\Omega}} \int \psi_i(\mathbf{r}) e^{-i(\mathbf{k}+\mathbf{G})\cdot\mathbf{r}} d\mathbf{r} = \tilde{\psi}_i(\mathbf{k}+\mathbf{G}) \tag{2.18}$$

Using means of Fast Fourier Transform, transformation between real space representation and reciprocal space representation can be constructed. The plane-wave basis set is naturally suited to the periodic system. However, the PW basis set is not the practical basis set for performing electronic structure calculations. One essential reason is due to the highly localized nature of the core electrons, which means a large number of PW basis sets should be used to expand the wave functions near the core electrons. Such a large number of PW basis set makes the computation

very expensive. Another reason is that, in general, the effective potential is a functional of the valence electron density instead of the total exact electron density, contributions of the core electrons to the bonding and other solid-state properties can be usually ignored compared to those of valence electrons. As a consequence, it is necessary to replace the atomic potential of the core electrons with a pseudopotential (PP). Within the PP approximation, the core region is effectively freezed while all degrees of freedom have been removed. On the other hand, the full Coulomb potential of nucleus is not used for treating the valence electrons, alternatively, a weaker PP which can smooth the oscillatory core part of potential and wave functions is used.

There are several PPs can work for replacing the core potential: norm-conserving pseudopotentials [11, 12], ultra-soft (Vanderbilt) pseudopotentials [13] and projector-augmented wave (PAW) method [14]. Determination an appropriate PP for the studied system should consider the properties of the pseudopotentials. The most important one among all properties is the transferability. The transferability requires the PPs can reproduce the scattering properties of the nucleus plus core electrons in various different chemical environments (isolated atoms, molecules, crystals, etc.). The plane-wave basis set, pseudopotential method and other methodologies in this Chapter have been implemented in several extensively used DFT packages, including Vienna ab initio simulation package (VASP) [15−18] and Quantum Espresso (QE) [19, 20] which have been employed to obtain the results of this Thesis.

2.4 Specific Implementation in This Study

In this section, based on the PW basis set, the specific implementation of natural bond orbital (NBO) algorithm, anharmonic vibrational spectra on periodic system will be concisely introduced. Another utilized method–artificial force induced reaction method implemented in the global reaction route mapping is also presented.

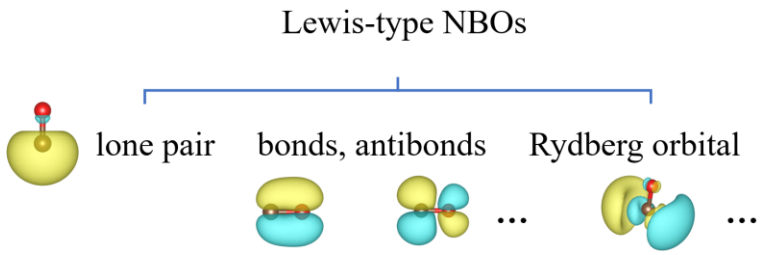

Figure 2.1. A simple picture showing the basic components derived from the NBO algorithm, the CO molecule has been used as the model.

To give a concise description of each method, we start from the introduction of NBO analysis which can provide a purely localized real space representation of bonding interaction. It can replace the delocalized molecular orbitals with a set of localized bonding orbitals, antibonding orbitals, lone pair orbitals as the linear combinations of orthogonal hybrid orbitals centered on atoms, with a strong connection to the Lewis structure [21], as shown in the **Figure 2.1**. The NBO analysis requires a density matrix in a localized atom-centered basis set. However, for calculation in periodic surface systems, the electronic wave function is given in the reciprocal space, which conflicts with the localized, real space representation in traditional NBO method. To include the periodicity of the surface system, we follow with the periodic NBO method using the same algorithm presented by B. D. Dunnington and J. R. Schmidt in 2012 [22]. Firstly, a projection of plane wave bands into atomic orbital basis sets proposed by Sanchez-Portal et al. [23, 24] has been

employed. Then, beginning with a set of atom centered, atomic orbital (AO) basis functions, the corresponding crystalline AOs. The density and overlap matrices obtained from the original AO basis are used for calculation of natural atomic orbitals (NAOs). After this AO-to-NAO transformation, the NAOs are then used for the periodic search of one-center lone pairs, two-center bonding, antibonding natural bond orbitals, as well as the Rydberg orbitals.

Then, we give an introduction to the anharmonic vibrational spectra calculation used in this thesis. Generally, there are two approaches that can be used for frequency calculation. The first approach is based on the calculation of the second-order derivative of the potential energy surface with respect to the geometry (Hessian matrix) using the finite differences within the harmonic approximation. The second one is based on the calculation of the Hessian matrix and Born effective charges of the studied system. Herein, the calculation of anharmonic vibrational spectra in this thesis is following with the method presented by José A. Garrido Torres et al. in 2019 [25]. The intensity of the spectra is obtained by an analytic expression for the Morse potential. Such expression provides the anharmonic corrections for fundamental transitions using the Born effective charges. During the practical calculation, a series of single-point calculation (the energy is along the dimensionless coordinates of each mode) are firstly performed to obtain the one-dimensional potential energy surface (1D-PES) of each mode. For each mode, ten equally spaced ten single points have been selected. To keep different modes are comparable, the mass-weighted normal coordinates should be transformed into dimensionless coordinates, which is similar to the method proposed by Gregurick et al. [26]. The obtained 1D-PES of each studied mode is then fitted to a Morse potential

$$V(x) = D\left(1 - e^{-a(x-r_e)}\right)^2 \tag{2.19}$$

x is the displacement from the equilibrium state, D, a and r_e are constants determined from the DFT calculations. The nonlinear least-squares algorithm is used for the fit. The constants obtained after fitting are used for the calculation of the relative anharmonic correction factors. The calculated spectra are finally broadened using a Gaussian profile. Such method have provided accurate theoretical calculations of the vibrational features of molecules at metal surfaces.

The final important method featured in this thesis is the artificial force induced reaction (AFIR) [27−29] implemented in the global reaction route mapping (GRRM) algorithm [27, 30]. This method can search a AFIR path based on the random initial reactant. Finding the AFIR path is induced by an artificial force, and the geometrical change is by minimizing a AFIR function. All obtained AFIR paths are then analyzed to obtain the actual TSs that connect the AFIR paths. An important parameter in the AFIR method is the force parameter γ which determines the biggest barrier of the predicted TSs. For instance, the γ = 3.109 eV (300 kJ/mol) means that only the TSs with a barrier less than 3.109 eV can be obtained.

2.5 References

[1] E. Schrödinger, *Ann. Phys*. **384**, 361 (1926).

[2] M. Born and R. Oppenheimer, *Ann. Phys*. **389**, 457 (1927)

[3] P. Hohenberg and W. Kohn, *Phys. Rev*. **136**, B864 (1964)

[4] W. Kohn, Rev. *Mod. Phys.* **71**, 1253 (1999)

[5] W. Kohn and L. J. Sham, *Phys. Rev*. **140**, A1133 (1965)

[6] D. C. Langreth and M. J. Mehl, *Phys. Rev. B* **28**, 1809 (1983)

[7] A. D. Becke, *Phys. Rev. A*, **38**, 3098 (1988)

[8] J. P. Perdew, K. Burke, and M. Ernzerhof, Phys. Rev. Lett. **77**, 3865 (1996)

[9] J. P. Perdew, K. Burke and M. Ernzerhof, *Phys. Rev. Lett.* **78**, 1396 (1997).

[10] F. Bloch, *Z. Phys.*, **52**, 555 (1929).

[11] D. R. Hamann, M. Schlüter, and C. Chiang, *Phys. Rev. Lett*. **43**, 1494 (1979).

[12] N. Troullier and José Luís Martins, *Phys. Rev. B* **43**, 1993 (1991).

[13] D. Vanderbilt, *Phys. Rev. B* **41**, 7892 (1990).

[14] P. E. Blöchl, *Phys. Rev. B* **50**, 17953 (1994)

[15] G. Kresse and J. Hafner, *Phys. Rev. B* **47**, 558 (1993).

[16] G. Kresse and J. Hafner, *Phys. Rev. B* **49**, 14251 (1994).

[17] G. Kresse and J. Furthmüller, *Phys. Rev. B* **54**, 11169 (1996).

[18] G. Kresse and J. Furthmüller, *Comput. Mater. Sci.* **6**, 15 (1996).

[19] P. Giannozzi, S. Baroni, N. Bonini, M. Calandra, R. Car, C. Cavazzoni, D. Ceresoli, G. L. Chiarotti, M. Cococcioni, I. Dabo, A. D. Corso, S. de Gironcoli, S. Fabris, G. Fratesi, R. Gebauer, U. Gerstmann, C. Gougoussis, A. Kokalj, M. Lazzeri, L. Martin-Samos, N. Marzari, F. Mauri, R. Mazzarello, S. Paolini, A. Pasquarello, L. Paulatto, C. Sbraccia, S. Scandolo, G. Sclauzero, A.

Seitsonen, A. Smogunov, P. Umari, and R. Wentzcovitch, *J. Phys.: Condens. Matter* **21**, 395502 (2009).

[20] P. Giannozzi, O. Andreussi, T. Brumme, O. Bunau, M. B. Nardelli, M. Calandra, R. Car, C. Cavazzoni, D. Ceresoli, M. Cococcioni, N. Colonna, I. Carnimeo, A. D. Corso, S. de Gironcoli, P. Delugas, R. A. DiStasio, Jr., A. Ferretti, A. Floris, G. Fratesi, G. Fugallo, R. Gebauer, U. Gerstmann, F. Giustino, T. Gorni, J. Jia, M. Kawamura, H.-Y. Ko, A. Kokalj, E. Kkbenli, M. Lazzeri, M. Marsili, N. Marzari, F. Mauri, N. L. Nguyen, H.-V. Nguyen, A. O. de-la Roza, L. Paulatto, S. Ponc, D. Rocca, R. Sabatini, B. Santra, M. Schlipf, A. P. Seitsonen, A. Smogunov, I. Timrov, T. Thonhauser, P. Umari, N. Vast, X. Wu, and S. Baroni, *J. Phys.: Condens. Matter* **29**, 465901 (2017).

[21] F. Weinhold and C. Landis, *Valency and Bonding–A Natural Bond Orbital Donor-Acceptor Perspective*; Cambridge University Press: Cambridge, 2005; pp 1−44.

[22] B. D. Dunnington and J. R. Schmidt, *J. Chem. Theory Comput.* **8**, 1902 (2012).

[23] D. Sanchez-Portal, E. Artacho, and J. M. Soler, *Solid State Commun*. **95**, 685 (1995).

[24] D. Sanchez-Portal, E. Artacho, and J. M. Soler, *J. Phys.: Condens. Matter* **8**, 3859 (1996).

[25] J. A. Garrido Torres, J. P. Götze, F. Grillo, N. V. Richardson, H. Früchtl, C. A. Hooley and R. Schaub, *Phys. Rev. B* **100**, 035433 (2019).

[26] S. K. Gregurick, G. M. Chaban, and B. R. Gerber, *J. Phys. Chem. A* **106**, 8696 (2002).

[27] S. Maeda, K. Ohno, and K. Morokuma, *Phys. Chem. Chem. Phys.* **15**, 3683 (2013).

[28] S. Maeda, T. Taketsugu, and K. Morokuma, *J. Comput. Chem.* **35**, 166 (2014).

[29] S. Maeda, Y. Harabuchi, M. Takagi, T. Taketsugu, and K. Morokuma, *Chem. Rec.* **16**, 2232 (2016).

[30] S. Maeda, Y. Harabuchi, M. Takagi, K. Saita, K. Suzuki, T. Ichino, Y. Sumiya, K. Sugiyama, and Y. Ono, *J. Comput. Chem*. **39**, 233 (2018).

Chapter 3

Substituent Effect on Aryl Isocyanides Adsorbed on Pt Surface

We have introduced different SAMs adsorbed on metal substrates and the theory for modeling surface systems, in this chapter, the terminal group substitution allowing for a modification of interfacial properties of the metal−organic molecule interface that crucially determines the performance of molecular electronic devices will be examined in a theoretical and quantitative way.

3.1 Introduction and Motivation

Chemisorption of SAMs on metal substrate is an efficient strategy to introduce new functionality of organic thin films [1, 2], and the appropriate choice of the terminal functional groups of the well-defined SAMs gives an opportunity to tune the nature of chemical bonding and conformation at the electrode surface. Small differences exert large effects on the tunneling charge transfer, yet it is this sensitivity that drives scientific interest because functionality arises from precise control over conformation and geometry. By varying the SAMs adsorbates substituted with functional groups which have different electron donating or withdrawing ability, change of electron localization towards the contacting head group can be realized. However, the magnitude of such terminal group substitution induced change of bonding nature is not easily to be evaluated in a quantitative way.

The resonant frequency based vibrational spectroscopy is one of the most widely used techniques for identifying the bonding information, and a frequency shift for the adsorbed molecule on the surface can be used as an indicator of the strength of chemical bonding on surface. In previous study, Uosaki *et al*. have examined the vibrational behavior of aryl isocyanide molecules adsorbed on the metal surface by the vibrational sum frequency generation (VSFG) spectroscopy [3]. Effects of the *para*-substituted group of aryl isocyanide molecule and metal substrates on VSFG spectra have been investigated. For identifying the bonding nature between NC head group and the substrate atoms, the tilt angles of 4-methylphenyl isocyanide (MPI) were estimated from the intensity ratio between VSFG peaks of C−H symmetric and asymmetric stretching vibrational modes of CH_3 group. However, the exact electron transfer mechanism and means of controlling the chemical bonding formation at the interfacial region of SAMs/metal surface are still unclear.

The use of theoretical indicators to characterize the reactive properties of surfaces is a common topic in the surface science community, various such indicators have been used to quantitatively examine the electron transfer between the molecule and surface. Hu *et al*. carried out the overlap population analysis of the molecular orbitals (MOs) to evaluate the magnitude of interaction strength between 4-chlorophenyl isocyanide molecule and Pt(111) or Au(111) surface. The relationship between the vibrational spectra and the electronic structure quantitatively has also been revealed [4]. In addition, two topological methods, namely Bader's quantum theory of atoms-in-molecule (QTAIM) [5−8] and electron localization function (ELF) [9, 10], are widely accepted as the modern theoretical methods for studying the nature of chemical bonding interactions. Specifically, QTAIM connects the topology of the electron density of a system based on the viewpoints of atoms and chemical bonding, while the ELF tool provides the explicit information

on the different bonding types, including covalent, ionic, and metallic bonds. In comparison to the mentioned methods, the natural bond orbital (NBO) analysis has also been broadly used to decipher the chemical bonding picture and interpret the electronic structures of the molecules due to the close association with the conventional Lewis structure diagrams [11]. Based on the density matrix, bonding orbitals, antibonding orbitals, lone pair orbitals, as well as Rydberg orbitals can be constructed as the linear combinations of orthogonal hybrid orbitals centered on atoms within the target molecule. At present, NBO algorithm has been broadly used for the isolated molecular cases, but recently it has been extended to the periodic system by Dinnington and Schmidt [12]. The developed periodic implemented NBO theory has been employed to solve various issues, such as the CO adsorption site preference problem [13], geometric changes upon the removal of a single oxygen atom from MgO surface [14], and the reaction mechanism of catalytic oxidation of NO by Cr_2O_3 surface [15].

In this chapter, we employ a NBO bond order model which can be derived from the periodic implementation of NBO analysis to examine the substituent effect on the bonding nature for aryl isocyanide molecules adsorbed on the Pt(111) surface. Vibrational frequencies were also calculated to get insight into the NC chemical bond strength and in conjunction with the experimental observations.

3.2 Computational Details

3.2.1 general parameters and computational models

Our calculations employ DFT techniques to simulate the whole system (organic layer and the metal surface). The DFT calculations were carried out for aryl isocyanide molecules X−C_6H_4−NC (X = $N(CH_3)_2$, NH_2, OCH_3, CH_3, H, Cl, CF_3, CN, NO_2) as isolated molecules and also adsorbed on the Pt(111) surface. The calculation were performed in the framework of generalized Kohn-Sham scheme using the projector augmented-wave (PAW) method [16, 17] as implemented in the Vienna Ab-Initio Simulation Package (VASP) package [18−21]. The calculation employed the Perdew-Burke-Ernzerhof (PBE) exchange-correlation functionals [22, 23] and account for the dispersion interactions using DFT-D3 method [24−26]. The specific parameters of DFT-D3 were directly taken from the implementation of dispersion effect in DFT calculations. For the treatment of valence electrons, we treated the valence s and d electrons and semicore p electrons as valence electrons for Pt atom. The convergence criteria for the total energy during the calculation was set to 10^{-5} eV. All geometries were fully optimized until the maximum final force less than 0.025 eV/Å using the conjugate-gradient (CG) algorithm. Γ-centered 9 × 9 × 1 meshes of the **k** grid was generated according to the Monkhorst-Pack scheme [27], and was used for the Brillouin zone (BZ) sampling. A plane wave cutoff energy was set to 600 eV. For isolated molecule, only the Γ point (1 × 1 × 1) was employed.

The lattice parameter of the bulk metal was calculated by fitting to the second-order Birch-Murnaghan equation of state [28]. The calculated lattice parameter is 3.9197 Å, which is in good agreement with the experimentally determined 3.9242 Å [29]. The Pt(111) surface was simulated with a 2 × 2 super cell and four-layered repeated slabs. A vacuum thickness with above 14 Å was set to sufficiently eliminate the periodic image interactions between neighboring cells. For the

clean Pt(111) surface, only top two layers were allowed to relax. X−C_6H_4−NC molecule was placed at the top site of one Pt atom once the calculation convergence was reached. The C atom of molecule was directly positioned above one Pt atom, and the N−C bond was placed perpendicular to the Pt surface, as shown in **Figure 3.1**. The oriented configuration is consistent with the experimentally observed atop adsorption site [3]. Finally, atoms in the bottom two layers were fixed at their bulk state while the adsorbed X−C_6H_4−NC molecule and the top two layers of the Pt surface were fully optimized. The spin polarization was applied to all calculations.

To calculate the vibrational frequency, we used a finite difference approach with a displacement of 0.015 Å. To reduce the computational cost, only the directly adsorbed Pt atom and all atoms of the X−C_6H_4−NC molecule were included. According to the periodic NBO algorithm, the electronic wave function represented in the atom-centered basis set is necessary. To reach this target, the plane wave function derived from plane wave DFT calculation was projected onto the Gaussian-type basis functions taken from the EMSL basis set library [30, 31]. In this study, the triple-ζ 6-311G* basis set was utilized for C, H, N, O, F atoms [32], and Cl atoms [33], while the jorge-DZP basis set was used for Pt atom [34]. Visualization of the structures, electron density and the NBO results were accompanied with the help of Visualization for Electronic and Structural Analysis (VESTA) code [35].

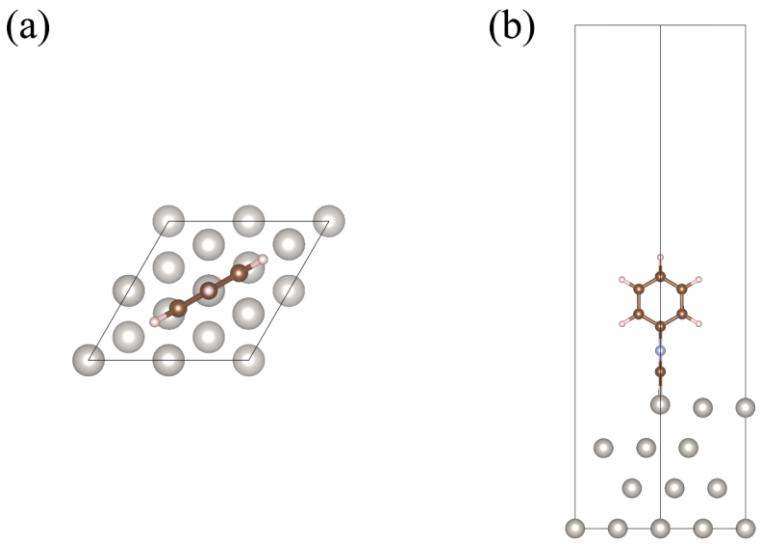

Figure 3.1. Top and side view of isocyanide SAMs adsorbed on Pt(111) surface, using H−C_6H_4−NC adsorbed on Pt(111) surface as the model.

To assess the effect of each substituent on the aryl isocyanide adsorbate and to quantitatively vary the electron donating or withdrawing ability of the substituents, we include the Hammett constants [36, 37] into this study. **Table 3.1** lists the overall studied substituents, their corresponding *para*-substituted Hammett constant (σ_p) relative to the hydrogen has also been given.

−X	σ_p	−X	σ_p
$-N(CH_3)_2$	−0.83	−Cl	0.23
$-NH_2$	−0.66	$-CF_3$	0.54
$-OCH_3$	−0.27	−CN	0.66
$-CH_3$	−0.17	$-NO_2$	0.78
−H	0		

Table 3.1. The studied substituents that set para to the aromatic ring in the aryl isocyanide molecules along with the corresponding Hammett constant (σ_p) for each substituent

The conventional Hammett constant or parameter is determined according to the **Figure 3.2**. The Hammett constant is obtained from placing the substituent (X) to the carboxylic acid functional group, and measuring the differences in reaction rate of the benzoic acid dissociation constant in water solution. Varying the electron richness or poorness of the benzylic carbon, the reactivity differences can thereby be interpreted. Thus, Hammett constant has widely used as a semiquantitative evaluation the charge build-up at the benzylic carbon in the reaction transition state. In this study, the *para*-substituted constants is defined as σ_p, the electron-donating groups (EDG) possess negative σ_p values, whereas the electron-withdrawing groups (EWG) shows positive σ_p values. X = H is treated as a reference as $\sigma_p = 0$.

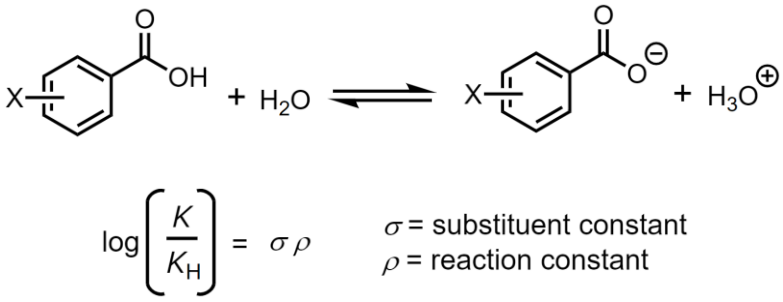

Figure 3.2. A benzoic acid ionization reaction with water [38].

3.2.2 periodic NBO algorithm derived bond order model

To describe the NC bond strength, we introduced a simple bond order model based on the orbital occupancy of the target surface model obtained from the periodic NBO analysis. The NBO bond order of the NC bond can be simply calculated as:

$$(n_{BO} - n_{ABO}) / 2$$

where n_{BO} and n_{ABO} represent the number of electrons in bonding orbitals and antibonding orbitals, respectively. According to this bond order model, it is evident that the bond order has the largest value when the bonding states are fully occupied, and antibonding states remain in empty.

The bond order is not an observable value, but rather an indicator for better understanding of chemical bonding strength in the framework of electronic wavefunction of the system. In addition, bond strength can also be determined by the stretching frequency of a chemical bond: a stronger bond relates to a larger frequency, and vice versa.

In addition to the periodic NBO analysis, the electron localization functions (ELF) which can provide an additional measure of the electron density at the chemical bond were also computed on the basis of periodic-boundary-condition DFT as implemented in VASP software.

3.3 Result and discussion

3.3.1 isolated X−C_6H_4−NC molecule

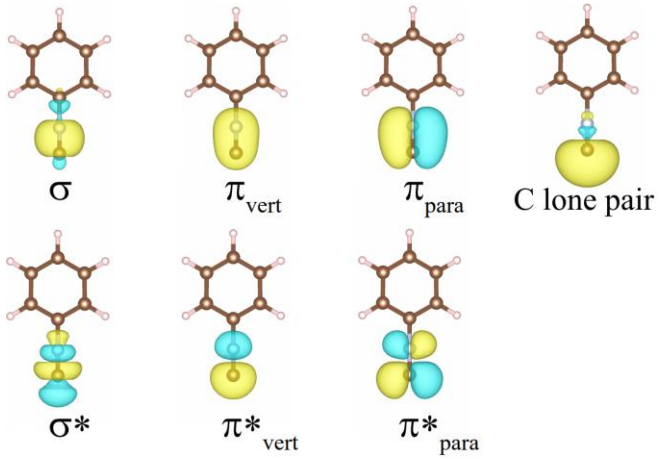

Figure 3.3. The NBOs to represent the NC bonding nature in isolated aryl isocyanide molecule of H−C_6H_4−NC: σ bonding orbital, vertical component of π bonding orbital (π_{vert}), parallel component of the π bonding orbital (π_{para}), C lone pair orbital, and the corresponding three antibonding orbitals (σ*, π^*_{vert}, π^*_{para}). Isosurface is set to 0.04 e/Bohr^3.

Figure 3.3 shows some NBOs that are related to the NC bonding of an isolated H−C_6H_4−NC molecule. The triple bond nature of the NC bond is constituted by one σ and doubly degenerate π bonding orbitals. If we consider the planarity of the benzene ring, the NC π orbitals can be classified into the vertical component (out-of-plane, π_{vert}), and the parallel component (in-plane, π_{para}). The C lone pair orbital with doubly-occupation has also been shown in Fig. 3.3. It should be noted that the C lone pair orbital has a slight antibonding character between the C and N atoms.

Figure 3.4 shows the computed results of (a) NC stretching frequency, (b) bond order, (c) bonding orbital population, and (d) antibonding orbital population for all isolated molecules as a function of Hammett constants. We found both NC stretching frequency and bond order have the

same "volcano-like" profiles: their trends increase from the most EDG to H group, and then tend to decrease from H group to the most EWG.

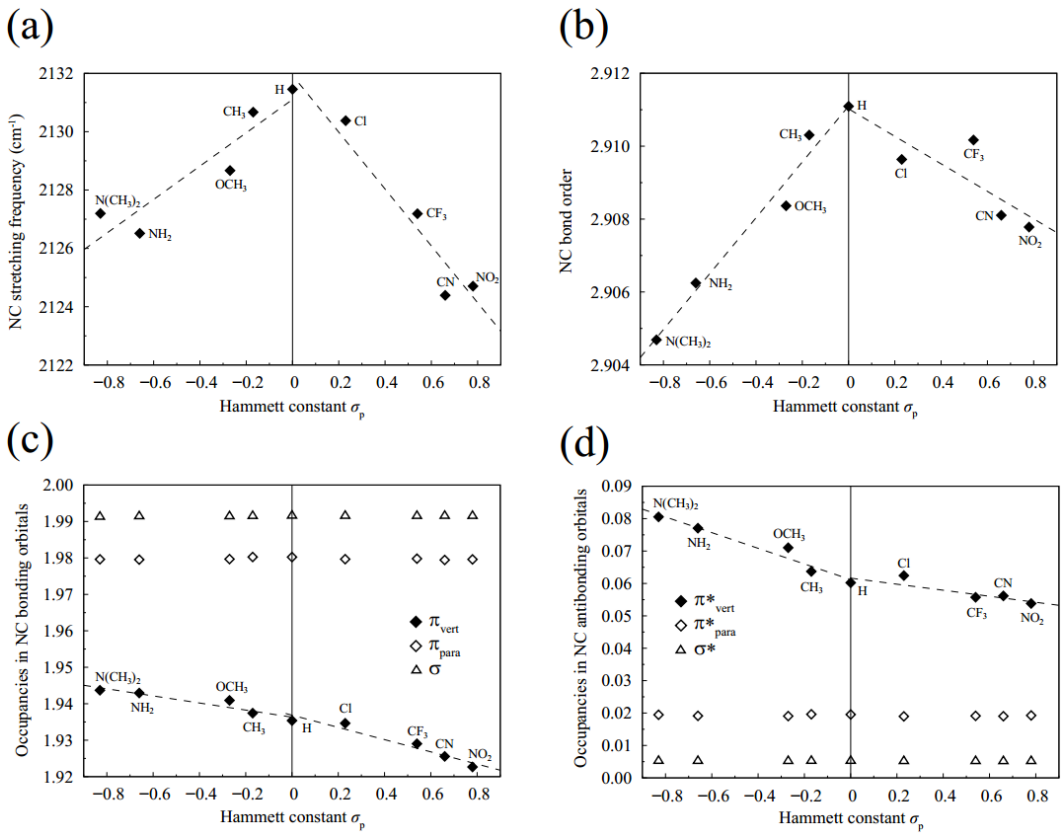

Figure 3.4. (a) NC stretching frequency, (b) NC bond order, (c) NBO occupancy in NC bonding orbitals (σ and π), and (d) NBO occupancy in NC antibonding orbitals (σ* and π*) for isolated X−C_6H_4−NC molecule. *x* coordinate shows the para-substituted Hammett constants of each group.

The electron transfer between the *para*-substituted groups and NC group of the isolated aryl isocyanide (X−C_6H_4−NC) molecules is responsible for variations in bond order. The EDG attached to the benzene can increase the electron denstity in benzene ring by the resonance effect. This will result in more electron transfer transferred into the antibonding orbital of NC group. On the other hand, the EWG attached to the benzene tends to attract electron from the benzene ring. This effect will result in the slight removal of electron from the bonding orbitals of NC group. To

give a more detailed analysis, we then classifiled the NC bond into σ, π_{vert}, and π_{para} orbitals, respectively, and calculated their NBO occupancies, as shown in Fig. 3.4(c) and (d). We found the NBO occupancy in σ and π_{para} bonding orbitals are roughly constant with respect to the Hammett constant. In contrast, NBO occupancy in π_{vert} bonding orbital are significantly influenced, the detailed values decrease from 1.94 (for $N(CH_3)_2$) to 1.92 (for NO_2). A substantial decrease trend is observed in the π_{vert} bonding orbital population with the increase of electron withdrawing ability. Therefore, the electron transfer to substituents is mainly arising from the loss of electron in π_{vert} bonding orbital. On the other hand, electron transfer from the substituents to NC group can be quantitatively determined from the occupancy change in three corresponding antibonding orbitals, σ *, π^*_{para} and π^*_{vert}, as shown in Fig. 3.4(d). Also, we found that NBO occupancy in σ * and π^*_{para} antibonding orbitals keep almost invariant with respect to the Hammett constants, there is very limited electron transferred into these orbitals. In contrast, we observed the decrease trend in π^*_{vert} antibonding orbital; substituted-groups with more electron donating ability promote more electrons into the π^*_{vert} orbitals, suggesting that the π^*_{vert} orbitals are more sensitive to the change of electron withdrawing/donating ability.

The above results reveals that the bond order variation is primarily arising from the occupancy change in the π_{vert} component. The total bond order trend follows the mode of π_{vert} and π_{vert}* occupancies. More specifically, we found the decrease trend in NBO occupancy of π_{vert} and π^*_{vert} orbitals are different with each other. For π_{vert} bonding orbital, the plotted line in EDG region shows a gentle slope compared to the plotted line in the EWG zone. Contrarily, we found the completely opposite decrease trend for π^*_{vert} antibonding orbital. As a consequence, the total "volcano-like" trend of the bond order can be invoked by this difference.

The "volcano-like" trend of the bond order can be intuitively and qualitatively explained by thinking over a picture that EDGs give more electrons to antibonding orbitals of NC group, while EWGs attract more electrons from the bonding orbitals of NC through the aromatic ring. Both of these two ways result in a decrease trend of bond order, therefore, a molecule with no substitution ($H-C_6H_4-NC$ molecule) exhibits the highest bond order. Finally, the local populations are also affected by substituted group. When electron-withdrawing ability of a group increases, the C atom gets more positively charged, while the N atom becomes more negative charged. This also confirms that it is the electron-withdrawing ability of substituent that causes the electron transfer from C to N, aromatic ring, and also the substituted group.

3.3.2 $X-C_6H_4-NC$ molecule on Pt(111) surface

Next step, we turn our attention to $X-C_6H_4-NC$ molecules adsorbed on the Pt(111) surface. We have recognized that predicting the accurate adsorption site on surface remains a very challenging subject for conventional DFT calculation when we talk about the adsorption of CO molecule on transition metal surface [39−43]. Actually, our calculated results in the framework of PBE functional shows that the $X-C_6H_4-NC$ molecule adsorbs at the hollow site on the Pt surface, while the experimental characterization indicates that atop site is the accurate adsorption site. To follow the experimental reported result strictly, the CN bond was oriented perpendicular to Pt surface in our subsequent calculations.

Table 3.2. Bond lengths of CN of X−C_6H_4−NC molecules adsorbed on Pt(111) surface and their corresponding adsorption energies.

	Hammett constant	NC bond length (Å)	Adsorption energy, E_{ads} (eV)
$-N(CH_3)_2$	−0.83	1.1827	−2.4315
$-NH_2$	−0.66	1.1829	−2.4281
$-OCH_3$	−0.27	1.1833	−2.5042
$-CH_3$	−0.17	1.1831	−2.4590
−H	0	1.1837	−2.4277
−Cl	0.23	1.1840	−2.4621
$-CF_3$	0.54	1.1849	−2.4693
−CN	0.66	1.1855	−2.3526
$-NO_2$	0.78	1.1851	−2.3758

Table 2 lists the bond lengths of CN bond of aryl isocyanide molecules adsorbed on Pt(111) surface and their corresponding adsorption energies which can be defined as

$$E_{ads} = E[\text{molecule-surface}] - (E[\text{molecule}] + E[\text{surface}])$$

herein, $E[A]$ shows the calculated electronic free energy of species A. Bond length of the CN bond increases with the increase of the electron withdrawing ability quantified by Hammett constants. On the other hand, their adsorption energies show a slight fluctuation ranging from −2.35 to −2.50 eV, indicating a strong chemical adsorption.

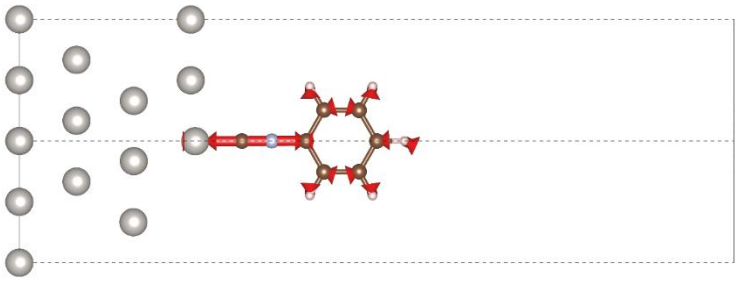

Figure 3.5. Stretching vibration of the NC bond of aryl isocyanide SAMs adsorbed on Pt(111) surface. The red arrows show the direction of vibrations and their length indicates the associated stretching strength.

Figure 3.5 shows the NC stretching vibration when X−C_6H_4−NC molecules adsorbed on the Pt(111) surface. **Figure 3.6** shows the variation of stretching frequency and bond order of NC bond of the X−C_6H_4−NC molecules (where X = $N(CH_3)_2$, NH_2, OCH_3, CH_3, H, Cl, CF_3, CN, NO_2, respectively) on the Pt(111) surface (in red color), as a function of the electron donating/withdrawing ability. To give a better comparison, we added the reported results of isolated molecules (shown in Fig. 3.4) to the Fig. 3.6 (in black color). As shown in the Fig. 3.6(a), including the surface substrate increases the stretching frequency of NC bond by approximately 70 cm^{-1} (blue-shifted) when comparing with the respective isolated molecules. This phenomenon is consistent with the experimental results by VSFG spectroscopy [3]. The calculated and experimental results reveal that electron transfer between adsorbate and surface can influence the stretching frequency of NC bond greatly. In particular, stretching frequency of NC bond after adsorption on surface exhibits a decrease trend from the most EDG to most EWG. This trend is different from the isolated case which shows a "volcano-like" trend.

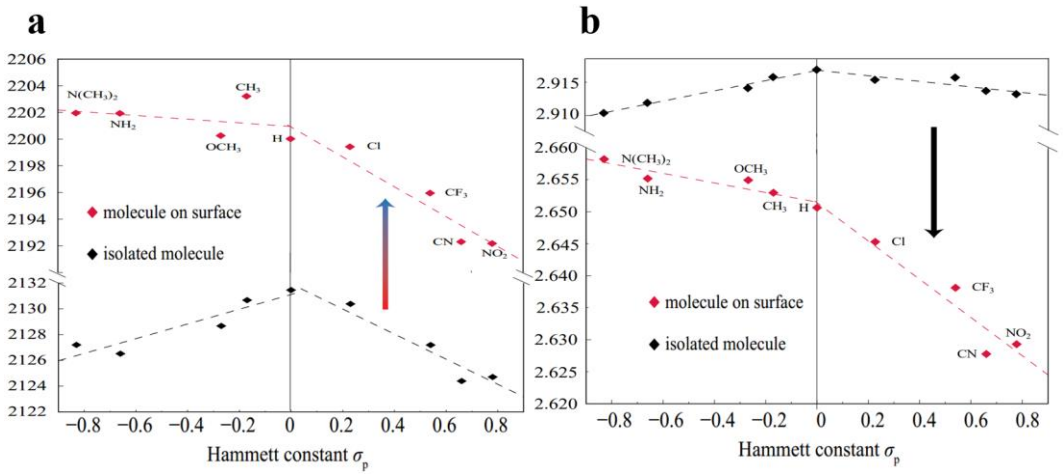

Figure 3.6. (a) Stretching frequency and (b) bond order of the NC bond of X−C_6H_4−NC molecules adsorbed on Pt(111) surface (in red color) and the isolated case (in black color), as a function of Hammett constant. The dashed lines represent the linear fits of each region and the y coordinate has been partially omitted for a better comparison.

Comparison of the bond order of NC bond of isolated and adsorbed aryl isocyanide SAMs have been depicted in the Fig. 3.6b. After adsorption, bond order of NC bond derived from our NBO model decreases (↓ 0.28) although the stretching frequency has experienced a large blue shift (~70 cm^{-1}). Thus, the larger bond order does not always relate to the higher frequency of the corresponding stretching vibrational mode using this periodic NBO algorithm derived bond order model. Bond orders of adsorbed molecules have a decrease trend, which is different from the isolated case. The electron transfer from the Pt surface to antibonding orbitals of NC bond contributes to this decrease trend of bond order. A larger occupancy increase in the antibonding orbitals of NC bond and a relatively smaller occupancy loss in the bonding orbital result in the overall observed trend.

To get insight into the origin of the similar trends in stretching frequency and bond order of NC bond, we then concentrate on the factors that can directly affect the chemical bonding mechanism and investigate the explicit electron transfer mechanism during the generation of a chemical bond between aryl isocyanide SAMs and Pt(111) surface. This electron transfer process can introduce a change in spectroscopic information of X−C_6H_4−NC on metal surfaces [3, 4, 44−46]. The generally accepted Blyholder model that consists of σ donation and π back-donation have been broadly used to examine the bonding interaction between CO molecule and Pt(111) surface [13, 47−49]. Validity of Blyholder-type representation has also been confirmed when applying to other models, such as HNC molecule on Au(111) surface [50], and Cl−C_6H_4−NC molecule on Au(111) and Pt(111) surfaces [4], Cl−C_6H_4−NC molecule on Pt(110), Pt(211), Pt(100), and Pt(111) surfaces [44]. In this study, we also employ such representation in which the strength of NC bond of aryl isocyanide SAMs on the Pt(111) surface is determined by a balance between σ donation (from lone pair orbital of C atom to partially occupied d orbitals of Pt surface) and π back-donation (from Pt d orbitals to π* antibonding orbitals of NC bond), as shown in the schematic illustration below (**Figure 3.7**). It is worth to mention that the mixing states between MOs of molecule and the d orbitals of metal are outside the regime of the conventional Blyholder model. Such mixing states have been included in an advanced representation, namely Pettersson-Nilsson model [51−55]. Additional MOs have been considered in this model and the interaction between molecule and metal surfaces have been described by σ-repulsion/π-attraction mechanism. This model thereby essentially extends the simple representation of the Blyholder model. Furthermore, the extended σ-repulsion/π-attraction mechanism pointed out that σ interaction has both repulsive and attractive components through the Pauli repulsion and electron donation to metal bands, respectively. This newly proposed model has been applied to investigate the C−O

and C−metal bond strengths of CO molecule adsorbed on Pt−Ru−Os tertiary alloy and Pt−Os binary alloy and [56], PtRuOsIr quaternary [57], PtRu alloys [58], and Pt(100) and Ru(0001) surfaces [59], as well as CO and H_2O co-adsorbed on Pt(111) surface at different coverages [60]. To concisely investigate the substituent effect on stretching frequency and bond order of NC bond, we characterize the donation and back-donation strengths according to a localized perspective of chemical bonding in a quantitative manner.

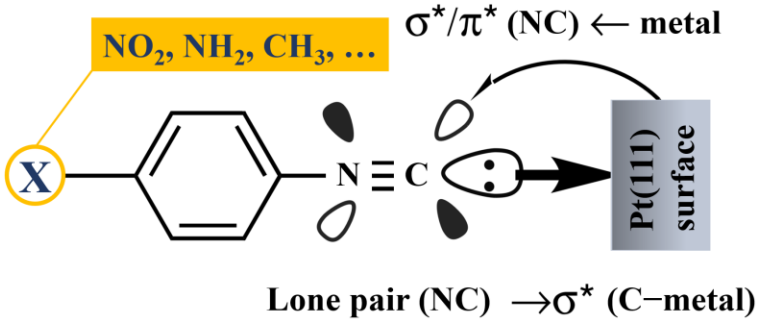

Figure 3.7. A schematic illustration of the donation and back-donation processes between aryl isocyanide molecule and the metal surface (Pt(111) surface in this chapter). X represents the *para*-substituted groups.

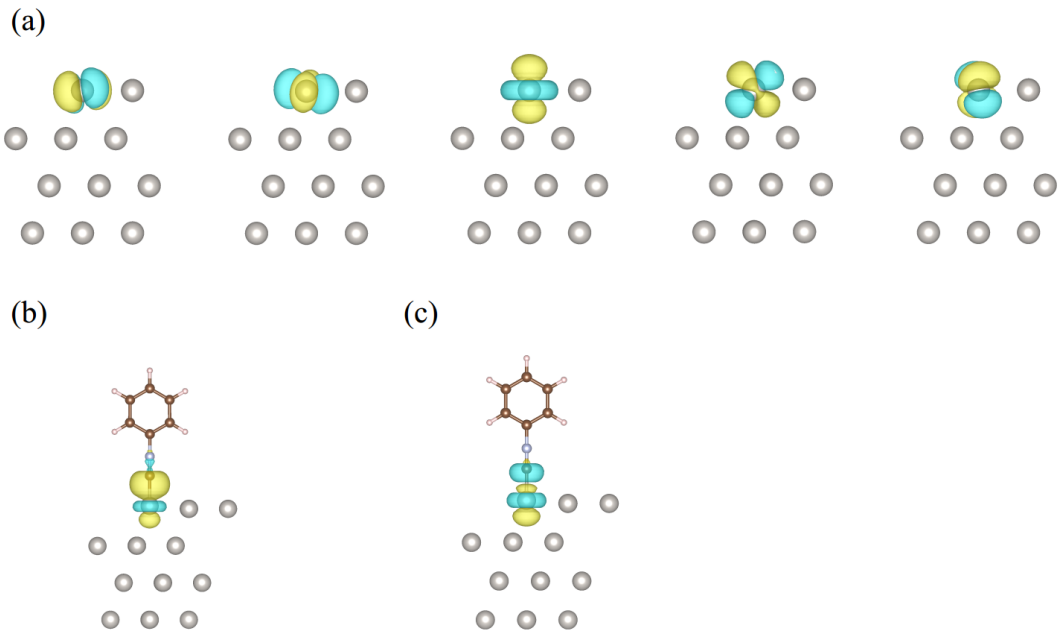

Figure 3.8. (a) five d orbitals of the metal atom in the clean Pt(111) surface, (b) Pt−C σ bonding orbital, and (c) Pt−C σ* antibonding orbital.

Figure 3.8 shows the periodic NBO algorithm derived five d orbitals of the Pt atom in the clean Pt surface, the Pt−C σ bonding orbital, and its corresponding antibonding orbital. The H−C_6H_4−NC molecule adsorbed on the Pt(111) surface has been used as the model case. C lone pair orbital of H−C_6H_4−NC in Fig. 3.3 and the Pt d_z^2 orbital contribute to the formation of Pt−C σ bonding and σ* antibonding orbitals. After adsorption, lone pair orbital of C interacts with the partially occupied Pt d_z^2 orbital, electrons transfer from the aryl isocyanide SAMs to the adsorbed Pt atom where σ bonding and σ* antibonding orbitals of Pt−C bond are locating around the Fermi level. It is well known that the LUMO of adsorbate should locate near to the Fermi level of the metal surface for an efficient electron injection from metal to adsorbed molecule. We observed an almost doubly-occupied Pt−C σ bonding orbital with an occupation of above 1.95 electrons, which is consistent with the picture of a localized two-center bond. The further population analysis also supports the view of this strong ionic character of Pt−C bond. The natural charge of C atom of NC

bond in H−C_6H_4−NC molecule case varies from +0.23 *e* (for isolated molecule) to +0.45 *e* (on surface). This is attributed to the removal of electron from C lone pair to form Pt−C bonding orbital, The charge of N atom changes slightly from −0.46 *e* (for isolated molecule) to −0.36 *e* (on surface). On the other hand, charge of the adsorbing platinum atom is −0.45 *e*, which is much negative than its neighboring Pt atoms on the top layer (approximately +0.16 *e*).

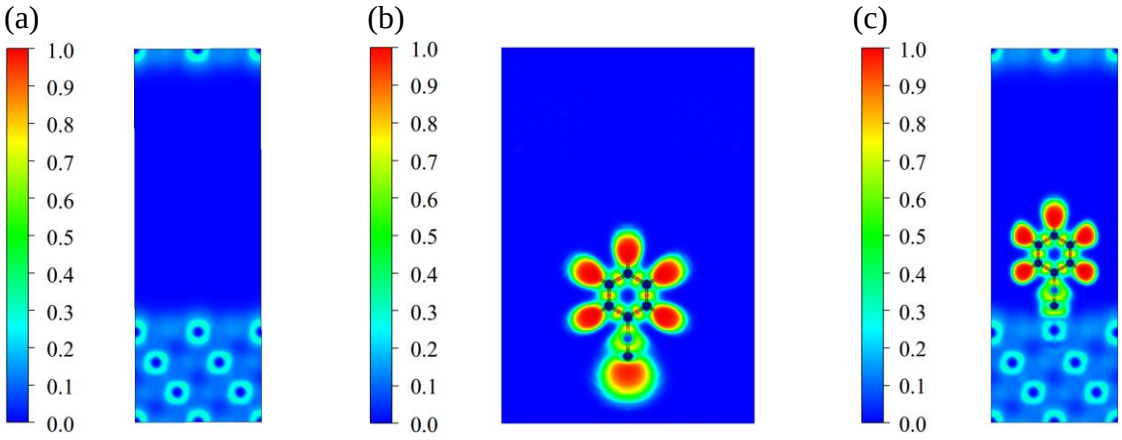

Figure 3.9. Electron localization function (ELF) plots of (a) clean Pt(111) surface, (b) isolated H−C_6H_4−NC molecule, and (c) H−C_6H_4−NC molecule adsorbed on Pt(111) surface. In the color-coding scheme, a high degree of electron localization is shown in red color, whereas regions of low ELF values are shown in blue color. The isosurface values of the maps are set to 0.04 e/Bohr^3.

An additional measure of the electron density rearrangement has been performed by the electron localization function method, as shown in **Figure 3.9**. The maximum of electron localization near the Pt atoms is 0.332, such low ELF value reveals the metallic nature of the Pt(111) surface. For isolated H−C_6H_4−NC molecule, we found the high ELF value (> 0.9) around the region of C atom of NC group, suggesting the complete localization characteristic of the C lone

pair orbital. The ELF value between N and C atoms is approximately 0.75, showing a typical covalent bonding interaction. After adsorption on Pt(111) surface, we observed a large difference in the ELF between C and Pt atoms. Such large difference has been considered as a signature of the ionic character of Pt−C bond.

Let us now quantify the interactions taking place between the molecule and the metal substrate in terms of charge transfer upon adsorption. As shown previously in Fig. 3.6, the stretching frequency of NC bond of aryl isocyanide SAMs show a large blue shift by ~70 cm^{-1} after adsorption when comparing with frequencies for corresponding isolated molecule. Such blue-shift phenomenon can be explained by σ donation from C lone pair orbital of the adsorbate to the metal surface since the C lone pair orbital shows a partial antibonding character for NC bond, as shown in the Fig. 3.3. Formation of the Pt−C σ bond via the σ donation promotes the suppression of this antibonding character, resulting in the strengthening of NC bond and thereby a blue-shift in the vibrational frequency [61]. We have also recognized that the magnitude of blue shift decreases gradually as the Hammett constant increases. NBO occupancies in Pt−C σ bonding orbital and σ* antibonding orbital have been shown in **Figure 3.10**, as a function of the Hammett constant. We found the NBO occupancy in Pt−C σ bonding orbital remains constant with respect to the Hammett constant. In contrast, we found an evident linearly increase trend for NBO occupancies in Pt−C σ* antibonding orbitals. The substituent effect on σ donation bond appears mainly in the variation of the occupancy in Pt−C σ* antibonding orbitals. The increasing trend in Pt−C σ* occupancy suggests the increase of the NC antibonding character induced by C lone pair orbital, which is consistent with the decrease trend of the magnitude of blue-shift in frequency as the Hammett constant gradually increases.

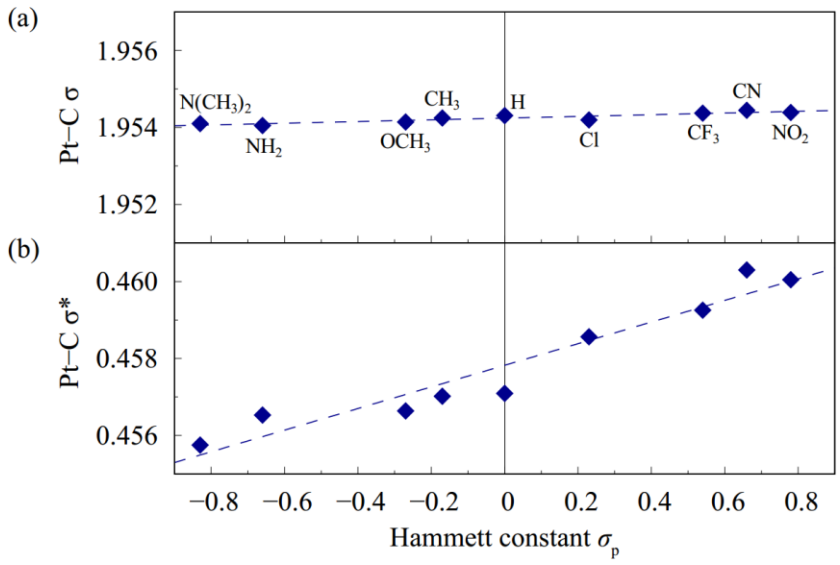

Figure 3.10. Periodic NBO algorithm derived occupancies in (a) Pt−C σ bonding orbital and (b) Pt−C σ* antibonding orbital of X−C_6H_4−NC molecule with different substituents adsorbed on the Pt surface, as a function of the Hammett constant of each group.

In addition to the main interaction between C lone pair orbital of the NC bond and Pt d orbitals, the σ and two π bonding orbitals of NC bond can also interact with the d orbitals of Pt atom in the surface. Both of them show the less occupancy after adsorption on surface (the decrease amount is only around 0.02~0.03). In particular, the decrease amount of NBO occupancy of π_{vert} also shows a decrease trend as a function of the *para*-substituted Hammett constant. This is attributed to the electron donating/withdrawing ability of the substituted groups. In comparison to the Pt−C σ bond, NBO occupancies of NC σ and π orbitals is not significantly affected with respect to the Hammett constant. Therefore, we can conclude that the C lone pair orbital of the isolated X−C_6H_4−NC molecule plays a dominant role during the formation of Pt−C bond.

As for the π back-donation that indicates the electron transfer from metal surface to the adsorbed molecule, the π* antibonding of NC bond accepts electron from Pt d-states. One of the

typical phenomena towards the σ donation/π back-donation model is the partially filling of π* antibonding orbitals upon adsorption on surface. The metal−adsorbate interaction can be destabilized with an increase of filling in the antibonding orbital, leading to a weaker binding. π back-donation reduces the bond strength of NC bond, and therefore, causing a red shift in the stretching frequency of NC bond. Such effect is opposite to the effect of σ donation. Here, we use the difference of orbital occupancy in π* antibonding orbitals of NC between adsorbed and isolated X−C_6H_4−NC molecules to define the NBO occupancy increment. **Figure 3.11** shows the NBO occupancy increment for NC π* antibonding orbitals between adsorbed and isolated molecules for (a) vertical component (π^*_{vert}), and (b) parallel component (π^*_{para}). We found a 0.20~0.30 occupancy increment in each component equally. Such large antibonding occupancy increment reveals that the electron transfer from the metal surface to the adsorbed molecule has occurred. Specifically, filling of the π* NC orbital can be facilitated when using substituted groups with greater electron withdrawing ability for adsorption. In contrast, filling of the NC π* orbital can be hindered by the substituted groups with stronger electron donating ability. The bond order of NC bond becomes lower when more electrons transferred into the NC π* orbital. Therefore, according to our definition of the NBO derived bond order model, the bond order behaves as an overall decrease trend, which has shown in the Fig. 3.6. On the other hand, we can conclude that as the electron withdrawing ability of the substituted group increases, the π back-donation becomes stronger.

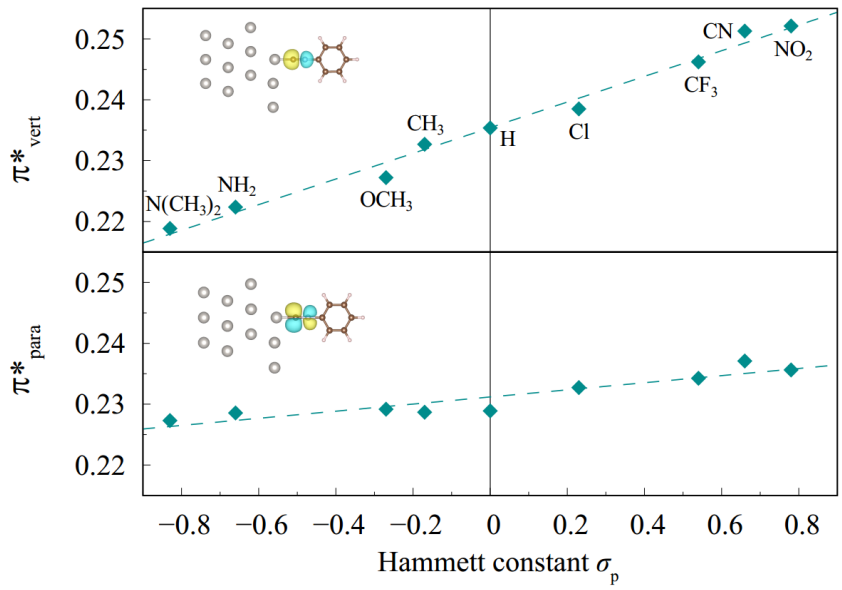

Figure 3.11. The NBO occupancy difference in orbital occupancy between the NC π* antibonding orbitals of isolated and adsorbed aryl isocyanide SAMs, (a) vertical component (π^*_{vert}), and (b) parallel component (π^*_{para}). The insets give the schematic configurations of these two NC π* antibonding orbitals for electron injection upon adsorption on metal surface.

The occupancy change upon adsorption on surface also occurs in the σ* antibonding orbital. In comparison to the π* orbitals, the occupancy difference in the σ* orbital is very limited (~0.009 *e*). However, we also found a linearly increase trend with respect to the Hammett constant. This trend is also due to the increase of electron withdrawing ability of the substituted groups.

The donor/acceptor analysis proposed by Dinnington and Schmidt [10] confirms the source of the occupancy increase in these antibonding orbital is from the metal lone pairs. After adsorption, we found that the configurations of d states of the adsorbing Pt atom have slightly changed with respect to the original coordinate plane. We think this is mainly due to the appearance of the π-conjugated benzene plane. Due to symmetry consideration, the deformed d_{xz} and d_{yz} orbitals on the adsorbing Pt atom have been shown in **Figure 3.12**. The two d orbitals of the adsorbing Pt atom

that have similar symmetry as the π orbitals of the adsorbed SAMs. This gives a visible representation of the concept of metal back bonding [62].

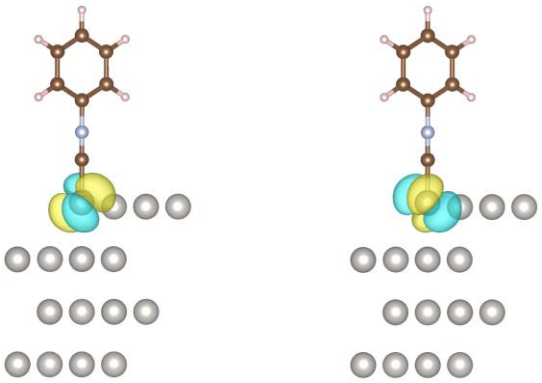

Figure 3.12. The deformed d_{xz} and d_{yz} orbitals on the adsorbing Pt atom.

In light of these calculated results, we conclude that both σ donation and π back-donation are responsible for the change of the stretching frequency of NC bond. Specifically, the blue shift in the frequency is mainly due to the σ donation, while the red shift is induced by the π back-donation. The resultant effect of donation and back-donation determines the overall decrease trend in frequency. On the other hand, the definition of periodic NBO algorithm derived bond order model proposed here shows the more significant role of NC antibonding orbitals. It can be thereby understood that the bond order in the case of aryl isocyanide SAMs on Pt(111) surface is primarily attributed to the strength of π back-donation. This can help us to explain the substantial decrease of the bond order.

3.4 Summary of This Chapter

This chapter provides an atomic view of the electronics states involved in the formation of the chemical bond in SAMs/metal surface interface with different substituent groups, which provide different degrees of electron donation and back-donation and are essential toward the design of molecular electronic devices with chemical functionality. The charge density rearrangements confined to the interface caused by chemical bonding interaction between aryl isocyanide molecules and the Pt(111) surface can be easily captured by periodic NBO implementation. Through a comprehensive DFT study on a series of substituent attached SAMs, relationships between the bonding structure and the electron donating or withdrawing ability of substituent are described explicitly. Moreover, this chapter also started with the strong curiosity about the applicability of the theoretical modeling and also the correspondence between experimental and theoretical results.

3.5 References

[1] G. Whitesides, *Science* **295**, 2418 (2002).

[2] G. Bracco; M, Smerieri; L. Savio, Self-assembly of Organic Molecules at Metal Surfaces. Springer Handbook of Surface Science 2020, 967−1004.

[3] M. Ito, H. Noguchi, K. Ikeda and K. Uosaki, *Phys. Chem. Chem. Phys.* **12**, 3156 (2010).

[4] W. Hu, S. Duan, Y. Zhang, H. Ren, J. Jiang and Y. Luo, *Phys. Chem. Chem. Phys.* **19**, 32389 (2017).

[5] R. F. W. Bader, *Chem. Rev.* **91**, 893 (1991).

[6] R. F. W. Bader, *Atoms in Molecules: A Quantum Theory*, Oxford University Press, USA, 1994.

[7] R. F. W. Bader, *Acc. Chem. Res.* **18**, 9 (1985).

[8] R. F. W. Bader. In: P. v. Schleyer, (Ed.). *Encyclopedia of Computational Chemistry.* (John Wiley and Sons, Chichester, U.K., 1998), pp. 64−86.

[9] A. D. Becke and K. E. Edgecombe, *J. Chem. Phys.* **92**, 5397 (1990).

[10] A. Savin, R. Nesper, S. Wengert and T. F. Fässler, A*ngew. Chem., Int. Ed. Engl.* **36**, 1808 (1997).

[11] F. Weinhold and C. Landis, *Valency and Bonding–A Natural Bond Orbital Donor-Acceptor Perspective*; Cambridge University Press: Cambridge, 2005; pp 1−44.

[12] B. D. Dunnington and J. R. Schmidt, *J. Chem. Theory Comput.* **8**, 1902 (2012).

[13] G. T. K. K. Gunasooriya and M. Saeys, *ACS Catal.* **8**, 3770 (2018).

[14] I. A. Popov, E. Jimenez-Izal, A. N. Alexandrova and A. I. Boldyrev, *J. Phys. Chem. C* **122**, 11933 (2018).

[15] J. Jin, N. Sun, W. Hu, H. Yuan, H. F. Wang and P. Hu, *ACS Catal.* **8**, 5415 (2018).

[16] P. E. Blöchl, *Phys. Rev. B* **50**, 17953 (1994).

[17] G. Kresse and D. Joubert, *Phys. Rev. B* **59**, 1758 (1999).

[18] G. Kresse and J. Hafner, *Phys. Rev. B* **47**, 558 (1993).

[19] G. Kresse and J. Hafner, *Phys. Rev. B* **49**, 14251 (1994).

[20] G. Kresse and J. Furthmüller, *Phys. Rev. B* **54**, 11169 (1996).

[21] G. Kresse and J. Furthmüller, *Comput. Mater. Sci.* **6**, 15 (1996).

[22] J. P. Perdew, K. Burke and M. Ernzerhof, *Phys. Rev. Lett.* **77**, 3865 (1996).

[23] J. P. Perdew, K. Burke and M. Ernzerhof, *Phys. Rev. Lett.* **78**, 1396 (1997).

[24] S. Grimme, J. Antony, S. Ehrlich and H. Krieg, *J. Chem. Phys*. **132**, 154104 (2010).

[25] A. K. Grimme, Homepage. http://www.thch.uni-bonn.de/tc/.

[26] A. Antony, C. Hakanoglu, A. Asthagiri and J. F. Weaver, *J. Chem. Phys*. **136**, 054702 (2012).

[27] H. J. Monkhorst and J. D. Pack, *Phys. Rev. B* **13**, 5188 (1976).

[28] F. Birch, *Phys. Rev.* **71**, 809 (1947).

[29] Y. Waseda, K. Hirata and M. Ohtani, *High Temp. High Pressures* **7**, 221 (1975).

[30] D. Feller, *J. Comput. Chem.* **17**, 1571 (1996).

[31] K. L. Schuchardt, B. T. Didier, T. Elsethagen, L. Sun, V. Gurumoorthi, J. Chase, J. Li and T. L. Windus, *J. Chem. Inf. Model.* **47**, 1045 (2007).

[32] R. Krishnan, J. S. Binkley, R. Seeger and J. A. Pople, *J. Chem. Phys.* **72**, 650 (1980).

[33] A. D. McLean and G. S. Chandler, *J. Chem. Phys.* **72**, 5639 (1980).

[34] R. C. de Berrêdo and F. E. Jorge, *J. Mol. Struct.: THEOCHEM* **961**, 107 (2010).

[35] K. Momma and F. Izumi, *J. Appl. Crystallogr.* **44**, 1272 (2011).

[36] L. P. Hammett, *J. Am. Chem. Soc*. **59**, 96 (1937).

[37] C. Hansch, A. Leo and R. W. Taft, *Chem. Rev*. **91**, 165 (1991).

[38] www.chemistryworld.com/opinion/hammett-equation/4011006.article

[39] P. J. Feibelman, B. Hammer, J. K. Nørskov, F. Wagner, M. Scheffler, R. Stumpf, R. Watwe and J. Dumesic, *J. Phys. Chem. B* **105**, 4018 (2001).

[40] G. Kresse, A. Gil and P. Sautet, *Phys. Rev. B*, 2003, **68**, 073401.

[41] Q. M. Hu, K. Reuter and M. Scheffler, *Phys. Rev. Lett.*, 2007, **98**, 176103.

[42] L. Schimka, J. Harl, A. Stroppa, A. Grüneis, M. Marsman, F. Mittendorfer and G. Kresse, *Nat. Mater*. **9**, 741 (2010).

[43] S. Gautier, S. N. Steinmann, C. Michel, P. Fleurat-Lessard and P. Sautet, *Phys. Chem. Chem. Phys.* **17**, 28921 (2015).

[44] J. Hu, M. Tanabe, J. Sato, K. Uosaki and K. Ikeda, *J. Am. Chem. Soc.* **136**, 10299 (2014).

[45] Y. Li, D. Lu, S. A. Swanson, J. C. Scott and G. Galli, *J. Phys. Chem. C* **112**, 6413 (2008).

[46] A. Ghalgaoui, N. Doudin, and M. Sterrer, *Langmuir* **33**, 91 (2017).

[47] G. Blyholder, *J. Phys. Chem.* **68**, 2772 (1964)

[48] H. Aizawa and S. Tsuneyuki, *Surface Science* **399**, 364 (1998).

[49] S. S. Sung and R. Hoffmann, *J. Am. Chem. Soc.* **107**, 578 (1985).

[50] Y. Gilman, P. B. Allen and M. S. Hybertsen, *J. Phys. Chem. C* **112**, 3314 (2008).

[51] P. Bennich, T. Wiell, O. Karis, M. Weinelt, N. Wassdahl, A. Nilsson, M. Nyberg, L. G. M. Pettersson, J. Stohr and M. Samant, *Phys. Rev. B* **57**, 9274 (1998).

[52] A. Föhlisch, M. Nyberg, J. Hasselström, O. Karis, L. G. M. Pettersson and A. Nilsson, *Phys. Rev. Lett.* **85**, 3309 (2000).

[53] A. Föhlisch, M. Nyberg, P. Bennich, L. Triguero, J. Hasselström, O. Karis, L. G. M. Pettersson, and A. Nilsson, *J. Chem. Phys*. **112**, 1946 (2000).

[54] A. Nilsson, M. Weinelt, T. Wiell, P. Bennich, O. Karis, N. Wassdahl, J. Stohr, and M. G. Samant, *Phys. Rev. Lett*., 1997, **78**, 2847 (1997).

[55] K. Gameel, I. M. Sharafeldin and N. K. Allam, *Phys. Chem. Chem. Phys.* **21**, 11476 (2019).

[56] N. Dimakis, T. Mion, and E. S. Smotkin, *J. Phys. Chem. C* **116**, 21447 (2012).

[57] N. Dimakis, F. A. Flor, N. E. Navarro, A. Salgado, and E. S. Smotkin, *J. Phys. Chem. C* **120**, 10427 (2016).

[58] N. Dimakis, M. Cowan, G. Hanson and E. S. Smotkin, *J. Phys. Chem. C* **113**, 18730 (2009).

[59] N. Dimakis, N. E. Navarro, T. Mion and E. S. Smotkin, *J. Phys. Chem. C* **118**, 11711 (2014).

[60] N. Dimakis, I. Salas, L. Gonzalez, N. Loupe and E. S. Smotkin, *J. Chem. Phys*. **150**, 024703 (2019).

[61] D. Astruc, Organometallic Chemistry and Catalysis, 608 pp. Springer, Berlin, 2007.

[62] R. Hoffmann, Solids and Surfaces: A Chemist's View of Bonding in Extended Structures; VCH Publishers: New York, 1988.

Chapter 4

Substrate-dependent Electron Transfer at SAMs/Metal Interface

In Chapter 3, the substituent effect of organic molecule on the nature and formation mechanism of chemical bonding induced by metal−SAMs interaction has been investigated. During the formation of SAMs system, the metal substrate also plays an essential role which is capable of adsorbing the organic monolayers. Adsorption of SAMs on different metals or on different surface orientations may change these characteristics. In this chapter, in tandem with the experimental observations by VSFG spectroscopy, we further investigated the metal substrate effect using the aryl isocyanide SAMs adsorbed on two commonly studied metal surface, Au and Ag surfaces with the aim of discussing quantitatively the extent to which the metal substrate affects the spectral behavior in terms of charge transfer between the molecules and the surface.

4.1 Introduction and Motivation

Chemical bonding interactions between organic molecules and metal surfaces determine many interfacial phenomena, such as charge transport [1−4], dynamics of electronic and vibrational excitations [5, 6] and chemical reactivity [7, 8] in the interfacial region between metal electrodes. The characterization of these interfacial bonds plays an important role in surface modification and functionalization. However, the complexity of the adsorbed structure of molecules on the surface, including the adsorption sites, and the coverage and orientation of the surface make it difficult to characterize them. Well-ordered SAMs on metal electrodes, an essential component of molecular

electronic devices, are a typical model for studying adsorbent−substrate interactions [9, 10]. Charge transfer between SAMs and metal electrodes is strongly dependent on the surface topography of the metal electrode. Therefore, before implementing SAMs for a particular application, it is necessary to understand how the intrinsic properties of the metal surface affect the interface structure. Thiol compounds on the gold surface are one of the widely studied systems because of the strong chemical bonding between the −S group and the atoms on the gold surface [11−20]. The aryl isocyanide molecule is also one of the important candidates because of the effective network of delocalized electrons between the π-orbitals of the benzene ring and the d-band of the metal surface, which is linked by the triple bond of the NC group [21−30]. The interaction between aryl isocyanide molecules and metal surfaces has been investigated using spectroscopic methods such as near-edge X-ray absorption fine structure spectroscopy (NEXAFS) and temperature-dependent surface-enhanced Raman spectroscopy (SERS) in relation to spectral signals and bonding properties [31].

The substate effect on the adsorbed molecule have been extensively investigated. An experimental study of biphenyl-based thiols on Au(111) and Ag(111) surfaces showed that these two surfaces possess opposite odd-even effect which represents the dependence between orientation of the biphenyl moiety and the number of methylene groups [32]. In addition, based on an investigation of photoinduced electron dynamics at the porphyrin/Ag(111), Ag(100) interfaces, it has been shown that different substrate orientation can also induce different energy alignment of the electronic states of the adsorbed molecule with respect to the Fermi level of the metal surface, and therefore governs both static and photoinduced electron transfer processes [33]. It is clear that the difference in the orientation of the substrate causes a difference in energy alignment of the

electronic states of the adsorbed molecules relative to the Fermi level of the metal surface and dominates both the static and photo-induced electron transfer process.

Quantum chemical calculations are also effective approach to investigate adsorption conformational changes for the structurally well-defined SAMs on metal substrates. They provides an intuitively clear picture of the chemical bonding interactions between SAMs and surfaces at the molecular level. The charge transfer between the SAMs and the metal substrate is an important factor for the interaction at the interface. NBO analysis converts the electronic wavefunction to a representation based on a localized basis and assigns the delocalized multi-electron wavefunction and electron pairs to one-center-two-electron orbital (lone pairs) and two-center-two-electron bond, which can be used to analyze the bonding mode of molecular systems based on the wave function [34]. This NBO analysis has recently been extended to periodic systems and implemented in the Periodic NBO software [35]. In pervious chapter, we have investigated the NC bond strength of the X−C_6H_4−NC molecule on the Pt surface by periodic-boundary density functional theory (DFT) calculation with a periodic NBO analysis, focusing on the substituent effect and the surface effect. The calculated NC stretching frequency and NC bond order from the NBO analysis were plotted as a function of the Hammett constant [36, 37] of the substituents X, showing that a "volcano-like" profile for an isolated molecule changes greatly for the molecules adsorbed on the Pt surface. This study demonstrated that the NBO analysis of chemical bonds of various organic molecules adsorbed on the surface can bring a deep understanding of the interaction of the molecule with the surface.

In this chapter, the molecular vibrations and electronic wavefunctions of aryl isocyanide molecules adsorbed on Au(111) and Ag(111) substrates are investigated by theoretical calculations, and supplemented with experimental results by VSFG spectroscopy, with the aim of discussing

quantitatively the extent to which the metal substrate affects the spectral behavior in terms of charge transfer between the molecules and the surface.

4.2 Computational Details

DFT calculations with a spin-polarized scheme were carried out for aryl isocyanide molecules with different para-substituted groups (H−C_6H_4−NC, OCH_3−C_6H_4−NC (OCH_3: electron-withdrawing group), NO_2−C_6H_4−NC (NO_2: electron-donating group)) adsorbed on Au(111) and Ag(111) surfaces with the Vienna Ab initio Simulation Package (VASP) software [38−41]. The Perdew-Burke-Ernzerhof functional in general gradient approximation (GGA-PBE) [42, 43] was selected as the XC functional, while van der Waals interactions were considered by using the D3 energy correction with zero damping during the optimization [44−46]. The core electrons are described by the projector-augmented wave (PAW) method [47, 48]. A plane-wave basis set with a kinetic energy cutoff of 540 eV was adopted for all calculations. Brillouin zone integration was carried out by the Methfessel−Paxton method [49] and Γ-point-centered 9 × 9 × 1 meshes of the *k* grid generated according to the Monkhorst–Pack scheme [50]. All structures were fully relaxed within a convergence of less than 10^{-6} eV for the total energy and 0.02 eV/Å for the force. The optimized lattice constants of bulk Au and Ag were determined to be 4.098 and 4.071 Å, respectively, which agree well with experimental values of 4.08 and 4.09 Å, respectively [51]. Using the equilibrium lattice constants, we modeled the Au(111) and Ag(111) surfaces with repeated slabs of four layers. The periodically repeated slabs are decoupled by 15 Å vacuum gaps. The aromatic molecules and the uppermost two metal layers were allowed to keep relax during the geometry relaxation. The bottom two layers were fixed at their bulk-truncated positions using the optimized lattice constants of the bulk metals. Otherwise, both Au(111) and Ag(111) surfaces are unreconstructed.

We also reproduced the vibrational spectra of aryl isocyanide molecule in gas phase and on metal substrates theoretically based on the Hessian matrix and Born effective charges which were calculated using the density functional perturbation theory (DFPT) [52, 53]. The DFPT based

method can provide theoretical vibrational spectra of adsorbate at metal surfaces [54−56] The anharmonic corrections have been included for each vibrational mode through a computation of the Morse-potential using the analytical method proposed by Torres *et. al.* [57].

To give a quantitative analysis of the chemical bonding of molecules adsorbed on the surface, we performed the periodic NBO calculation for analyzing orbital occupancy and generating visualization files. The plane-wave wave functions obtained from the static calculation using VASP for each optimized structure were projected onto the Gaussian-type basis sets taken from the EMSL basis set library [58, 59] For this purpose, we selected the jorge-DZP basis set [60−63]. Bader's quantum theory of atoms-in-molecules (QTAIM) analysis [64−67] was also carried out to investigate the change of electron distribution in molecules, using the algorithm by Henkelman *et al.*[68−71]. The Visualization for Electronic and Structural Analysis software (VESTA) was employed for orbital visualization [72].

4.3 Result and Discussion

4.3.1 structural and spectroscopic property of SAMs on Au and Ag surfaces

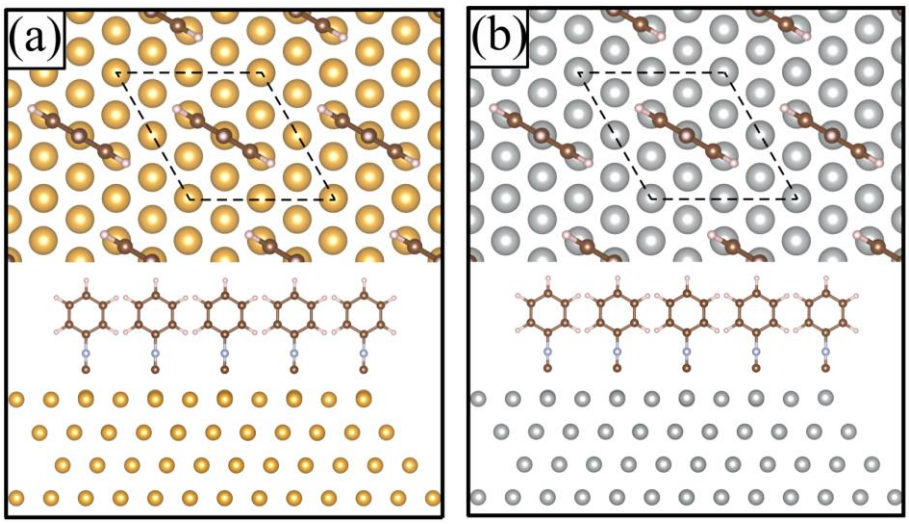

Figure 4.1. Top and side views of the optimized H−C_6H_4−NC molecule adsorbed on (a) Au(111) and (b) Ag (111) surfaces, in which gold, silver, gray, brown and red spheres denote Au, Ag, N, C and H atoms, respectively. The dash lines indicate the supercells used in this calculation.

Figure 4.1 shows the top and side views of the optimized H−C_6H_4−NC molecule adsorbed on Au(111) and Ag(111) surfaces. The corresponding NC bond lengths and metal−C interatomic distances are summarized in **Table 4.1**. Compared to the case of isolated molecules, the NC bond length is slightly shorter when adsorbed on the surface of Au or Ag. The adsorbed molecule is closer to the Au surface than to the Ag surface.

		Free	Au(111)	Ag(111)
H−C_6H_4−NC	*r*(N−C)/Å	1.184	1.176	1.178
	r(metal−C)/Å	-	2.012	2.115
OCH_3−C_6H_4−NC	*r*(N−C)/Å	1.184	1.176	1.179
	r(metal−C)/Å	-	2.016	2.120
NO_2−C_6H_4−NC	*r*(N−C)/Å	1.184	1.176	1.178
	r(metal−C)/Å	-	2.011	2.114

Table 4.1. Calculated values of N-C bond lengths (*r*(N−C)) and metal-C interatomic distances (*r*(metal−C)) of H−C_6H_4−NC, OCH_3−C_6H_4−NC and NO_2−C_6H_4−NC molecules in the isolated state and in the adsorbed state on Au(111) or Ag(111) surfaces.

Table 4.2 summarizes the experimental and calculated values of the C-N stretching vibrational frequencies. The vibrational frequencies for isolated molecules suitably agree with the experimental values obtained by FTIR spectroscopy in Table 4.2, and are also comparable with our previous work [25]. On the other hand, the "*volcano-like*" trend of vibrational frequency for isolated molecules as a function of Hammett constant is also in accordance with the results of FTIR spectroscopy and the previous report [25]. This demonstrates the validity of our calculation models and calculating vibrational spectra using the DFPT method.

		Experiment/cm^{-1}			Calculation/cm^{-1}		
substituent	σ_p	Free	Au	Ag	Free	Au	Ag
$-OCH_3$	−0.27	2122	2194	2185	2131	2194	2159
−H	0	2123	2199	2186	2133	2196	2165
$-NO_2$	0.78	2119	2194	2176	2125	2177	2150

Table 4.2. The CN stretching frequency for aryl isocyanide molecule on Au and Ag surface obtained from VSFG spectroscopy and those of free molecules in dilute hexane solutions obtained by the FTIR spectroscopy. The experimental results are extracted from doctoral thesis of Dr. Mikio Ito. The calculated frequencies based on the DFPT method are also shown.

The specific theoretical spectra for three isolated molecules and molecules adsorbed on Au and Ag surface are shown in **Figure 4.2**. The peaks centered at 2131 cm^{-1} ($-OCH_3$ *para*-substituted), 2133 cm^{-1} (no substitution) and 2125 cm^{-1} ($-NO_2$ *para*-substituted) for isolated molecules can be assigned to the NC stretching frequency (ν_{NC}). The multiple peaks at 3000 ~ 3100 cm^{-1} in the spectra belong to the stretching vibrations (ν_{CH}) of the C−H bonds in the OCH_3 group and C−H bonds in the aromatic ring. In addition to these spectral features, the symmetric and asymmetric stretches of C−C bonds in the aromatic rings appear in the region around 1500 cm^{-1}, and the vibrational modes identified near 1000 cm^{-1} are due to the C−H in-plane bending. As our focus in this study is to show the metal substrate effect on the interfacial structure, the stretching vibration of the contacting NC bond is expected to play a more significant role than other vibrations. Thus, most attention will be paid to the NC stretching frequency in the rest of this work.

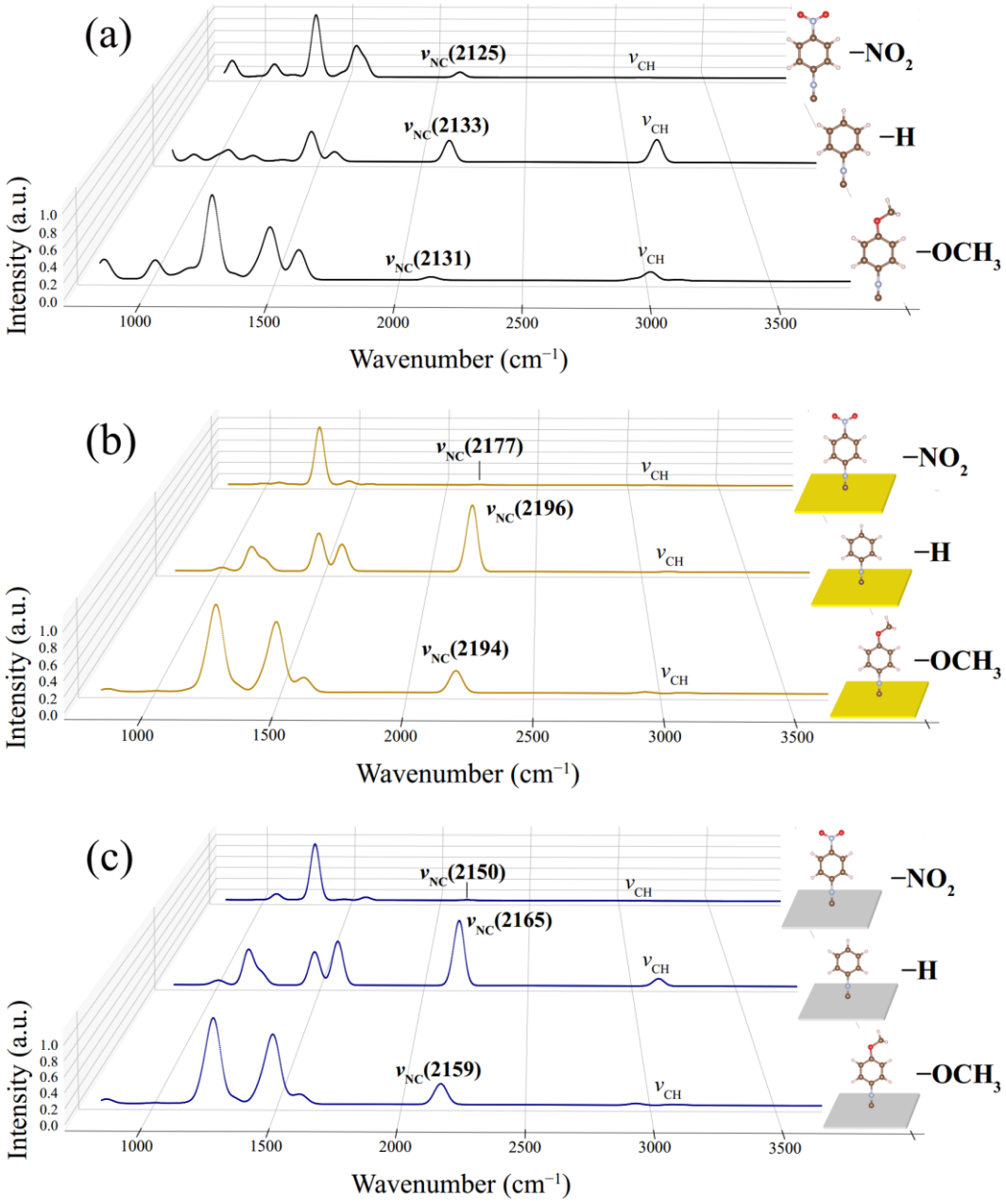

Figure 4.2. Calculated vibrational spectra of X−C_6H_4−NC molecule (X = OCH_3, H, NO_2) (a) without substrate, (b) on the Au(111) surface, and (c) on the Ag(111) surface.

After adsorption, we found that the NC stretching frequency undergoes a blue-shift for Au(111) and Ag(111) surfaces compared to the isolated molecule case as shown in Fig. 4.2(a), respectively. Importantly, the frequency in the case of Au surface possess a larger blue-shift than

Ag surface (50~60 cm^{-1} versus 30~40 cm^{-1}). This blue-shift in spectra has also been found in the VSFG spectroscopic study. Similar to the theoretical results, the VSFG spectroscopic results also show that the blue-shift of NC stretching frequency in the case molecule adsorbed on Au(111) is more significant as compared to that in the case of Ag(111) adsorption (70~76 cm^{-1} versus 55~65 cm^{-1}).

Combining the experimental VSFG spectra and theoretical investigations in this section, it was concluded that the Au(111) surface exhibits more significant effect on the blue-shift in NC stretching vibration than the Ag(111) surface, reflecting the metal substrate effect on the vibrational behavior at the interface.

4.3.2 electronic structure of SAMs/substrate interfaces

To ascertain the general mechanism behind this trend, the electronic structure calculations have been performed in this section. At first, we carried out the density of states (DOS) calculation to reveal how the molecular states of aryl isocyanide SAMs are redistributed due to their interaction with the adsorbed metal substrates. The total DOS can be further projected onto the atomic orbitals (PDOS) to assign the contributions from individual atoms. For a clear view, only the NC group instead of all atoms of the adsorbate has been included, and the atomic orbitals whose contribution to the total DOS is lower than 3% will not be considered here. **Figure 4.3** gives the projected DOS (PDOS) onto the NC group in isolated H−C_6H_4−NC molecule, clean Au and Ag surfaces as well as NC group of H−C_6H_4−NC molecule adsorbed on Au and Ag surfaces, respectively. As revealed by Fig. 4.3a, density distribution for NC group in the isolated molecule is discrete and the main component of total DOS is dictated by the C and N 2p orbitals. Fig. 4.3b shows the PDOS of clean Au and Ag surface before adsorption. A sharp drop was observed in the energy range from −2 to

−1 eV for Au and −3 to −2 eV for Ag. Contribution of Au 5d and Ag 4d states is more significant as compared to Au 6s, 6p states and Ag 5s, 5p states in the energy range of −6 to −1 eV for Au and −6 to −2 eV for Ag, respectively. However, this situation is notably different near the Fermi energy, at which the s and p states of two metals produce almost equal contributions comparing with the d states. This leads to more pronounced hybridization between d and sp states of the clean surface near the Fermi energy region.

(a)

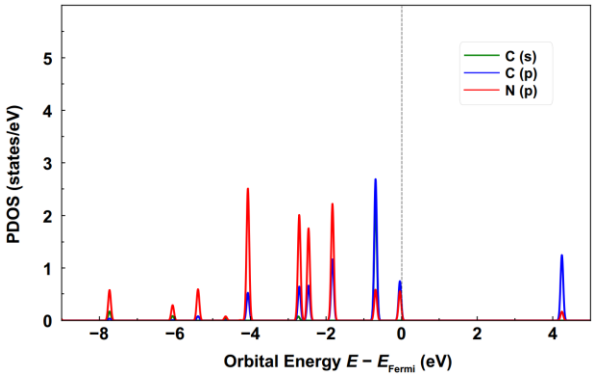

(b)

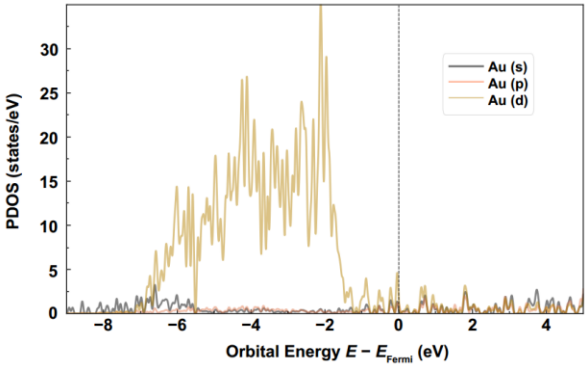

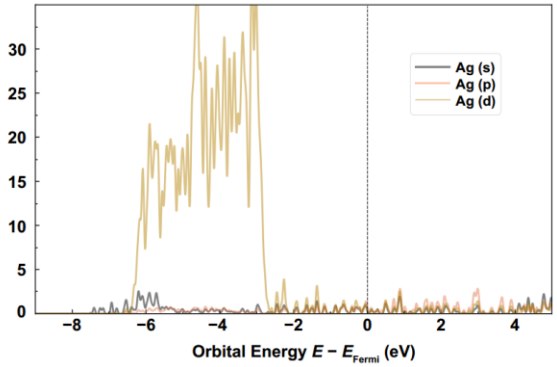

(c)

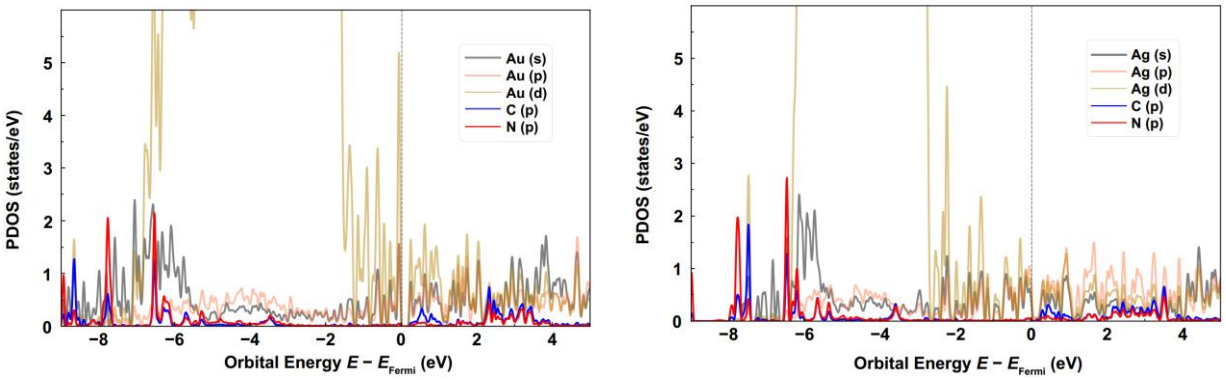

Figure 4.3. PDOS projected onto (a) NC group in H−C_6H_4−NC molecule in gas phase, (b) clean Au(111) and Ag(111) surfaces without adsorption (left and right panels, respectively) and (c) NC group in H−C_6H_4−NC molecule adsorbed on Au(111) and Ag (111) surfaces (left and right panels, respectively). Fermi levels are shown by the black dashed lines located at 0 eV. Only atomic orbitals whose DOS contributes over 3% of total DOS have been considered.

Then, Fig. 4.3c gives the PDOS projected on the NC group in H−C_6H_4−NC molecule adsorbed on Au and Ag surfaces. The hybridization between the electronic levels of the adsorbed SAMs and the metal substrate results in the formation of several bonding and antibonding states, showing different features in comparison to the PDOS computed for isolated molecule. First, the sharp states of isolated molecule, particularly the C 2p states were found to be broadened into resonance and shifted to a lower energy around the bottom of Au valence band region, indicating the electron transfer from adsorbate state 5σ with Au d states which is defined as the σ donation process. On the other hand, 1π level of NC interacts with Au d orbitals, resulting in overlapping of PDOS around −4 to −7 eV, as well as the couplings above the Fermi energy which are ascribed to electron transfer from d states to π* antibonding orbitals of the NC group [73, 74].

PDOS of NC group in H−C_6H_4−NC molecule adsorbed on Ag surface is almost identical to that of Au surface, as depicted in the right panel of Fig. 4.3c. Herein, the PDOS analysis shows that the 5σ orbital of the NC bond donates electrons to the metal surface to strengthen the Au/Ag−C bonds, while the NC π* orbital accepts the back-donated electrons from the Au/Ag d orbitals, leading to the weakening of the NC bond.

A Bader charge analysis of the electronic density distribution in **Table 4.3** indicates that, upon adsorption on Au(111) and Ag(111) surfaces, the adsorbed H−C_6H_4−NC molecule lose 0.03 and gain 0.07 electrons, respectively, when compared with the isolated molecule. Such limited values seems to point out the weak interaction between SAMs and metal substrates. However, we found the C atom which contacting with the metal surface was positively charged by 0.15 electrons for adsorption on Au(111) surface, and negatively charged by 0.01 electron for adsorption on Ag(111) surface. This difference highlights the metal substrate effect and relates to the strength of σ donation/π back-donation which will be further discussed later in a quantitative manner.

H−C_6H_4−NC on Au(111) surface			
	Au	C	N
before adsorption/*e*	−0.036	+1.640	−2.662
after adsorption/*e*	+0.151	+1.791	−2.781
H−C_6H_4−NC on Ag(111) surface			
	Ag	C	N
before adsorption/*e*	−0.023	+1.640	−2.662
after adsorption/*e*	+0.137	+1.635	−2.725

Table 4.3. Bader charge data for H−C_6H_4−NC molecule adsorbed on (a) Au(111) and (b) Ag (111) surfaces, charges for isolated molecule and clean metal surface have also been listed for comparison.

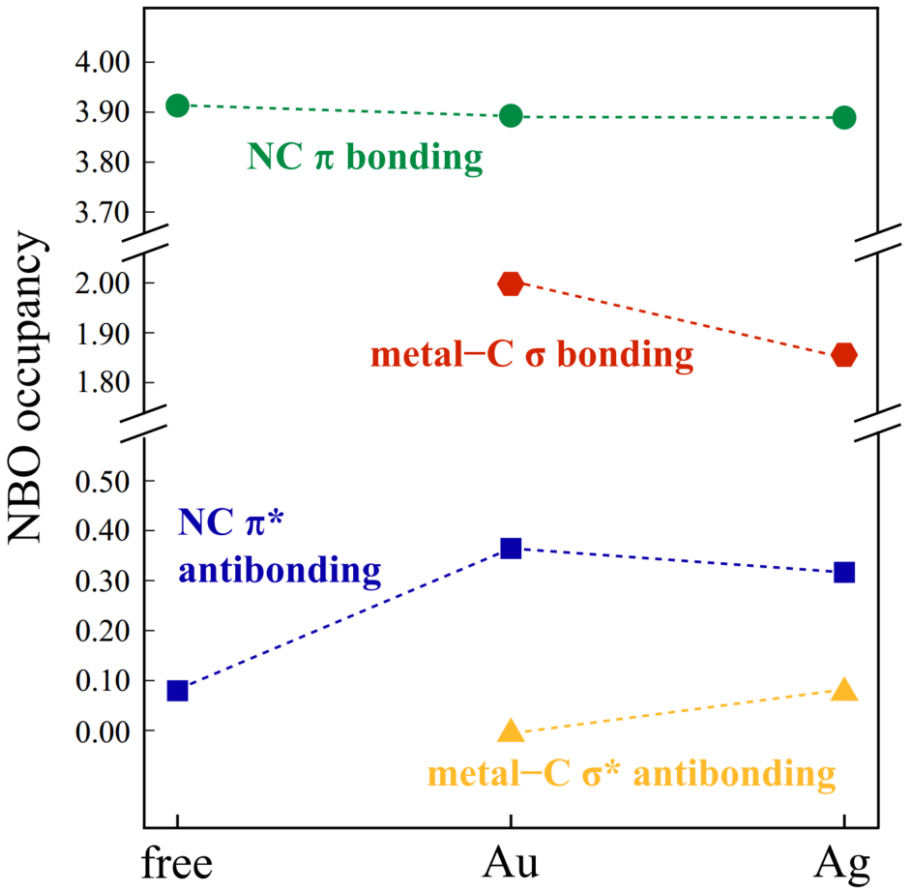

Figure 4.4. Calculated NBO occupancy in NC π bonding orbitals, metal−C σ bonding orbitals, NC π bonding orbitals, and metal−C σ antibonding orbitals for free H−C_6H_4−NC molecule, and molecule adsorbed on Au and Ag surfaces.

Moreover, the NBO algorithm in periodic implementation were employed to quantitatively analyze the surface chemical bonding interaction and rationalize the differences between Au(111) and Ag(111) in depth understanding. **Figure 4.4** shows our calculated NBO occupancy in several representative orbitals, including NC π bonding orbitals, metal−C σ bonding orbitals, NC π bonding orbitals, and metal−C σ antibonding orbitals for free H−C_6H_4−NC molecule, and molecule adsorbed on Au and Ag surfaces, respectively.

We start the discussion from the NBO occupancies in NC π bonding orbitals as indicated by the green points. There are two components of NC bonding orbitals, including in-plane and out-of-plane components, as well as their spin up and down components, as presented in last chapter. For simplicity, their summation, has been given here. There was only a slight decrease in occupancy from 3.913*e* (free molecule) to 3.893*e* (Au) and 3.889*e* (Ag) upon adsorption. Electron leaves from the NC π bonding orbitals after binding to the surface, although the amount is very low (~0.02 *e*).

Then, we focus on the metal−C σ bonding orbitals represented by the red points. The occupancy of above 1.98*e* for Au surface is in agreement with the picture of a nearly perfect localized two-center bond in the ideal state, suggesting that such adsorption bond is formed almost solely from the C atom (lone pair orbital) of the isolated SAMs molecule. In comparison to Au surface, Ag−C σ bonding orbital has an occupancy of 1.86*e*, which is relatively lower than that in Au−C σ bonding orbital. The σ donation−π back-donation mechanism demonstrates that metal−C bond formation is attributed to the interaction between NC 5σ and a hybrid of Au (Ag) d_z^2 and Au (Ag) sp orbitals. Since the NC 5σ orbital has a weak antibonding nature, metal−C σ bond formation by the σ donation will the suppression of this antibonding character, leading to the strengthening of the NC bond and a blue-shift in the NC stretching frequency [75]. The values of occupation number of Au or Ag−C σ bonding orbitals can be used to evaluate the strength of σ donation. The larger population in the Au−C σ bonding orbital indicates that stronger σ donation occurs at the interface between SAMs and Au surface after binding to the surface, which is responsible for the further blue-shift in ν_{NC} than Ag surface.

NC π* antibonding orbital plays an important role during the π back-donation, its occupancy (blue points) can therefore be used as a measure of the π back-donation strength. NC π*

antibonding orbital of SAMs on Au surface have larger occupancy of ~0.36*e* in comparison to that of SAMs on Ag surface (~0.32*e*). The relatively larger occupancy number in NC π* antibonding orbital reveals the stronger π back-donation, which induces the weakening of NC bonds and the red-shift in vibrational frequency.

NBO occupancy in the Au/Ag−C σ* antibonding orbitals in indicated by the yellow points. Ag−C σ* has larger occupancy (~0.08*e*) than Au (lower than 0.02*e*), showing the stronger Pauli repulsion between the NC 5σ molecular orbitals and the metal surface d-states in Ag case. Both Au−C σ* and Ag−C σ* antibonding orbitals have smaller occupancy than previously reported Pt surface case [25]. Variations in the NBO occupancies of the NC σ bonding and σ* antibonding (not shown in Fig. 4.4) orbitals are proven can influence the overall electron transfer to a very small extent, and thus are insensitive to the metal surface. Additionally, varying the substituent group of SAMs lead to very limited changes compared with the change of metal surface.

Having the above discussion in mind, we can summarize that SAMs on Au surface has both stronger σ donation and π back-donation in comparison to those on Ag surface. In conjunction with the spectral results by VSFG and calculation, it can be revealed that the overall blue-shift in NC stretching frequency after binding to the metal surface is attributed to the more significant role of σ donation over π back-donation, both for Au and Ag. More importantly, the stronger σ donation in the Au case induces the further blue-shift in vibrational frequency than Ag surface, showing the metal substrate effect on electron transfer at the interfacial region.

4.4 Summary of This chapter

We have investigated the metal substrate-dependent electron transfer between adsorbate SAMs and two typical metal surfaces−Au(111) and Ag(111), using VSFG spectra complemented by theoretical calculations. A self-assembly molecular system has been constructed by immersing the Au(111) and Ag(111) thin films prepared by vapor deposition in the isocyanide solutions. The fabricated structures have been well characterized by the surface-specific vibrational sum frequency generation spectroscopy. The spectroscopic result shows a blue-shift in vibrational frequency compared to that of the isolated molecules, while the blue-shift in the case of using Au(111) as substrate is more significant than that in the Ag(111) case. Furthermore, to rationalize the experimental findings, we carried out the theoretical calculations including study of spectra based on density functional perturbation theory and the Natural Bonding Orbitals algorithm. Computational result supports experimental observations and the more significant σ donation strength of SAMs on Au over Ag has been considered as the decisive factor in determining the further blue-shift in vibrational frequency for Au surface. Our study provides systematic insights into the relationship between vibrational frequency and orbital population, suggesting opportunities for designing molecule/metal interfaces with desired electronic properties using diverse metal substrates.

4.5 References

[1] M. Ratner, *Nat. Nanotechnol.*, 2013, **8**, 378 (2013).

[2] L. Sun, Y. A. Diaz-Fernandez, T. A. Gschneidtner, F. Westerlund, S. Lara-Avila and K. Moth-Poulsen, *Chem. Soc. Rev.* **43**, 7378 (2014).

[3] D. Xiang, X. Wang, C. Jia, T. Lee and X. Guo, *Chem. Rev.* **116**, 4318 (2015).

[4] C. Jia and X. Guo, *Chem. Soc. Rev.* **42**, 5642 (2013).

[5] H. Chadwick and R. D. Beck, *Chem. Soc. Rev.* **45**, 3576 (2016).

[6] G.-H. Deng, Y. Qian and Y. Rao, *J. Chem. Phys.* **150**, 024708 (2019).

[7] P. Saalfrank, *Chem. Rev.* **106**, 4116 (2006).

[8] W. R. Browne and B. L. Feringa, *Annu. Rev. Phys. Chem.* **60**, 407 (2009).

[9] R. M. Metzger, *Chem. Rev.* **115**, 5056 (2015).

[10] A. Vilan and D. Cahen, *Chem. Rev.* 117, 4624 (2017).

[11] H. Häkkinen, *Nat. Chem*. **4**, 443 (2012).

[12] R. Nuzzo and D. Allara, *J. Am. Chem. Soc.* **105**, 4481 (1983).

[13] R. Nuzzo, F. Fusco, and D. Allara, *J. Am. Chem. Soc*. **109**, 2358 (1987).

[14] R. Nuzzo, L. Dubois, and D. Allara, *J. Am. Chem. Soc.* **112**, 558 (1990).

[15] M. D. Porter, T. Bright, D. Allara, and C. Chidsey, *J. Am. Chem. Soc.* **109**, 3559 (1987).

[16] C. Chen, M. Mrksich, S. Huang, G. Whitesides, and D. Ingber, *Science* **276**,1425 (1997).

[17] X. Jiang, R. Ferrigno, M. Mrksich, and G. Whitesides, *J. Am. Chem. Soc*. **125**, 2366 (2003).

[18] X. Jiang, D. Bruzewicz, A. Wong, M. Piel, and G. Whitesides, *Proc. Nat. Acad. Sci*. **102**, 975 (2005).

[19] R. L. McCreery, *Chem. Mater*. **16**, 4477 (2004).

[20] K. Sotthewes, V. Geskin, R. Heimbuch, A. Kumar, and H. J. W. Zandvliet, *APL Mater*. **2**, 010701 (2014).

[21] M. Kiguchi, S. Miura, K. Hara, M. Sawamura, and K. Murakoshi, *Appl. Phys. Lett.* **89**, 213104 (2006).

[22] K. Ikeda, N. Fujimoto, and K. Uosaki, *J. Phys. Chem. C* **118**, 21550 (2014).

[23] M. Ito, H. Noguchi, K. Ikeda and K. Uosaki, *Phys. Chem. Chem. Phys.* **12**, 3156 (2010).

[24] W. Hu, S. Duan, Y. Zhang, H. Ren, J. Jiang and Y. Luo, *Phys. Chem. Chem. Phys.* **19**, 32389 (2017).

[25] B. Wang, M. Gao, K. Uosaki, and T. Taketsugu, *Phys. Chem. Chem. Phys.* **22**, 12200 (2020).

[26] J. Hu, N. Hoshi, K. Uosaki and K. Ikeda, *Nano Lett.* **15**, 7982 (2015).

[27] K. Ikeda, J. Sato and K. Uosaki, *J. Photochem. Photobiol., A* **221**, 175 (2011).

[28] K. Ikeda, A. Kimura and K. Uosaki, *J. Electroanal. Chem.* **800**, 151 (2017).

[29] K. Ikeda, J. Sato, N. Fujimoto, N. Hayazawa, S. Kawata and K. Uosaki, *J. Phys. Chem. C* **113**, 11816 (2009).

[30] K. Ikeda, N. Fujimoto, H. Uehara and K. Uosaki, *Chem. Phys. Lett.* **460**, 205 (2008).

[31] S. Kim, K. Ihm, T.-H. Kang, S. Hwang and S.-W. Joo, *Surf. Interface Anal.* **37**, 294 (2005).

[32] H. T. Rong, S. Frey, Y.-J. Yang, M. Zharnikov, M. Buck, M. Wühn, C. Wöll and G. Helmchen, *Langmuir* **17**, 1582 (2001).

[33] S. Tognolini, S. Ponzoni, F. Sedona, M. Sambi and S. Pagliara, *J. Phys. Chem. Lett.* **6**, 3632 (2015).

[34] F. Weinhold and C. Landis, *Valency and Bonding–A Natural Bond Orbital Donor-Acceptor Perspective*; Cambridge University Press: Cambridge, 2005; pp 1−44.

[35] B. D. Dunnington and J. R. Schmidt, *J. Chem. Theory Comput.* **8**, 1902 (2012).

[36] L. P. Hammett, *J. Am. Chem. Soc*. **59**, 96 (1937).

[37] C. Hansch, A. Leo and R. W. Taft, *Chem. Rev*. **91**, 165 (1991).

[38] G. Kresse and J. Hafner, *Phys. Rev. B* **47**, 558 (1993).

[39] G. Kresse and J. Hafner, *Phys. Rev. B* **49**, 14251 (1994).

[40] G. Kresse and J. Furthmüller, *Phys. Rev. B* **54**, 11169 (1996).

[41] G. Kresse and J. Furthmüller, *Comput. Mater. Sci.* **6**, 15 (1996).

[42] J. P. Perdew, K. Burke and M. Ernzerhof, *Phys. Rev. Lett.* **77**, 3865 (1996).

[43] J. P. Perdew, K. Burke and M. Ernzerhof, *Phys. Rev. Lett.* **78**, 1396 (1997).

[44] S. Grimme, J. Antony, S. Ehrlich and H. Krieg, *J. Chem. Phys*. **132**, 154104 (2010).

[45] A. K. Grimme, Homepage. http://www.thch.uni-bonn.de/tc/.

[46] A. Antony, C. Hakanoglu, A. Asthagiri and J. F. Weaver, *J. Chem. Phys*. **136**, 054702 (2012).

[47] P. E. Blöchl, *Phys. Rev. B* **50**, 17953 (1994).

[48] G. Kresse and D. Joubert, *Phys. Rev. B* **59**, 1758 (1999).

[49] M. Methfessel, *Phys. Rev. B: Condens. Matter Mater. Phys*. **40**, 3616 (1989).

[50] H. J. Monkhorst and J. D. Pack, *Phys. Rev. B* **13**, 5188 (1976).

[51] *Handbook of Chemistry and Physics*; Lide, D. R., Ed.; CRC Press: Boca Raton, FL, 2008; pp 12−15.

[52] P. Giannozzi and S. Baroni, *J. Chem. Phys.* **100**, 8537 (1994).

[53] S. Baroni, S. De Gironcoli, A. Dal Corso, and P. Giannozzi, *Rev. Mod. Phys.* **73**, 515 (2001).

[54] S.-S. Lee, B. Kim and S. Lee, *J. Phys. Chem. C* **118**, 20840 (2014).

[55] M. Seydou, J. Teyssandier, N. Battaglini, G. T. Kenfack, P. Lang, F. Tielens, F. Maurel and B. Diawara, *RSC Adv.* **4**, 25698 (2014).

[56] A. Davantès, D. Costa, and G. Lefèvre, *J. Phys. Chem. C* **119**, 12356 (2015).

[57] J. A. Garrido Torres, J. P. Götze, F. Grillo, N. V. Richardson, H. Früchtl, C. A. Hooley and R. Schaub, *Phys. Rev. B* **100**, 035433 (2019).

[58] A. Antony, C. Hakanoglu, A. Asthagiri and J. F. Weaver, *J. Chem. Phys*. **136**, 054702 (2012).

[59] H. J. Monkhorst and J. D. Pack, *Phys. Rev. B* **13**, 5188 (1976).

[60] F. E. Jorge, P. S. Sagrillo and A. R. de Oliveira, *Chem. Phys. Lett.*, **432**, 558 (2006).

[61] P. L. Barbieri, P. A. Fantin and F. E. Jorge, *Mol. Phys.* **104**, 2945 (2006).

[62] S. F. Machado, G. G. Camiletti, A. Canal Neto, F. E. Jorge and R. S. Jorge, *Mol. Phys.* **107**, 1713 (2009).

[63] A. C. Neto, E. P. Muniz, R. Centoducatte and F. E. Jorge, *THEOCHEM* **718**, 219 (2005).

[64] R. F. W. Bader, *Chem. Rev.* **91**, 893 (1991).

[65] R. F. W. Bader, *Atoms in Molecules: A Quantum Theory*, Oxford University Press, USA, 1994.

[66] R. F. W. Bader, *Acc. Chem. Res.* **18**, 9 (1985).

[67] R. F. W. Bader. In: P. v. Schleyer, (Ed.). *Encyclopedia of Computational Chemistry.* (John Wiley and Sons, Chichester, U.K., 1998), pp. 64−86.

[68] W. Tang, E. Sanville and G. Henkelman, *J. Phys.: Condens. Matter* **21**, 084204 (2009).

[69] E. Sanville, S. D. Kenny, R. Smith and G. Henkelman, *J. Comp. Chem.* **28**, 899 (2007).

[70] G. Henkelman, A. Arnaldsson, and H. Jónsson, *Comput. Mater. Sci.* **36**, 354 (2006).

[71] M. Yu and D. R. Trinkle, *J. Chem. Phys.* **134**, 064111 (2011).

[72] K. Momma and F. Izumi, *J. Appl. Crystallogr.* **44**, 1272 (2011).

[73] Y. Li, D. Lu, S. A. Swanson, J. C. Scott and G. Galli, *J. Phys. Chem. C* **112**, 6413 (2008).

[74] Y. Gilman, P. B. Allen and M. S. Hybertsen, *J. Phys. Chem. C* **112**, 3314 (2008).

[75] D. Astruc, Organometallic Chemistry and Catalysis, 608 pp. Springer, Berlin, 2007.

Chapter 5

Catalytic Functionalization of C doped h-BN Surface

As discussed throughout chapter 3 and chapter 4, we focused on two individual components of self-assembled monolayers adsorbed on noble metal surfaces, the substituent and metal substrate. Their respective role during the bonding formation at the interface structure has been clarified. In this Chapter, our attention has moved from the electron transfer across the interface to the catalytic reactions that occur on single C atom doped h-BN surface. Herein, we investigated two typical oxidation reaction, CO oxidation and C_2H_4 oxidation occurring at this doped surface. The reaction mechanism and the favorable transition states have been clarified.

5.1 Introduction and Motivation

The molecular oxygen can activate and dissociate on the heterogeneous catalyst surface and induce the catalytic reactions. Such activation plays an important role in a variety of practical applications, including electrochemistry in fuel cells, combustion reaction, and selective oxidation reaction [1, 2]. To design such kind of heterogeneous catalyst, much effort have been made in this field. Current used catalysts for the chemical reactions with molecular oxygen are mostly based on the platinum-group metals (PGMs), it has been found such catalysts can effectively induce the oxidation reaction [3, 4]. Although the PGMs based catalysts have high efficiency, the low abundance and the high price strongly hinder the industrial applications of the catalysts [5]. Therefore, it is still an urgent work to develop the novel effective heterogeneous catalysts which have high efficiency for molecular oxygen activation and have low cost feature [5, 6].

Graphene, a typical two-dimensional metal-free material, has attracted huge interest for the catalytic reactions due to its wide surface area and distinctive chemical and physical properties. However, delocalized uniform charge distribution of graphene results in its inactive nature for catalytic reactions [7]. To overcome this issue, various dopants and vacancy defects have been considered to add to the graphene surface. Previous theoretical and experimental studies have found that the high efficiency of graphene materials can be achieved by including some single transition metal elements or non-metal atoms (B, N, P, S etc.) which can change the electronic structure and electron distribution [8−10]. Graphene doped with B and N elements has become an active heterogeneous catalyst for aerobic oxidation reactions [11].

Hexagonal boron nitride (h-BN) has the similar geometry with graphene. In comparison to the graphene, h-BN has a wide band gap and high thermal stability, and has been generally considered as an insulator inactive catalysts [12]. However, recent studies show that h-BN can be effectively functionalized by various tools including atomic dopant, defect and metal support and reveals unusual catalytic ability [12−23]. Such unusual catalytic ability arises from the interaction and activation of the adsorbed molecular oxygen (O_2) with the surface catalyst due to the presence of the defect states in the forbidden region of h-BN catalyst [12]. Specifically, we have found the h-BN nanosheets deposited on Au(111) support shows exceptional electro-catalytic ability for oxygen reduction reaction (ORR) [16, 24], as well as the hydrogen evolution reaction (HER) [19]. As for the HER, the BN/Au catalyst exhibits the catalytic activity similar to that of Pt surface, which is widely recognized as one of most best catalysts. Despite the high potential of BN based materials for development of non-metal catalysts, a serious limitation should also be mentioned: the active sites that inducing the catalytic reactions are only restricted to the dopant atoms with a small surface area.

Two important conditions should be satisfied for activation of the adsorbed O_2 molecule on surface: a). adsorption energy should be an appropriate value, too weak adsorption cannot keep the activated O_2 molecule bonded to the surface, while too strong adsorption makes leaving the reaction products from the surface difficult to occur after the reaction; b). the surface area should be wide enough to increase the efficiency of heterogeneous catalysts. At present, PGMs based catalysts have been widely recognized as the suitable catalysts for satisfying these two condition in different reactions [25, 26]. Besides, we have recently found that doping one carbon atom into a position of boron atom in the hexagonal h-BN structure, the newly formed C_B@h-BN structure becomes a *n*-type semiconducting material with considerable catalytic activity for molecular O_2 activation over the wide area even extended far away from the C impurity [27]. Different from the inert nature of pure h-BN monolayer for O_2 adsorption and activation, C_B@h-BN sheet can adsorb and activate O_2 molecule even far from the doped C impurity. The study has also shown that the active area for catalytic reaction in C_B@h-BN strongly depends on the energy gap between the highest occupied defect level of doped C impurity, and the bottom of conduction band (CB) of the h-BN surface. In particular, the defect states should be delocalized and close to the CB of surface to activate the O_2 in the wide surface area.

In this study, we are aiming to examine the distance dependence of activation barriers for some prototypical oxidation reactions as a function of the distance between the C impurity and the active sites. Specifically, CO oxidation and C_2H_4 epoxidation induced by O_2 activation which are of fundamental importance during practical industrial applications have been selected as the target reactions due to their industrial and fundamental importance. Through the analyze of reaction energy profiles and the distance dependence of activation barriers on the distance between active

sites and the doped C impurity, we aim to demonstrate the reaction mechanism of two oxidation reactions and evaluate the catalytic activity of C_B@h-BN surface catalysts.

5.2 Computational Details

The DFT calculations were carried out with the Wu-Cohen (WC) generalized-gradient-approximation (GGA) exchange-correlation functional [28], which has been implemented in the Plane-Wave Self-Consistent Field (PWSCF) program of Quantum Espresso package [29, 30]. It has been revealed that the WC functional can accurately reproduces the lattice parameters, crystal geometries, as well as surface energies of solid system with layered conformation including graphite and h-BN which shows weak interaction between layers [14]. The plane-wave basis set has been used with the Troullier-Martins norm-conserving pseudopotentials. The spin polarization and periodic boundary condition (PBC) have been considered for all systems. The energy cutoff of 80 Ry has been chosen to obtain the full convergence in total energies and forces. Lattice parameter of the bulk h-BN monolayer was fully optimized using the Monkhorst-Pack 10×10×4 k-point mesh for the sampling of the Brillouin zone. Our calculated lattice parameters a = b = 2.504 Å, and c = 6.656 Å are in great agreement with the experimental values [31]: a = b = 2.524 ± 0.020 Å and c = 6.684 ± 0.020 Å. The climbing image nudged elastic band (ci-NEB) method is utilized for searching the transition states and minimum energy pathways [32]. The atoms in molecules method (AIM) is employed for charge analysis [33]. To view the electron density difference, we used the package of Visualization for Electronic and Structural Analysis software (VESTA) [34]. The h-BN surface is modeled by a one-layer slab containing 6×6 unit cells. Vacuum region of 15 Å in the (001) direction is used to separate the periodically replicated slabs. Due to the large size of the used supercell, only the Γ point is used for sampling the Brillouin zone in this study. The adsorption energy is calculated by the following equation

$E_{ad} = E_{tot} - E_{C@h\text{-}BN} - E_{O2} - E_{mol}$, where E_{tot}, $E_{C@h\text{-}BN}$, E_{O2}, E_{mol} indicate the free energy of the entire system, the C@h-BN monolayer, the isolated oxygen molecule and the CO or C_2H_4 reactants, respectively.

5.3 Result and Discussion

5.3.1 adsorption of O_2, CO and C_2H_4 molecules on C_B@h-BN surface

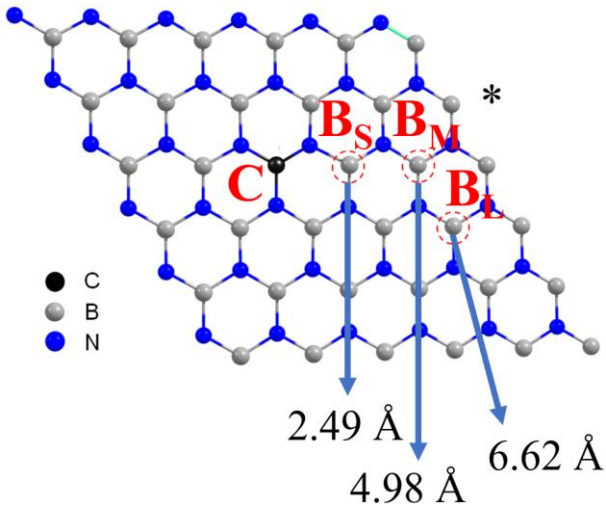

Figure 5.1. Computational model for the C-doped h-BN monolayer and three B active sites for O_2 adsorption in this study. The C, B, N atoms are indicated by black, gray and blue, respectively.

We firstly consider the adsorption of O_2, CO and C_2H_4 molecules on the C_B@h-BN into the B active sites. To obtain the most stable configurations of CO and C_2H_4 molecules adsorbed on the C_B@h-BN monolayer, various initial configurations were considered followed by the full optimization of the entire system, which is similar to the approach used in a previous work [18]. As the O_2 molecule can only adsorb on the B active sites of the surface [18], we selected three adsorption sites, B_S, B_M, B_L (**Figure 5.1**) with different distances from the doping C atom of 2.49 Å, 4.98 Å, and 6.62 Å, respectively. A previous theoretical work of doping of C to B positions in

the h-BN monolayer shows the planar geometry structure of h-BN sheet is less affected by the doping C [18]. However, the C doping considerably influences the electronic structure of h-BN monolayer and results in the appearance of defect levels in the forbidden zone of the surface. It has been found that the occupied 2*p* states of the doped C atom at the bottom of the CB of h-BN monolayer can considerably influence the chemical property of the surface, resulting in the adsorption and activation of O_2 molecule in the surface area extending far from the doped C atom.

Figure 5.2 lists the most stable configurations after optimization of CO and C_2H_4 and O_2 molecules adsorbed in the vicinity of C_B impurity in the h-BN monolayer. The calculation of adsorption energy shows CO molecule weakly adsorbs on top of the C site with the adsorption energy of −0.19 eV (−4.4 kcal/mol). The interaction with the B active sites is very limited with the

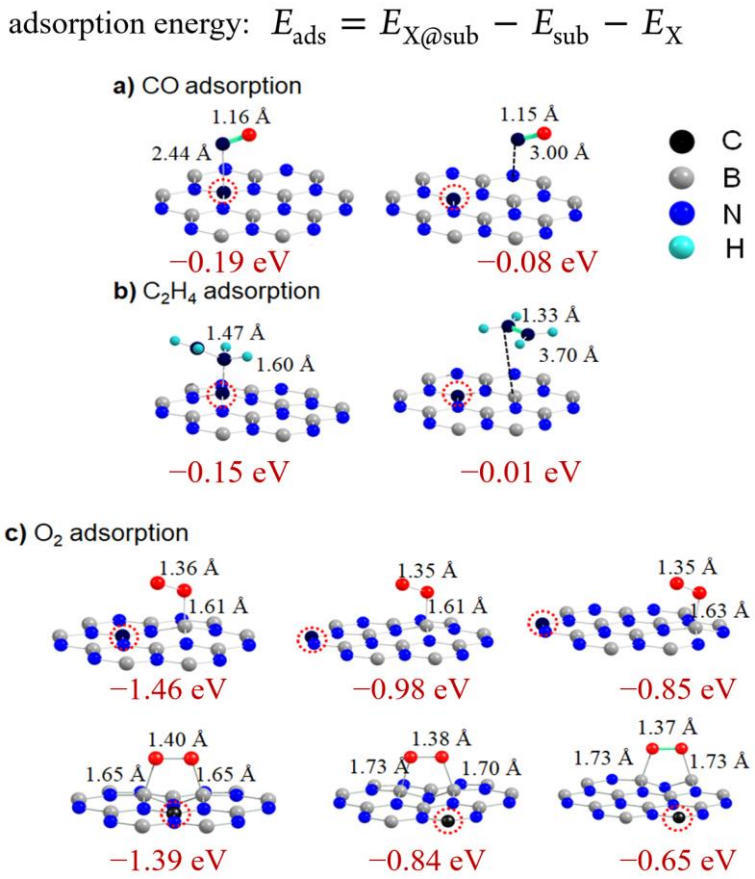

Figure 5.2. Optimized configurations of CO, C_2H_4 and O_2 molecules adsorbed on the C_B@h-BN monolayer. Their corresponding adsorption energies are given below each configuration indicated by the red color. For simplicity consideration, only a part of the C_B@h-BN monolayer has been shown. The distances between molecule and surface are given in Å. The red dashed circle represents the position of the doped C atom.

adsorption energy of −0.08 eV (−1.8 kcal/mol). The C−C bond length between CO molecule and C_B@h-BN is 2.44 Å, and the C−O bond length changes very limited from that of the free CO molecule, indicating that there is almost no electron transfer between the CO molecule and surface monolayer. Similarly, the C_2H_4 adsorption analysis has also shown that C_2H_4 molecule can weakly adsorb at the doped C site of the C_B@h-BN surface with the adsorption energy of −0.15 eV, there is no obvious interaction was found with other sites. In comparison to CO and C_2H_4 adsorption, the upcoming O_2 molecule can adsorb not only at the C atom site, but also at the B sites even far from the doped C atom. A detailed study on the O_2 adsorption on C_B@h-BN has been carried out in a previous work [18]: the O_2 molecule can adsorb on the top of B atom (top site) and the bridge two closet B atoms (bridge site) on the surface monolayer. As for the adsorption energy, O_2 molecule on the top site of B_S, B_M, and B_L sites are −1.46, −0.98 and −0.85 eV, respectively. A slightly weaker adsorption at the bridge sites than the top ones has also been found. In particular, the result reveals that the adsorption of O_2 molecule on C_B@h-BN monolayer strongly depends on the distance between the adsorption B sites and the doped C. Specifically, as the distance increases, the absolute values of adsorption energy gradually decreases. These adsorption energies are much larger than those of the former CO and C_2H_4 molecules.

After the O_2 adsorption, two main pathways can be proposed for the oxidation reaction [14]: i) the preliminary dissociation of the adsorbed O_2 molecule, followed with the oxidation of the reactant with the dissociated oxygen atoms; ii) the reactant directly interacts with the activated O_2 molecule. In this work, both these pathways will be considered for the oxidation reactions.

5.3.2 CO oxidation reaction mechanism on C_B@h-BN surface

Next, we pay attention to the possible catalytic reaction pathways for CO and C_2H_4 oxidation reactions occurring at the C_B@h-BN surface. Tremendous studies has been devoted to

investigating the CO oxidation reaction from different aspects [35−43]. The detailed mechanism of CO oxidation can be specifically classified into two different types: Langmuir−Hinshelwood (LH) mechanism, in which CO and O_2 molecules co-adsorb on the surface and then react with each other to induce the reaction, and Eley−Rideal (ER) mechanism, in which the isolated CO molecule reacts with the already adsorbed O_2 molecule to generate the product. In a previous study, we have found that either the self-promotion mechanism following the bimolecular LH mechanism or the ER mechanism can promote the CO oxidation on h-BN surface with the support of gold cluster. Herein, as the adsorption of O_2 molecule on C_B@h-BN surface is much stronger than the CO adsorption, we therefore mainly focus on the reaction mechanism of CO oxidation induced by the activated O_2 molecule on C_B@h-BN surface. After the adsorption and activation O_2 molecule, there are two possible pathways for the catalytic oxidation on C_B@h-BN should be considered: i) CO molecule interacts with the atomic O, which is produced by the dissociation of the adsorbed O_2 molecule; ii) CO molecule attacks the already activated adsorbed O_2 through breaking the O−O bond.

The barrier of O_2 dissociation on C_B@h-BN surface is about 1.83 eV. Such a high barrier indicates that it is difficult to break the O−O bond. Therefore, the CO oxidation is considered following the second pathway in which the CO molecule directly reacts with the O_2 activated on the C_B@h-BN surface. As the formation of the second product (CO with the O adatom) is much easier than formation of the first CO_2 product, herein, only the rate-determining step – first formation of CO_2 molecule will be shown in the following investigation. **Figure 5.3** shows the

energy profiles of CO oxidation reaction at the closest B_S site on the C_B@h-BN surface. The *y* coordinate shows the energy of each transition state and intermediate along the reaction pathway. According to our computational results, the reaction proceeds with the formation of a peroxide-

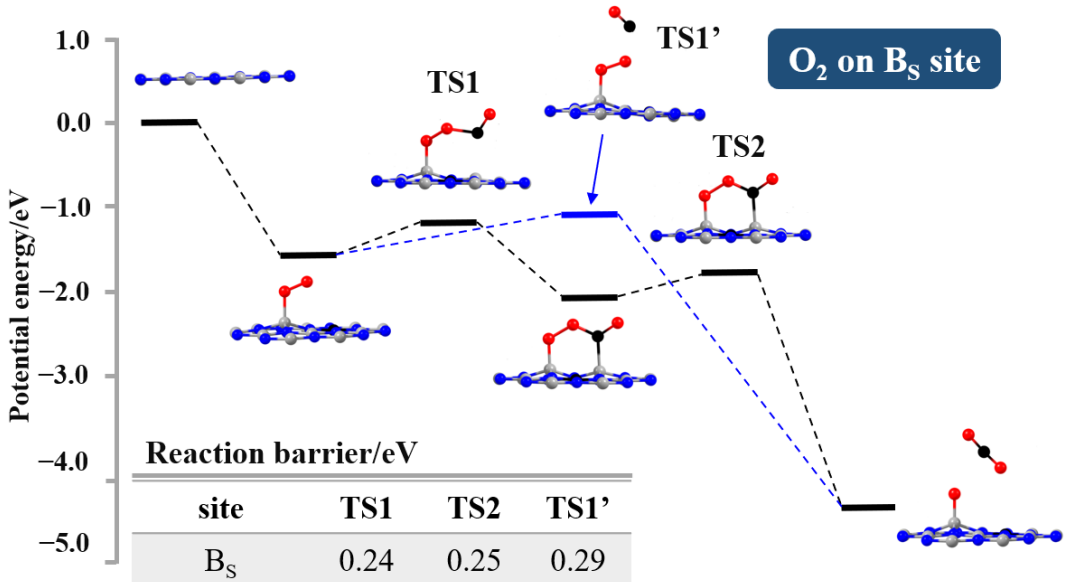

Reaction barrier/eV

site	TS1	TS2	TS1'
B_S	0.24	0.25	0.29
B_M	0.12	0.32	0.30
B_L	0.19	0.25	0.30

Figure 5.3. Energy profiles of CO oxidation at B_S site on C_B@h-BN surface. Only part of the h-BN monolayer is shown when taking the simplicity into consideration. The C, B, N, and O atoms are indicated by black, gray, blue, and red, respectively. Inset: a table showing the reaction barrier of formation of several transition states during the reaction for different B active sites.

like OCOO intermediate in the pathway. Formation of this intermediate is an exothermic step. The ci-NEB calculation shows this intermediate can be generated through the formation of TS1 with a considerable low activation barrier, 0.24 eV (5.5 kcal/mol). The low activation barrier can be considered as a result of the strong interaction between CO and O_2 molecules [44]. Co-adsorption of CO and O_2 molecule elongates the O−O bond of O_2 molecule to 1.49 Å. Furthermore, the OCOO intermediate is decomposed into a CO_2 molecule through the formation of TS2 in the Figure 5.3

with a low activation barrier of 0.25 eV (5.7 kcal/mol), resulting in the residual O atom strongly adsorbed on the surface with the adsorption energy of −4.24 eV (−97.8 kcal/mol). Such energy profile through the formation of OCOO intermediate via co-adsorption is generally called as the *self-promoting pathway*. Along this pathway, the co-adsorption of CO facilitates the breaking of O−O bond. On the other hand, our calculation has also revealed that the adsorbed O_2 molecule can also react with the CO molecule to generate the first CO_2 product through TS1' with a relatively low reaction energy, 0.29 eV (6.7 kcal/mol), resulting in the residual O atom adsorbed on the C_B@h-BN surface similar to the *self-promoting pathway*. This reaction pathway is indicated as the *direct pathway*: the CO molecule directly interacts with the absorbed O_2 molecule. Both *self-promoting pathway* and *direct pathway* predicted the relatively low activation energies, suggesting that the first CO_2 molecule is generated via these two reaction pathways on the C_B@h-BN surface.

Therefore, the overall reaction pathway of CO oxidation on C_B@h-BN surface follows (asterisk (*) denotes the adsorbed surface):

(1) $O_2 + * \rightarrow O_2*$,

(2) $CO + O_2* \rightarrow OCOO*$ or $CO + O_2* \rightarrow CO_2 + O*$ (rate-determining step),

(3) $OCOO* \rightarrow CO_2 + O*$,

(4) $CO + O* \rightarrow OCO*$ or $CO + O* \rightarrow CO_2 + *$,

(5) $OCO* \rightarrow CO_2 + *$.

As for the distance dependence, we carried out the ci-NEB calculation to search the reaction pathway for the other two B active sites: B_M, and B_L. Reaction barriers for formation of TS1, TS2 and TS1' are less affected when the distance changes, as shown in the inset table of **Figure 5.3**. In

the case of the *self-promoting pathway*, the reaction energies of the formation of the first CO_2 vary from 0.25, 0.32 and 0.25 eV for the B_S, B_M and B_L sites, respectively. The low reaction barrier even in the B active site with long distance shows that three adsorption sites: B_S, B_M and B_L are active. The distance from the doped C hardly affects the reactivity of these active sites. Such independence relationship can be also revealed from the calculation of direct pathways.

To investigate the origin of this long activation, we calculated the electron density difference for the co-adsorption of CO_2 molecule and O adatom on C_B@h-BN surface for different adsorption sites, as shown in **Figure 5.4**. The electron density difference calculation is based on $\rho = \rho(\text{TS1}) - \rho(\text{OCOO}) - \rho(C_B@\text{h-BN})$. According to the calculation, we found that the electron loss from the C_B@h-BN surface is mainly from the N and doped C close to the B active sites. The electron transfer from the 2p state of the doped C atom is less affected by the distance between the doped C and B active sites.

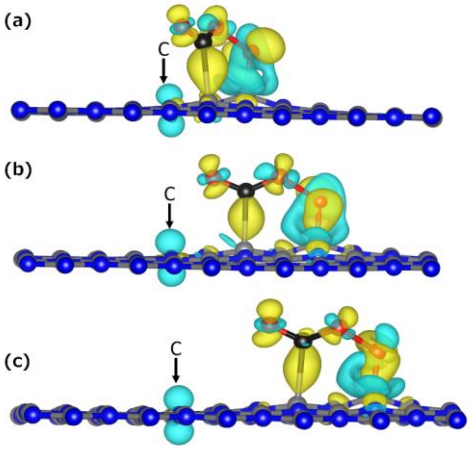

Figure 5.4. The electron density difference, $\rho = \rho(\text{TS1}) - \rho(\text{OCOO}) - \rho(\text{C}_\text{B}@\text{h-BN})$, for the co-adsorption of CO_2 molecule and O atom on the C_B@h-BN surface for different active sites. The yellow and green color indicates the electron accumulation and depletion, respectively. The isosurface is chosen at +0.005 and −0.005 e/Å^3.

5.3.3 C_2H_4 epoxidation reaction mechanism on C_B@h-BN surface

Similar to the CO oxidation reaction, we have also investigated the C_2H_4 epoxidation reaction mechanism. The optimized configurations and the corresponding adsorption energies of C_2H_4 and O_2 molecules adsorbed at the B_S site of C_B@h-BN has been shown in Figure 5.2. We found that the C_2H_4 molecule binds much weaker than the O_2 molecule, and no co-adsorption of C_2H_4 and O_2 molecules on C_B@h-BN surface has been found. Therefore, the O_2 adsorption on the surface is the first step of C_2H_4 epoxidation.

Figure 5.5 shows the reaction energy profile for the C_2H_4 oxidation along with the geometries of transition states and intermediates. Similar to the CO oxidation, herein, only the rate-determining step – first formation of C_2H_4 epoxide product will be shown in the following investigation. After the O_2 adsorption, the upcoming C_2H_4 molecule reacts the adsorbed O_2 molecule to form the OOC_2H_4 intermediate at the top site. The barrier of generating the OOC_2H_4 intermediate via TS1 is 0.39 eV (9.0 kcal/mol). Similar to the interaction between CO and O_2 molecules, the interaction between C_2H_4 molecule and the adsorbed O_2 molecule also elongates the O−O bond to promote the O_2 dissociation. After the formation of OOC_2H_4 intermediate, the

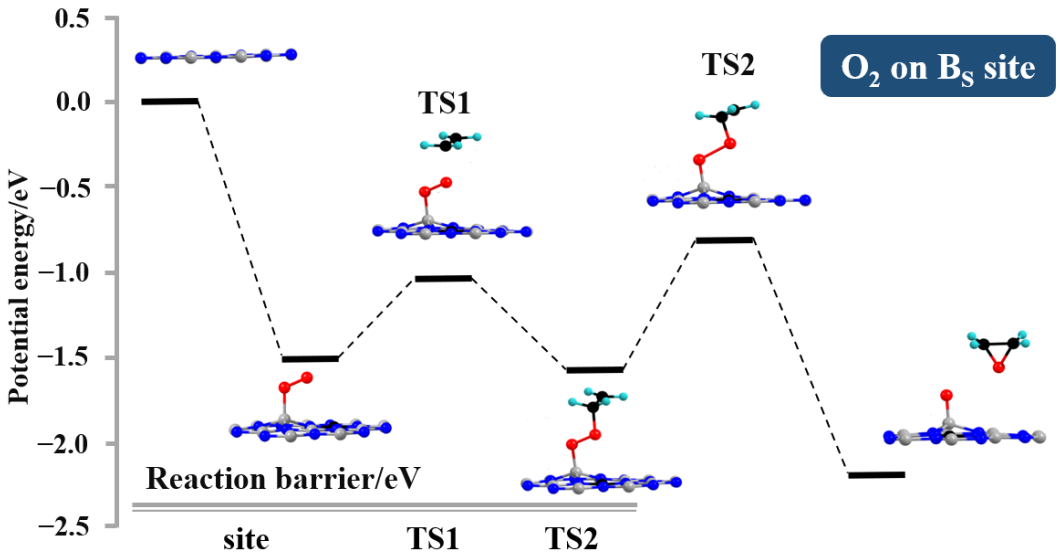

Reaction barrier/eV

site	TS1	TS2
B_S	0.39	0.71
B_M	0.46	0.64
B_L	0.45	0.62

Figure 5.5. Energy profiles for oxidation of ethylene to ethylene oxide at B_S sites. Energies are in the unit of eV. The corresponding geometries are shown in (c) and (d), only part of the h-BN surface is shown. Only part of the h-BN monolayer is shown when taking the simplicity into consideration. The C, B, N, and O atoms are indicated by black, gray, blue, and red, respectively. Inset: a table showing the reaction barrier of formation of several transition states during the reaction for different B active sites.

reaction proceeds with the formation of the first product and the residual O atom on the surface via the TS2. The reaction barrier of this step is 0.71 eV (16 kcal/mol).

In summary, the C_2H_4 epoxidation reaction on C_B@h-BN surface can proceed in the following steps:

(1) $O_2 + * \rightarrow O_2*$,

(2) $C_2H_4 + O_2* \rightarrow OOC_2H_4*$,

(3) $OOC_2H_4^* \rightarrow C_2H_4O + O^*$ (rate-determining step),

As for the distance dependence, the ci-NEB calculation has also been carried out to search the reaction pathway for the other two B active sites: B_M, and B_L. Reaction barriers for formation of TS1 and TS2 are less affected when the distance changes, as shown in the inset table of **Figure 5.5**. The low reaction barrier for the B active site with long distance indicates that three adsorption sites: B_S, B_M and B_L are all active for the reaction. The distances from the doped C atom possess limited effect on the reactivity of these active sites.

Similar to the CO oxidation, we then calculated the electron density difference for C2H4 epoxidation on the C_B@h-BN surface. **Figure 5.6** shows the variation in the electron density of the adsorbed species in TS1 induced by the interaction between OOC_2H_4 intermediate and C_B@h-BN surface. According to this density difference, we found that the electron loss from the C_B@h-BN surface is mainly from the N and doped C close to the B active sites. The electron transfer from the 2p state of the doped C atom is less affected by the distance between the doped C and B active sites. This effect is similar to the observed effect for CO oxidation reaction. Therefore, it can be suggested that the C_B@h-BN surface can be a potential catalyst for C_2H_4 epoxidation reaction due to the formation of the large active area around the C impurity of the C_B@h-BN surface.

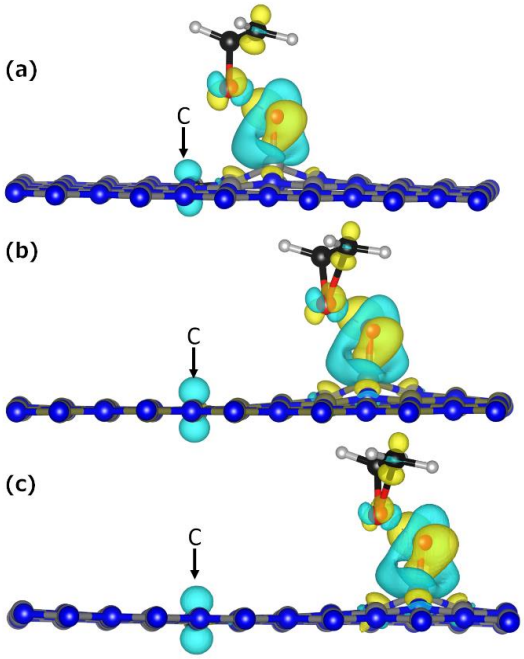

Figure 5.6. Distance dependence of electron density difference, $\rho = \rho(\mathrm{TS1}) - \rho(\mathrm{OOC_2H_4}) - \rho(\mathrm{C_B@h\text{-}BN})$, for the adsorption of $\mathrm{OOC_2H_4}$ intermediate on $\mathrm{C_B@h\text{-}BN}$ surface in the TS1 configuration for three adsorption sites. The yellow and green color indicates the electron accumulation and depletion, respectively. The isosurface is chosen at +0.005 and −0.005 e/Å^3.

5.4 Summary of This chapter

In this study, we have investigated the CO oxidation and C_2H_4 epoxidation induced by molecular oxygen on the carbon-doped hexagonal boron nitride (C_B@h-BN) surface. We have explicitly explored the energy profiles and also the dependence of the activation barriers on the distance between the doped C atom and the active sites. We have found the CO reaction can proceed with the self-promoting pathway induced by co-adsorption of CO and O_2 molecules on surface and the direct pathway. In contrary, the As a result, calculation of C_2H_4 epoxidation reaction shows the C_2H_4 molecule does not adsorb on the surface, the direct attacking between C_2H_4 and O_2 molecules is predicted. Moreover, we have also found the reaction barriers change very little with the increase in the distance from the doped C atom for the rare-determining steps of these two reactions. Therefore, we summarize that the C doping of h-BN monolayer can activate a wide area around the doped C atom. We therefore demonstrate that the C-doped h-BN monolayer can be used for development of potential catalyst for the oxidation reactions induced by the activation of molecular oxygen.

5.5 References

[1] Q. Fu and X. Bao, *Chem. Soc. Rev.* **46**, 1842 (2017).

[2] C. L. Tan, X. H. Cao, X. J. Wu, Q. Y. He, J. Yang, X. Zhang, J. Z. Chen, W. Zhao, S. K. Han, G. H. Nam, M. Sindoro, and H. Zhang, *Chem. Rev.* 117, 6225 (2017).

[3] S. F. Cai, H. P. Rong, X. F. Yu, X. W. Liu, D. S. Wang, W. He, and Y. D. Li, *ACS Catal.* **3**, 478 (2013).

[4] M. M. Montemore, M. A. van Spronsen, R. J. Madix, and C. M. Friend, *Chem. Rev.* **118**, 2816 (2018).

[5] X. G. Duan, K. O'Donnell, H. Q. Sun, Y. X. Wang, and S. B. Wang, *Small* **11**, 3036 (2015).

[6] M. Y. Liu, Z. R. Zhang, H. Z. Liu, Z. B. Xie, Q. Q. Mei, and B. X. Han, *Sci. Adv.* **4**, eaas9319 (2018).

[7] S. Navalon, A. Dhakshinamoorthy, M. Alvaro, M. Antonietti, and H. Garcia, *Chem. Soc. Rev.* **46**, 4501 (2017).

[8] N. Kan-Nari, S. Okamura, S. Fujita, J. Ozaki, and M. Araib, *Adv. Synth. Catal.* **352**, 1476 (2010).

[9] Y. H. Cao, H. Yu, F. Peng, and H. J. Wang, *ACS Catal.* **4**, 1617 (2014).

[10] R. J. Gao, L. Pan, J. H. Lu, J. S. Xu, X. W. Zhang, L. Wang, and J. J. Zou, *Chemcatchem* **9**, 4287 (2017).

[11] A. Dhakshinamoorthy, A. Primo, P. Concepcion, M. Alvaro, H. Garcia, *Chemistry* **19**, 7547 (2013).

[12] A. Lyalin, M. Gao, and T. Taketsugu, *Chem. Record.* **16**, 2324 (2016).

[13] M. Gao, A. Lyalin, and T. Taketsugu, *J. Phys. Chem. C* 116, 9054 (2012).

[14] M. Gao, A. Lyalin, and T. Taketsugu, *J. Chem. Phys.* **138**, 034701 (2013).

[15] A. Lyalin, A. Nakayama, K. Uosaki, and T. Taketsugu, *J. Phys. Chem. C* **117**, 21359 (2013).

[16] A. Lyalin, A. Nakayama, K. Uosaki, and T. Taketsugu, *Top. Catal.* **57**, 1032 (2014).

[17] K. Uosaki, G. Elumalai, H. Noguchi, T. Masuda, A. Lyalin, A. Nakayama, and T. Taketsugu, *J. Am. Chem. Soc.* **136**, 6542 (2014).

[18] M. Gao, M. Adachi, A. Lyalin, and T. Taketsugu. *J. Phys. Chem. C* **120**, 15993 (2016).

[19] K. Uosaki, G. Elumalai, H. C. Dinh, A. Lyalin, T. Taketsugu, and H. Noguchi, *Sci. Rep.* **6** (2016).

[20] A. Lyalin, K. Uosaki, and T. Taketsugu, *Electrocatalysis* **9**, 182 (2018).

[21] A. Gao, M. Nakahara, A. Lyalin, and T. Taketsugu, *J. Phys. Chem. C* **125**, 1334 (2021).

[22] J. T. Grant, C. A. Carrero, F. Goeltl, J. Venegas, P. Mueller, S. P. Burt, S. E. Specht, W. P. McDermott, A. Chieregato, and I. Hermans, *Science* **354**, 1570 (2016).

[23] R. Han, J. Y. Diao, S. Kumar, A. Lyalin, T. Taketsugu, G. Casillas, C. Richardson, F. Liu, C. W. Yoon, H. Y. Liu, X. D. Sun, and Z. G. Huang, *J. Energy. Chem.* **57**, 477 (2021).

[24] A. Lyalin, K. Uosaki, T. Taketsugu, *Electrocatalysis* **9**, 182 (2017).

[25] M. Shao, Q. Chang, J. P. Dodelet, and R. Chenitz, *Chem. Rev.* **116**, 3594 (2016).

[26] N. M. Markovic, T. J. Schmidt, V. Stamenkovic, and P. N. Ross, *Fuel Cells* **1**, 105 (2001).

[27] M. Gao, M. Adachi, A. Lyalin, and T. Taketsugu, *J. Phys. Chem. C* **120**, 15993 (2016).

[28] Z. G. Wu and R. E. Cohen, *Phy.Rev. B* **73** (2006).

[29] P. Giannozzi, S. Baroni, N. Bonini, M. Calandra, R. Car, C. Cavazzoni, D. Ceresoli, G. L. Chiarotti, M. Cococcioni, I. Dabo, A. D. Corso, S. de Gironcoli, S. Fabris, G. Fratesi, R. Gebauer, U. Gerstmann, C. Gougoussis, A. Kokalj, M. Lazzeri, L. Martin-Samos, N. Marzari, F. Mauri, R. Mazzarello, S. Paolini, A. Pasquarello, L. Paulatto, C. Sbraccia, S. Scandolo, G. Sclauzero, A.

Seitsonen, A. Smogunov, P. Umari, and R. Wentzcovitch, *J. Phys.: Condens. Matter* **21**, 395502 (2009).

[30] P. Giannozzi, O. Andreussi, T. Brumme, O. Bunau, M. B. Nardelli, M. Calandra, R. Car, C. Cavazzoni, D. Ceresoli, M. Cococcioni, N. Colonna, I. Carnimeo, A. D. Corso, S. de Gironcoli, P. Delugas, R. A. DiStasio, Jr., A. Ferretti, A. Floris, G. Fratesi, G. Fugallo, R. Gebauer, U. Gerstmann, F. Giustino, T. Gorni, J. Jia, M. Kawamura, H.-Y. Ko, A. Kokalj, E. Kkbenli, M. Lazzeri, M. Marsili, N. Marzari, F. Mauri, N. L. Nguyen, H.-V. Nguyen, A. O. de-la Roza, L. Paulatto, S. Ponc, D. Rocca, R. Sabatini, B. Santra, M. Schlipf, A. P. Seitsonen, A. Smogunov, I. Timrov, T. Thonhauser, P. Umari, N. Vast, X. Wu, and S. Baroni, *J. Phys.: Condens. Matter* **29**, 465901 (2017).

[31] C. S. Yoo, J. Akella, H. Cynn, and M. Nicol, *Phy. Rev. B* **56**, 140 (1997).

[32] G. Henkelman, B. P. Uberuaga, and H. Jonsson, *J. Chem. Phys.* **113**, 9901 (2000).

[33] G. Henkelman, A. Arnaldsson, and H. Jónsson, *Comput. Mater. Sci.* **36**, 354 (2006).

[34] K. Momma and F. Izumi, *J. Appl. Crystallogr.* **44**, 1272 (2011).

[35] M. Haruta, T. Kobayashi, H. Sano, and N. Yamada, *Chem. Lett.* **405** (1987).

[36] M. Haruta, *Catal. Today* **36**, 153 (1997).

[37] U. Landman, B. Yoon, C. Zhang, U. Heiz, and M. Arenz, *Top Catal.* **44**, 145 (2007).

[38] B. Yoon, H. Hakkinen, U. Landman, A. S. Worz, J. M. Antonietti, S. Abbet, K. Judai, and U. Heiz, *Science* **307**, 403 (2005).

[39] A. Sanchez, S. Abbet, U. Heiz, W. D. Schneider, H. Häkkinen, R. N. Barnett, and U. Landman, *J. Phys. Chem. A* **103**, 9573 (1999).

[40] M. Haruta and M. Date, *Appl. Catal. a-Gen.* **222**, 427 (2001).

[41] H. H. Kung, M. C. Kung, and C. K. Costello, *J. Catal.* **216**, 425 (2003).

[42] L. D. Socaciu, J. Hagen, T. M. Bernhardt, L. Woste, U. Heiz, H. Hakkinen, U. Landman, *J. Am. Chem. Soc.* **125**, 10437 (2003).

[43] J. M. C. Soares and M. Bowker, *Appl. Catal. a-Gen.* **291**, 136 (2005).

[44] Z. Lu, P. Lv, J. Xue, H. Wang, Y. Wang, Y. Huang, C. He, D. Ma, and Z. Yang, *RSC Adv.* **5**, 84381 (2015).

Chapter 6

Photo-oxidation Reaction at Phenol/Anatase TiO_2(001) Interface

In this chapter, we report the computational methods for providing the mechanistic insights into the photo-oxidation of phenol adsorbate on the surface of anatase TiO_2(001). The text in this section is essentially intended to outline how to model the excited state and exploit the fundamental process underlying the photocatalytic reactions at the periodic systems.

This chapter is organized as follows. In the beginning, we present the background of photo-oxidation reaction on surface system based on a previously reported study on phenol adsorbed on anatase TiO_2 surface. In Sec. 6.2, we introduce the computational models and parameters in this chapter. In Sec. 6.3.1, we derive the electronic structure calculation of phenol molecule adsorbed on anatase TiO_2 surface. The explicit results of reaction pathway calculation and the preferred reaction route is then given in Sec. 6.3.2. Finally, we draw the concluding remarks in Sec. 6.4.

6.1 Introduction and Motivation

Heterogeneous photocatalytic oxidation of organic compounds on semiconductor surface is an essential subject for studying the photocatalysis process [1−3]. After the absorption of photons, electrons and holes are separately formed that are able to initiate the chemical reactions. Understanding the charge separation of electron and holes, as well as the photocatalytic oxidation process after the formation of excited state is quite important due to the dependence between photochemical properties and kinetics of excited-state processes.

Titania (TiO_2) semiconductors (two main types: rutile and anatase) have been intensively studied due to its high chemical stability and efficient photocatalytic activity [3−7]. In comparison to the rutile, the metastable anatase is always considered more photoactive [8]. Investigations of some typical well-defined photocatalytic reactions and their detailed reaction mechanism play an important role development of various Titania oxide based photocatalytic materials. Among these reactions, photodissociation of phenol on TiO_2 surface is a prototypical case using this semiconductor material [9, 10]. Previously, the initial process of the photocatalytic phenol oxidation on anatase TiO_2(001) surface has been theoretically investigated using the long-range corrected (LC) time-dependent density functional theory (TDDFT) [11] by S. Suzuki *et. al*. [12]. The calculated excitation spectra of phenol-adsorbed TiO_2 surface has a strong peak at 3.3 eV which overlaps with that of the clean surface. Combining with the calculated atom-centered transition density matrix, the results indicate that the reaction undergoes a direct charge transfer from the phenol adsorbate to the TiO_2 surface which leads to the formation of radical cations of the phenol adsorbate.

Although the suggested reaction mechanism upon the production of radical cation of phenol has also been proposed in the end of the article, lack of theoretical proof is still a serious problem for completing the exact reaction after photoexcitation. Exploiting the reaction mechanism based on the excited state is still a challenge in the field of surface dynamics.

Numerous strategies or approximations have been utilized to treat the excited state dynamics simulation. Examples include: 1). anionic pseudopotential method [13, 14]. This method can model the ionic state of the adsorbate on the surface. Specifically, one electron is excited from the 1s core part and placed in the LUMO of adsorbate. For example, anionic state with F^{-1} pseudopotential can be represented by $1s^1 2s^2 2p^6$ configuration [15]. However, for production of

radical cation of phenol in this chapter, it is unreasonably to move electrons from valence orbital to the core orbital to construct the cationic state; 2). constrained DFT (cDFT) method. This diabatic states based method is designed to manually construct charge- and/or spin-constrained states and therefore the charge transfer rate can be determined, using the self-consistent ground state techniques [16−20]. The many-body wavefunctions that describe the localized charges can be obtained within DFT by modifying the Kohn-Sham equations to include a spatially-dependent potential, whose strength is varied self-consistently to satisfy the constraint of the desired number of electrons localized on a given atom or fragment [16−20]. However, it is until recent this method has been applied to periodic system [21] and is still very tricky to surface system with many atoms. Identifying the photoinduced reaction mechanism in an effective way, however, remains difficult for the periodic systems. This presents substantial challenges to understanding the variables that give rise to the chemistry occurring at the active site.

In this study, we aim to provide the theoretical insights into the exact reaction after photoexcitation at the most fundamental level from the dynamics point of view, trying to give an overall photo-oxidation mechanism until the formation of final products. Furthermore, effect of with or without anatase TiO_2 substrate on phenol oxidation mechanism will also be clarified.

6.2 Computational Details

All calculation until now in this chapter were performed using VASP software [22−25]. The electron exchange and correlation terms are treated with the PBE functional [26, 27]. Instead of the nanoparticle used in previous paper, we used the 3 × 3 surface with a relatively large surface area (11.48 × 11.48 × 40 Å). The calculations were spin polarized and were based on DFT+U approach [28]. The on-site U = 4.2 eV and J = 0 eV are applied to treat the 3d electrons of Ti atoms.

In this chapter, we investigated the photocatalytic oxidation reaction mechanism of phenol adsorbate on TiO_2(001) surface by an automated reaction pathway searching approach. This approach, namely artificial force induced reaction (AFIR) method [29−31] which is part of the global reaction route mapping (GRRM) strategy [29, 32], enables researchers to automatically locate a variety of possible reaction pathways and transition states. The obtained AFIR paths will be used for the further "RePATH" calculation. The "RePATH" calculation automatically applies all the other procedures, that is, LUP path optimization, EQ optimization, TS optimization, and IRC calculation, to all paths (either AFIR path, LUP path, or IRC path) that are read from previous results [32].

6.3 Results and Discussion

6.3.1. geometric and electronic structures of phenol−TiO_2 system

At first, we start from the introduction of optimized geometry. **Figure 6.1** shows the top and side views of the optimized geometry of phenol adsorbate on TiO_2(001) surface. The phenol adsorbate interacts with the surface through the O atom from −OH group and one Ti atom of the surface. Bond length between O atom and the adsorbing Ti atom is 2.190 Å. The tilt angle between the surface plane and aromatic ring is approximately 30°. The structure with a tilt angle is consistent with the structure predicted by using Ti_6O_{12} cluster model [12].

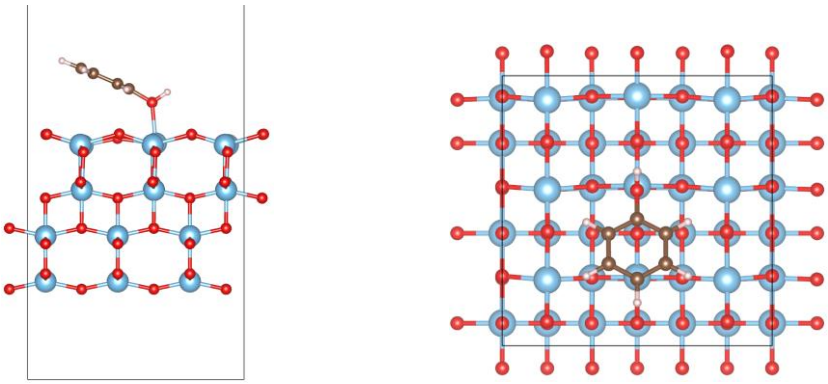

Figure 6.1. Top and side views of the optimized geometry of phenol adsorbate on TiO_2(001) surface in the ground state. The blue, red, brown, and pink color represent the Ti, O, C, and H atoms, respectively.

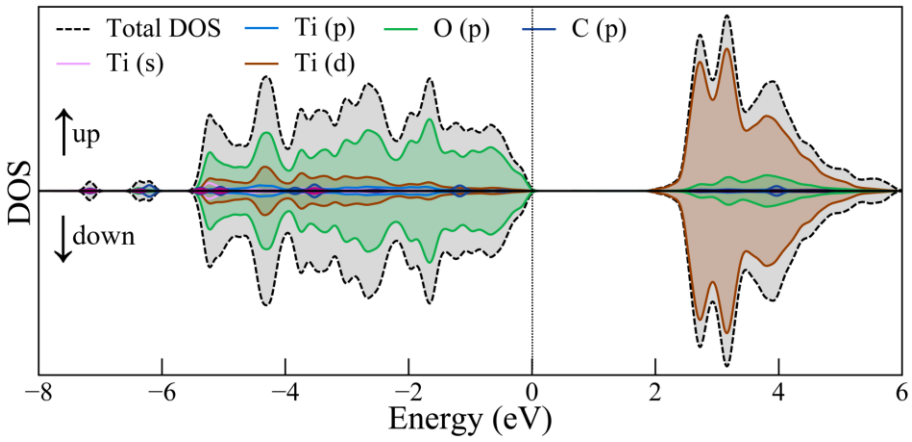

Figure 6.2. Total density of states and projected density of states (PDOS) of the phenol adsorbed on anatase TiO_2(001) surface. 0 eV corresponds to the Fermi level that indicated by the dot straight line.

To show the specific component of the electronic levels, we carried out the density of states calculation. **Figure 6.2** shows the projected DOS (PDOS) of the combined system. The PDOS

analysis here is to identify the main atomic orbital source for the adsorption. It can be found that the gap states of conduction band are mainly originated from the Ti 3d atomic orbitals, while the valence bands (VB) are primarily composed of the 2p orbital of O atoms, including O atoms from surface and the O atom of phenol adsorbate. For most pure DFT functionals such like PBE exchange correlation functional, the band gaps is usually underestimated due to the self-interaction error [26], even this error can be partially corrected at the PBE + *U* level (*U* = 4.2 added for Ti atoms in this chapter). We have confirmed that the experimental bandgap (~3.2 eV) is still much larger even the DFT + *U* has been performed.

6.3.2. reaction pathway analysis

For searching the reaction pathways of adsorbate with O_2 molecule, we utilized the multicomponent AFIR (MC−AFIR) methods [33]. At the initial time, AFIR paths are sampled starting from various initial structures. The set of initial structures are generated automatically by giving mutual orientations and positions of two or more inputted molecules randomly [32]. The terminate criterion NFault was set at 50 for reaction searches, which means the calculation will finish up when already-obtained structures are found 50 times.

To start with, we focus on the reaction between neutral phenol adsorbate and the oxygen molecule without the attendance of TiO_2(001) surface substrate. **Figure 6.3** shows the computed EQs that connected by the associated TS structures. It can be seen that the O_2 molecules has no interaction with the neutral phenol molecule, they are surrounding the phenol molecule and there is no actual interaction happens.

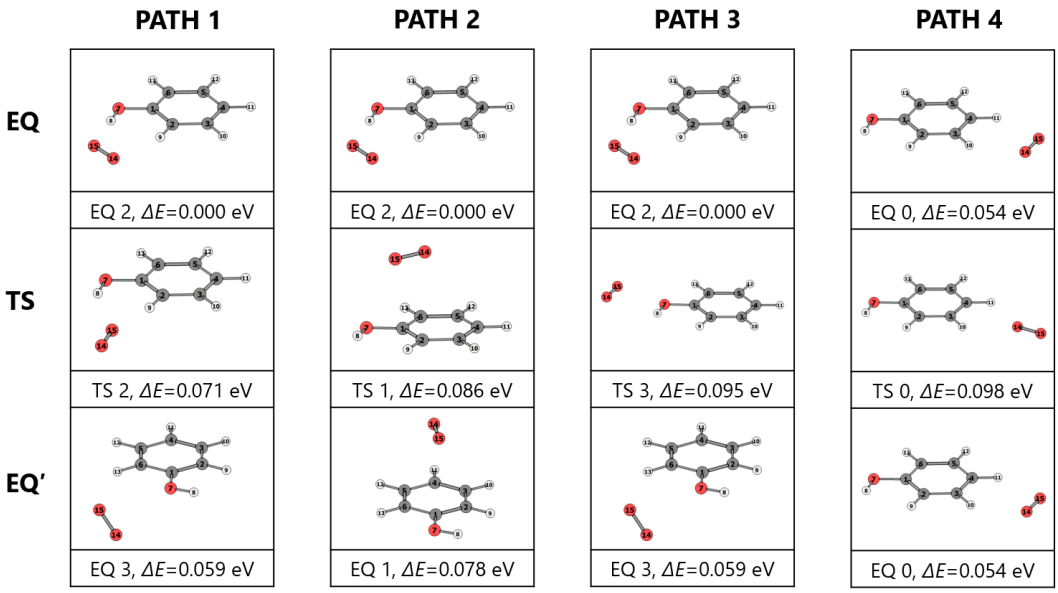

Figure 6.3. Calculated EQs and the TS structure connecting two respective EQs.

Then, we turn our attention to the cationic state of phenol adsorbate. Herein, the cationic state of phenol was constructed by introducing one positively charge and start with a computation of one positive charged and doublet structure. **Figure 6.4** shows the comparison between the calculated reaction pathway for reaction of phenol and O_2 molecule when phenol molecules are in their neutral and cationic states, respectively. Here, the force parameter γ which determines the biggest barrier of the predicted TSs is 200 kJ/mol (2.073 eV). This means that only the TSs with a barrier less than 2.073 eV can be obtained. We have found that there is no reaction between neutral phenol and O_2 molecule, while the cationic phenol reacts with the atoms in the aromatic ring, resulting in the formation of several equilibrium structure (EQ) (as shown in the Fig. 6.4). Specifically, there are 13 reactive intrinsic reaction coordinates (IRCs) have been predicted in total. Here, the obtained structure is therefore expected to proceed with the consecutive reaction until the formation of products for the photocatalytic oxidation reaction of phenol adsorbed on TiO_2 surface after the direct photoexcitation.

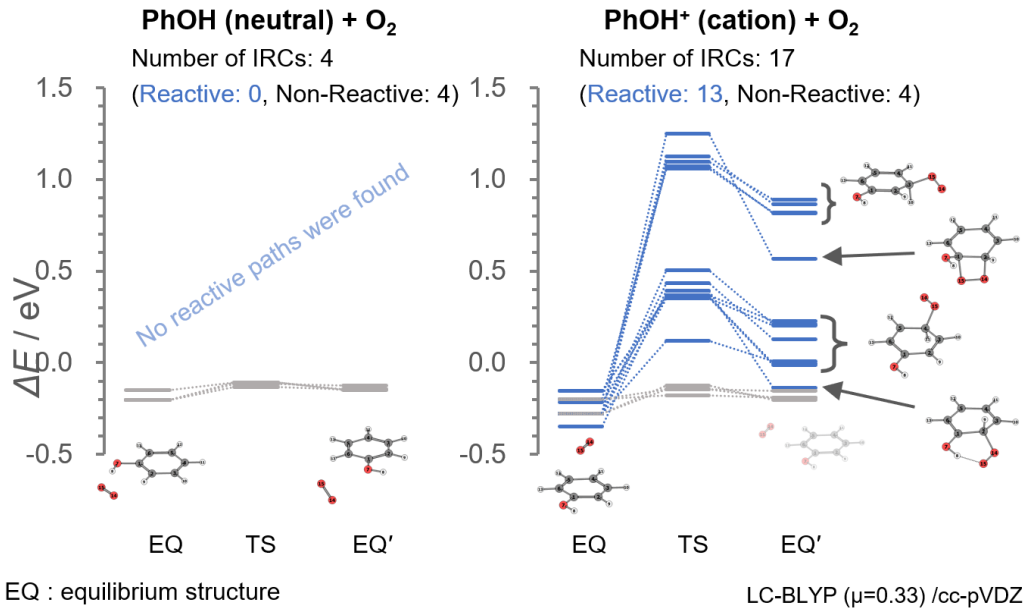

Figure 6.4. Comparison between the calculated reaction pathway for reaction of phenol and O_2 molecule when phenol molecules are in their neutral and cationic states, respectively.

Next, using the cationic phenol and O_2 as the reactant, we performed the reaction path searching. The calculated reaction path at present has been shown in **Figure 6.5**. The EQ4 is an important intermediate during the reaction we should pay attention to. The reactant can proceed with either 1-step route (purple color) or 3-step route (pink) to generate this intermediate. The pathway shown in red color in Fig. 6.4 represents an exothermic process after the formation of EQ4. Through this largely exothermic process, the overall reaction reaches the intermediate EQ6. The EQ6 has the lowest energy, and it is therefore expected to react with another upcoming O_2 molecule.

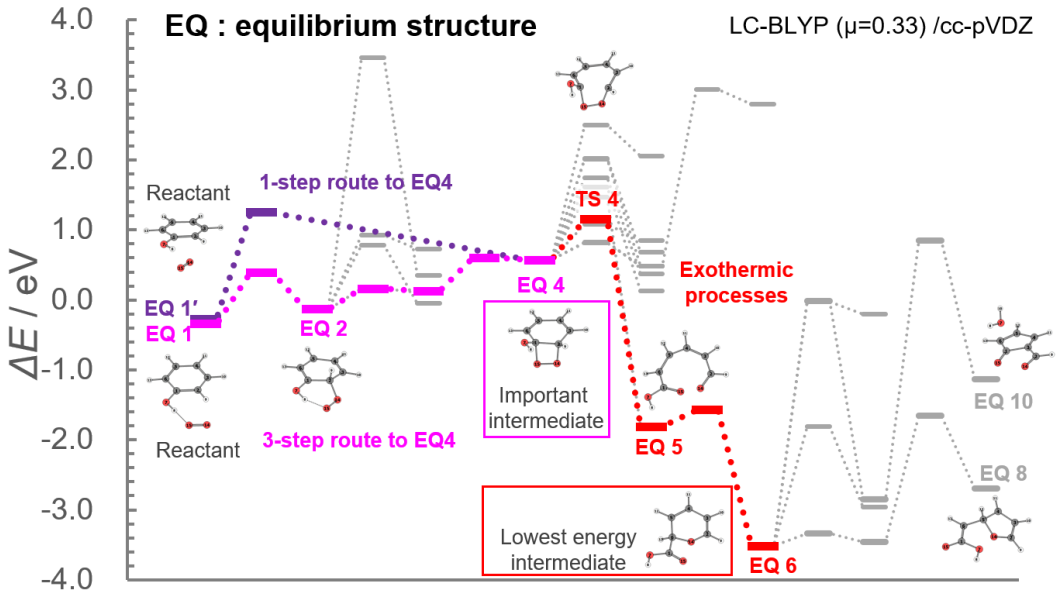

Figure 6.5. Comparison between the calculated reaction pathway for reaction of phenol and O_2 molecule when phenol molecules are in their neutral and cationic states, respectively.

6.4 Summary of This Chapter

We conclude our current findings obtained from the study in this chapter. To examine the excited states dynamics that can apply to the periodic surface system, we selected the photoexcitation of phenol adsorbate on anatase TiO_2(001) surface as model case study. We have attempted to present the AFIR calculation based on the cationic phenol adsorbate and O_2 molecule and compared the result with the reaction using neutral phenol molecule case. A difference in reaction pathway has been found between cationic and neutral states. No direct interaction has been expected using the neutral phenol molecule to react with O_2 molecule. Calculation using cationic phenol molecule leads to the formation of several equilibrium structures. The consecutive reaction until the formation of products is expected to continue based on this local minimum, thus providing the mechanistic insight into the future study when the TiO_2 surface has been taken into account and the photocatalytic oxidation reaction of phenol adsorbed on TiO_2 surface after the direct photoexcitation.

6.5 References

[1] Photocatalysis: Fundamentals and Perspectives; Schneider, J., Bahnemann, D. Ye, J. Puma, G. L. Dionysiou, D. D. Eds.; Royal Society of Chemistry: Cambridge, 2016.

[2] J. H. Kou, C. H. Lu, J. Wang, Y. K. Chen, Z. Z. Xu, and R. S. Varma, *Chem. Rev.* **117**, 1445 (2017).

[3]. Y. Nosaka and A. Y. Nosaka, *Chem. Rev.* **117**, 11302 (2017).

[4] U. Diebold, *Surf. Sci. Rep*. **48**, 53 (2003).

[5] X. Chen, S. S. Mao, *Chem. Rev*. **107**, 2891 (2007).

[6] J.-L Shi, H. M. Hao, and X. J. Lang, *Sustainable Energy Fuels*, **3**, 488 (2019).

[7] T.-Y. Wei and C.-C. Wan, *J. Photochem. Photobiol. A: Chem.* **69**, 241 (1992)

[8] A. Fujishima, X. Zhang, D. Tryk, *Surf. Sci. Rep*. **63**, 515 (2008).

[9] H. Chen, C. E. Nanayakkara, V. H. Grassian, *Chem. Rev*. **2012**, 112, 5919 (2012).

[10] H. G. Yang, C. H. Sun, S. Z. Qiao, J. Zou, G. Liu, S. C. Smith, H. M. Cheng, and G. Q. Lu, *Nature* **453**, 638 (2008).

[11] Y. Tawada, T. Tsuneda, S. Yanagisawa, T. Yanai, and K. Hirao, *J. Chem. Phys.* **120**, 8425 (2004).

[12] S. Suzuki, T. Tsuneda, and K. Hirao, *J. Chem. Phys*. **136**, 024706 (2012)

[13] L. Köhler and G. Kresse, *Phys. Rev. B* **70**, 165405 (2004).

[14] W. Ji, Z.-Y. Lu, and H. Gao, *Phys. Rev. Lett.* **97**, 246101 (2006).

[15] private e-mail with Dr. Kelvin Anggara, one of the authors of anionic pseudopotentials

[16] Q. Wu and T. Van Voorhis, *Phys. Rev. A* **72**, 024502 (2005).

[17] Q. Wu and T. Van Voorhis, *J. Chem. Theory Comput.* **2**, 765 (2006).

[18] Q. Wu and T. Van Voorhis, *J. Phys. Chem. A* **110**, 9212 (2006).

[19] B. Kaduk, T. Tsuchimochi, and T. V. Voorhis, *J. Chem. Phys*. **140**, 18A503 (2014).

[20] B. Kaduk, T. Kowalczyk, T. V. Voorhis, *Chem. Rev*. **112**, 321 (2012)

[21] M. B. Goldey, N. P. Brawand, M. Vörös, and G. Galli, J. *Chem. Theory Comput.* **13**, 6, 2581 (2017).

[22] G. Kresse and J. Hafner, *Phys. Rev. B* **47**, 558 (1993).

[23] G. Kresse and J. Hafner, *Phys. Rev. B* **49**, 14251 (1994).

[24] G. Kresse and J. Furthmüller, *Phys. Rev. B* **54**, 11169 (1996).

[25] G. Kresse and J. Furthmüller, *Comput. Mater. Sci.* **6**, 15 (1996).

[26] J. P. Perdew, K. Burke and M. Ernzerhof, *Phys. Rev. Lett.* **77**, 3865 (1996).

[27] J. P. Perdew, K. Burke and M. Ernzerhof, *Phys. Rev. Lett.* **78**, 1396 (1997).

[28] S. L. Dudarev, G. A. Botton, S. Y. Savrasov, C. J. Humphreys, and A. P. Sutton, *Phys. Rev. B* **57**, 1505 (1998).

[29] S. Maeda, K. Ohno, and K. Morokuma, *Phys. Chem. Chem. Phys.* **15**, 3683 (2013).

[30] S. Maeda, T. Taketsugu, and K. Morokuma, *J. Comput. Chem.* **35**, 166 (2014).

[31] S. Maeda, Y. Harabuchi, M. Takagi, T. Taketsugu, and K. Morokuma, *Chem. Rec.* **16**, 2232 (2016).

[32] S. Maeda, Y. Harabuchi, M. Takagi, K. Saita, K. Suzuki, T. Ichino, Y. Sumiya, K. Sugiyama, and Y. Ono, *J. Comput. Chem*. **39**, 233 (2018).

[33] S. Maeda and K. Morokuma, *J. Chem. Theory Comput*. **7**, 2335 (2011)

Chapter 7

General Conclusion

Knowledge and understanding acquired in this thesis studies is expected to impact various practical problems in a wide range of interfacial properties. There is one theme throughout the overall chapters, ***surface***. The introduction, theoretical methods, and discussion using some model case studies have therefore been expanded in detail based on this theme.

In Chapter 3, we investigated the substituent effect on the electron transfer at the interface between self-assembled monolayer and metal substrate. The shift in frequency is closely related to the variation of electron donating or withdrawing ability of the substituents. A bond order model derived from the periodic implementation of natural bond orbital algorithm was used as a measure of bond strength. This proposed DFT-based indicator can be easily extended to other adsorbate−surface studies.

In Chapter 4, we illustrated the metal substrate effect on chemical bonding strength at the interface using the joint theoretical method and the experimental spectroscopic observations. The larger blue-shift in vibrational frequency when the Au surface was used as the metal substrate is attributed to the more significant σ donation over the Ag case. Moreover, we have emphasized the synergistic relationship between experimental and theoretical studies in the field of molecular electronic devices.

In Chapter 5, catalytic reaction occurring at carbon-doped h-BN surface has been examined. We verified the catalytic activity in the wide range from the C dopant through the calculation of activation barriers and reaction pathways of two typical reactions, CO oxidation and C_2H_4

epoxidation. The findings may open up a novel avenue to tune the catalytic activity of electron transport at metal-molecule interfaces.

Finally, in Chapter 6, we aimed to provide some mechanistic insights into the photocatalytic chemical reaction on surface. We employed the artificial force induced reaction method implemented in the global reaction route mapping strategy. Neutral and cationic states of phenol molecules exhibited distinct behavior when interacts with the O_2 molecule. The study is expected to be applied to anatase TiO_2 surface.

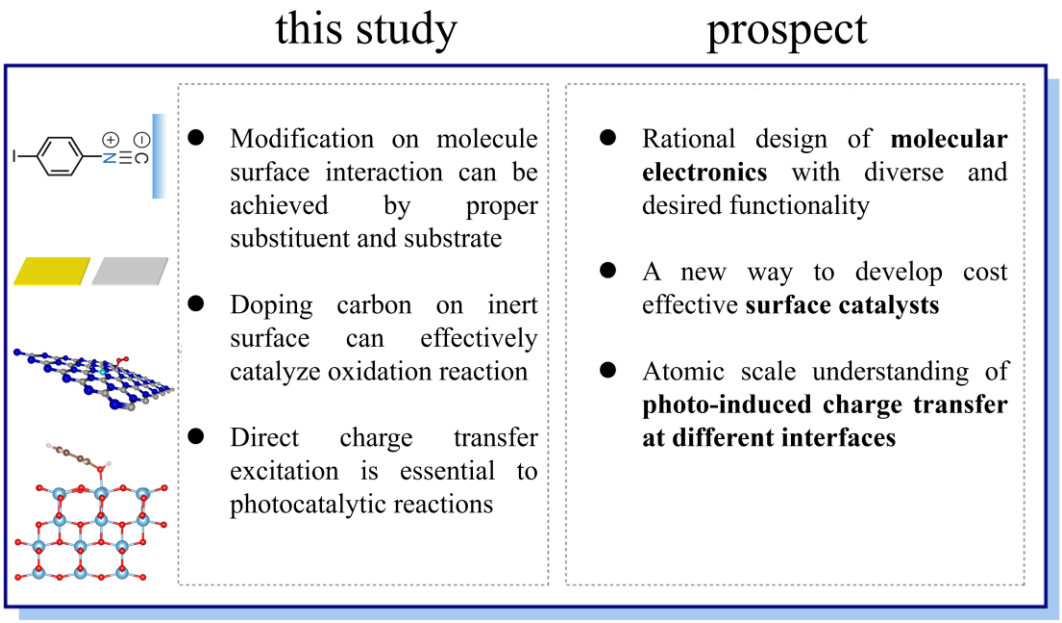

The above figure summarizes the findings and future prospects of this dissertation. This dissertation covers the theoretical methods for developing the DFT-based indicators for evaluating the bonding strengths and describing the electron transfer across the interfacial region. By revealing the important role of substituent and substrate on electron transfer, our report will strengthen the fundamental design efforts to atomistic control of molecule−surface interactions and development of efficient molecular electronic devices. We therefore hope it would be of benefit to both theorists and experimentalists working in this fascinating area.

Despite the progress in this thesis, I have to admit many intricacies of the surface systems have been ignored. Our knowledge of chemical phenomena and reaction dynamics on surface is still quite primitive, especially for the excited state dynamics on surface systems. Also, modification on the bond order model and inclusion of other lower lying molecular orbitals are required to adapt for the SAMs and metal surface with increasing structural complexity (surface coverage, surface reconstruction, molecular orientation, defects, and etc.).

This thesis is the first step toward incorporating more elements of chemical phenomena at interface into the corresponding calculations. We hope these elements can be included by means of quantum chemistry in the future.

Abbreviations

SAM	self-assembled monolayer
MPI	4-methylphenyl isocyanide
PDI	1,4-phenylene diisocyanide
MO	molecular orbital
HOMO, LUMO	highest occupied and lowest unoccupied molecular orbital
eV	electronvolt
Å	angstrom
2PPE	two-photon photoelectron
NEXAFS	near-edge X-ray absorption fine structure
DFT	density functional theory
DFPT	density functional perturbation theory
KS	Kohn-Sham
(P)DOS	(Projected) density of states
VASP	Vienna Ab initio Simulation Package
VESTA	Visualization for Electronic and Structural Analysis
CG	conjugate-gradient
QE	quantum espresso
PWscf	plane-wave self-consistent field
ASE	atomic simulation environment
EDG	electron-donating groups
EWG	electron-withdrawing groups
SFG	sum frequency generation

NBO	natural bonding orbital
QTAIM	Bader’s quantum theory of atoms-in-molecule
ELF	electron localization function
PBC	periodic boundary condition
BZ	Brillouin zone
PBE	Perdew−Burke−Ernzerhof
GGA	generalized gradient approximation
MO	molecular orbital
PAW	projected-augmented wave
NEB	nudged-elastic band
AFIR	artificial force induced reaction
MC-AFIR	multicomponent AFIR
GRRM	global reaction route mapping
EQ	equilibrium structure
TS	transition state
IRC	intrinsic reaction coordinate
RePath	path refinement
LUP	locally updated planes

ACKNOWLEDGMENT

First and foremost, I would like to thank my Ph.D. advisor, Prof. Tetsuya Taketsugu for giving me the opportunity to study in his research group. I'm so fortunate to be a member of quantum chemistry laboratory (QCL). This thesis work would not have been completed without the patient help, credible instruction, deep scientific knowledge of my advisor, and also the scientific atmosphere of QCL to work in.

Special thanks to Dr. Min Gao from Institute for Catalysis (ICT), Hokkaido University, who led me to my first research project and shared me her creative advice about the computation at the beginning time. I would also like to thank my dissertation committee: Prof. Junya Hasegawa, Prof. Toshihiro Shimada, and Associate Prof. Masato Kobayashi.

I would also like to thank my collaborator: Prof. Kohei Uosaki from NIMS. The graceful and comprehensive experimental work by Prof. Kohei Uosaki and his colleges, Prof. Katsuyoshi Ikeda, Prof. Hidenori Noguchi, and Dr. Mikio Ito inspired me and motivated this theoretical work. I appreciate the cooperation with them.

I am also so grateful to Prof. Takao Tsuneda and Assist. Prof. Kenichiro Saita. I cannot promote my research without the regular discussion online. I also want to thank all group members of QCL I have met in this three-year's study.

The financial support from China Scholarship Council (CSC) is gratefully acknowledged. I cannot pour myself into the study and research without the help of this scholarship.

Finally, I would like to thank my girlfriend, Yicheng Li. Her encouragement, support, and patience have made the past three years at Sapporo full of pleasure, and such a few sentences could ever convey my gratitude. I also appreciate my family for their love and emotional encouragement.